From General Relativity, to Axionic-Dark-Matter-Induced Inflationary Cosmology, and 'Holographic' Graphene

by

Michael P. Pierpoint

Thesis to be inserted

Submitted in partial fulfilment of the requirements

for the award of

Doctor of Philosophy of Loughborough University

February 19, 2015

Declaration of Originality

I hereby declare that all work presented in this thesis is original, and that all literature has been cited where necessary. Publications within the appendices, duly note the contributions from co-authors.

Abstract

This thesis explores the expansive world of *General Relativity*, and its role to play in modern cosmology and quantum field theory. We begin with a pedagogical approach to relativity, in particular, highlighting upon the ambiguity that arises with the conventions used in different textbooks. A brief introduction to tensor calculus has also been provided in the appendix. The preliminary chapters are also complimented with examples of numerical relativity via simulation. We then move on to discuss examples of non-linear systems, and their exact solutions. Such systems will be analogous to those we shall encounter later, upon considering scalar field theories as a means of modelling dark energy. We shall introduce the 'axion' as our highly motivated dark matter candidate, since this will ultimately determine the behaviour of the scalar field. Coupled to a scaling factor across the spatial domain, it is found that this scalar field will ultimately determine the evolution of our universe. The key result of this thesis has been the possibility to screen both the cosmological constant, and flatness of the universe, to within observable parameters. These results will be explicitly derived from first principles. Also included is a tentative approach to *holographic theory*, in which strongly correlated systems may be modelled within the asymptotic domain of Anti-de Sitter (AdS) space. Ultimately, our aspirations are to bridge the gap with condensed matter theory, in particular with the publications included within

the latter appendices. These publications discuss graphene as a revolutionary new material, for inclusion in both transistor-based and optoelectronic devices

Keywords: Relativity, Cosmology, Axions, AdS/CFT, Graphene, Optoelectronic.

From The Author

... "theoretical physicists - what do we have in common with a supermodel? We hardly spend our lives before mirrors using chemical foundation to beautify our looks, appearing in top magazines with the latest 'goss', with the shear want and desire to be idolised by the general public. No, our lives play out before whiteboards, the scene upon which we use mathematical foundation to beautify our minds! Our aim? to appear in highly acclaimed scientific journals with the latest ground-breaking new study, forever being 'immortalised' by our peers, spearheading the intrigue of individuals who will one day take our place. Maybe we're not so dissimilar after all!"

The Student Mindset of Today...

Results mean everything, to such a degree they can either empower or eradicate an individual's drive and enthusiasm. Although someone may possess a concise understanding and all the confidence at their disposal, just one bad examination mark can to mislead them to believe they were never actually that good. We often learn material without necessarily understanding how it will benefit us. Countless times have I encountered young students who say "what is the point of algebra? when am I ever gonna use that?"

Throughout my childhood, I was simply told that I needed it "to pass the exam". Nonetheless, despite essentially being force-fed this knowledge, we continually find ourselves open to more and more advanced material. The question is, when exactly does this chain of intellectual development cease? One possibility may be the limitations of our own minds, a view I personally do not support. I find it disturbing to believe that a mind can ever cease in its development - of course it can be hindered, but far more importantly, it can be nurtured.

The key principle to facilitate learning is to ask questions first, thereby supplying the immediate motivation for success. Why is the sky dark at night? How big is the universe? These are all questions one would ask as a child, but if the answers were put to us without the prompt of our own curiosity, we would not care less. The youth of today would be more concerned with the latest iTech gadgets and games consoles (certainly something Euclid circa 300 BC did not have to contend with). Fortunately, there are instances when a certain subject or individual can rekindle a sense of purpose and direction. Such instances leave you asking many intuitive questions, and allow your imagination to subsume an entire escapade of its own.

I have prepared this thesis as a continuation of my original MPhys dissertation, throughout which I lay the foundations for an introductory course in General Relativity (GR). For the benefit of the reader, I reiterate some of my original ideas, and elaborate upon them to a move advanced level. At the time, the Department of Physics had no such course in GR. I therefore extend my utmost gratitude to Dr. C. A. Hoenselaers for his supervision, his advice and direction, which allowed my final year as an undergraduate to be one of the most intellectual endeavours I had ever embarked upon. Nowadays, I can proudly say that Loughborough University offers fully fledged modules in

Relativity and Cosmology, a move which was pioneered by my co-supervisor, Dr. D. R. Gulevich. For the duration of my Ph.D, Dima has invested much faith in myself to supervise multiple taught and practical modules (including those 1am sessions at our observatory!). For this, and the confidence I have gained, I am eternally grateful.

Of course, I must also pay tribute my co-author and friend, Dr. Alan Wu, for our work in graphene-based electronics, and his contribution to our joint study of holographic superconductors. Alan is the most innocent person I know, and to quote his Ph.D examiner, Prof. Mikko Saarela, "incredibly stubborn". Thanks Alan!

Undoubtedly, my greatest thanks lie with my supervisor, Prof. F. V. Kusmartsev. Feo has the capability to listen to any crazy idea I may have, and somehow make it a workable reality (including time-travel to the past!). As a supervisor, he knows me better than I know myself! Since 2006, he has become like a father figure, understanding exactly what I am capable of, knowing my limits, and if my work is the best it could be. At times during my Ph.D, the word 'supervisor' has even become synonymous with 'counsellor' - whether this be my sister in hospital, or recently, the loss of my grandfather, Feo has always been there to guide me through such troubling times. Finally, I am (of course) grateful for the conferences Feo has allowed me to attend. Aside from the work aspect, they provided a welcome opportunity to meet new friends and have a personal life!

To any students who may read this thesis in the nearby future, I shall make the following point. The avid reader will no doubt have already skimmed through the main bulk of this text. After seeing just how 'abstract' the mathematics can be in places, some of you may now feel uneasy,

unsure whether you wish to continue reading on. This is typical of us as human beings; mankind has always feared that what it does not understand. It is no different from someone who has difficulty reading; claiming the words either appear blurred or jumbled. This more than often stems from a lack of experience, an unfamiliarity within the context being dealt with. This was certainly the way I felt upon first tackling my MPhys dissertation. The notation within literature seemed almost alienating, unlike anything seen before. A classic example of this is the Standard Model Lagrangian of Particle Physics (cf. Page viii). This more than often is met by a sense of bewilderment, but why should it be? Of course to say it is long winded would be a grotesque understatement. However, upon closer inspection, we find some fundamental constants, partial derivatives, gauge bosons, and particles/antiparticles; things we are very familiar with. It is only by studying the entity as a whole that we begin to lose touch. In the same manner, I discourage any student from attempting to understand an equation in this text (at first) as a whole. Instead, one should look for components which appear familiar, and to each of them assign a physical meaning. Just remember, it does not matter if you cannot understand an equation; after all, an equation is simply a means of describing a physical process in the language of mathematics.

$$-\tfrac{1}{2}\partial_\nu g^a_\mu \partial_\nu g^a_\mu - g_s f^{abc}\partial_\mu g^a_\nu g^b_\mu g^c_\nu - \tfrac{1}{4}g_s^2 f^{abc}f^{ade}g^b_\mu g^c_\nu g^d_\mu g^e_\nu + \tfrac{1}{2}ig_s^2(\bar{q}^\sigma_i\gamma^\mu q^\sigma_j)g^a_\mu + \bar{G}^a\partial^2 G^a +$$

$$g_s f^{abc}\partial_\mu \bar{G}^a G^b g^c_\mu - \partial_\nu W^+_\mu \partial_\nu W^-_\mu - M^2 W^+_\mu W^-_\mu - \tfrac{1}{2}\partial_\nu Z^0_\mu \partial_\nu Z^0_\mu - \tfrac{1}{2c^2_w}M^2 Z^0_\mu Z^0_\mu - \tfrac{1}{2}\partial_\mu A_\nu \partial_\mu A_\nu - \tfrac{1}{2}\partial_\mu H \partial_\mu H -$$

$$\tfrac{1}{2}m_h^2 H^2 - \partial_\mu \phi^+ \partial_\mu \phi^- - M^2\phi^+\phi^- - \tfrac{1}{2}\partial_\mu\phi^0\partial_\mu\phi^0 - \tfrac{1}{2c^2_w}M\phi^0\phi^0 - \beta_h[\tfrac{2M^2}{g^2} + \tfrac{2M}{g}H + \tfrac{1}{2}(H^2 + \phi^0\phi^0 +$$

$$2\phi^+\phi^-)] + \tfrac{2M^4}{g^2}\alpha_h - igc_w[\partial_\nu Z^0_\mu(W^+_\mu W^-_\nu - W^+_\nu W^-_\mu) - Z^0_\nu(W^+_\mu \partial_\nu W^-_\mu - W^-_\mu \partial_\nu W^+_\mu) + Z^0_\mu(W^+_\nu \partial_\nu W^-_\mu -$$

$$W^-_\nu \partial_\nu W^+_\mu)] - igs_w[\partial_\nu A_\mu(W^+_\mu W^-_\nu - W^+_\nu W^-_\mu) - A_\nu(W^+_\mu \partial_\nu W^-_\mu - W^-_\mu \partial_\nu W^+_\mu) + A_\mu(W^+_\nu \partial_\nu W^-_\mu -$$

$$W^-_\nu \partial_\nu W^+_\mu)] - \tfrac{1}{2}g^2 W^+_\mu W^-_\mu W^+_\nu W^-_\nu + \tfrac{1}{2}g^2 W^+_\mu W^-_\nu W^+_\mu W^-_\nu + g^2 c^2_w(Z^0_\mu W^+_\mu Z^0_\nu W^-_\nu - Z^0_\mu Z^0_\mu W^+_\nu W^-_\nu) +$$

$$g^2 s^2_w(A_\mu W^+_\mu A_\nu W^-_\nu - A_\mu A_\mu W^+_\nu W^-_\nu) + g^2 s_w c_w[A_\mu Z^0_\nu(W^+_\mu W^-_\nu - W^+_\nu W^-_\mu) - 2A_\mu Z^0_\mu W^+_\nu W^-_\nu] -$$

$$g\alpha[H^3 + H\phi^0\phi^0 + 2H\phi^+\phi^-] - \tfrac{1}{8}g^2\alpha_h[H^4 + (\phi^0)^4 + 4(\phi^+\phi^-)^2 + 4(\phi^0)^2\phi^+\phi^- + 4H^2\phi^+\phi^- +$$

$$2(\phi^0)^2H^2] - gMW^+_\mu W^-_\mu H - \tfrac{1}{2}g\tfrac{M}{c^2_w}Z^0_\mu Z^0_\mu H - \tfrac{1}{2}ig[W^+_\mu(\phi^0\partial_\mu\phi^- - \phi^-\partial_\mu\phi^0) - W^-_\mu(\phi^0\partial_\mu\phi^+ - \phi^+\partial_\mu\phi^0)] +$$

$$\tfrac{1}{2}g[W^+_\mu(H\partial_\mu\phi^- - \phi^-\partial_\mu H) - W^-_\mu(H\partial_\mu\phi^+ - \phi^+\partial_\mu H)] + \tfrac{1}{2}g\tfrac{1}{c_w}(Z^0_\mu(H\partial_\mu\phi^0 - \phi^0\partial_\mu H) - ig\tfrac{s^2_w}{c_w}MZ^0_\mu(W^+_\mu\phi^- -$$

$$W^-_\mu\phi^+) + igs_w MA_\mu(W^+_\mu\phi^- - W^-_\mu\phi^+) - ig\tfrac{1-2c^2_w}{2c_w}Z^0_\mu(\phi^+\partial_\mu\phi^- - \phi^-\partial_\mu\phi^+) + igs_w A_\mu(\phi^+\partial_\mu\phi^- - \phi^-\partial_\mu\phi^+) -$$

$$\tfrac{1}{4}g^2W^+_\mu W^-_\mu[H^2 + (\phi^0)^2 + 2\phi^+\phi^-] - \tfrac{1}{4}g^2\tfrac{1}{c^2_w}Z^0_\mu Z^0_\mu[H^2 + (\phi^0)^2 + 2(2s^2_w - 1)^2\phi^+\phi^-] - \tfrac{1}{2}g^2\tfrac{s^2_w}{c_w}Z^0_\mu\phi^0(W^+_\mu\phi^- +$$

$$W^-_\mu\phi^+) - \tfrac{1}{2}ig^2\tfrac{s^2_w}{c_w}Z^0_\mu H(W^+_\mu\phi^- - W^-_\mu\phi^+) + \tfrac{1}{2}g^2 s_w A_\mu\phi^0(W^+_\mu\phi^- + W^-_\mu\phi^+) + \tfrac{1}{2}ig^2 s_w A_\mu H(W^+_\mu\phi^- -$$

$$W^-_\mu\phi^+) - g^2\tfrac{s_w}{c_w}(2c^2_w - 1)Z^0_\mu A_\mu\phi^+\phi^- - g^1 s^2_w A_\mu A_\mu\phi^+\phi^- - \bar{e}^\lambda(\gamma\partial + m^\lambda_e)e^\lambda - \bar{\nu}^\lambda\gamma\partial\nu^\lambda - \bar{u}^\lambda_j(\gamma\partial +$$

$$m^\lambda_u)u^\lambda_j - \bar{d}^\lambda_j(\gamma\partial + m^\lambda_d)d^\lambda_j + igs_w A_\mu[-(\bar{e}^\lambda\gamma^\mu e^\lambda) + \tfrac{2}{3}(\bar{u}^\lambda_j\gamma^\mu u^\lambda_j) - \tfrac{1}{3}(\bar{d}^\lambda_j\gamma^\mu d^\lambda_j)] + \tfrac{ig}{4c_w}Z^0_\mu[(\bar{\nu}^\lambda\gamma^\mu(1+\gamma^5)\nu^\lambda) +$$

$$(\bar{e}^\lambda\gamma^\mu(4s^2_w - 1 - \gamma^5)e^\lambda) + (\bar{u}^\lambda_j\gamma^\mu(\tfrac{4}{3}s^2_w - 1 - \gamma^5)u^\lambda_j) + (\bar{d}^\lambda_j\gamma^\mu(1 - \tfrac{8}{3}s^2_w - \gamma^5)d^\lambda_j)] + \tfrac{ig}{2\sqrt{2}}W^+_\mu[(\bar{\nu}^\lambda\gamma^\mu(1+\gamma^5)e^\lambda) +$$

$$(\bar{u}^\lambda_j\gamma^\mu(1+\gamma^5)C_{\lambda\kappa}d^\kappa_j)] + \tfrac{ig}{2\sqrt{2}}W^-_\mu[(\bar{e}^\lambda\gamma^\mu(1+\gamma^5)\nu^\lambda) + (\bar{d}^\kappa_j C^\dagger_{\lambda\kappa}\gamma^\mu(1+\gamma^5)u^\lambda_j)] + \tfrac{ig}{2\sqrt{2}}\tfrac{m^\lambda_e}{M}[-\phi^+(\bar{\nu}^\lambda(1 -$$

$$\gamma^5)e^\lambda) + \phi^-(\bar{e}^\lambda(1+\gamma^5)\nu^\lambda)] - \tfrac{g}{2}\tfrac{m^\lambda_e}{M}[H(\bar{e}^\lambda e^\lambda) + i\phi^0(\bar{e}^\lambda\gamma^5 e^\lambda)] + \tfrac{ig}{2M\sqrt{2}}\phi^+[-m^\kappa_d(\bar{u}^\lambda_j C_{\lambda\kappa}(1-\gamma^5)d^\kappa_j) +$$

$$m^\lambda_u(\bar{u}^\lambda_j C_{\lambda\kappa}(1+\gamma^5)d^\kappa_j] + \tfrac{ig}{2M\sqrt{2}}\phi^-[m^\lambda_d(\bar{d}^\lambda_j C^\dagger_{\lambda\kappa}(1+\gamma^5)u^\kappa_j) - m^\kappa_u(\bar{d}^\lambda_j C^\dagger_{\lambda\kappa}(1-\gamma^5)u^\kappa_j] - \tfrac{g}{2}\tfrac{m^\lambda_u}{M}H(\bar{u}^\lambda_j u^\lambda_j) -$$

$$\tfrac{g}{2}\tfrac{m^\lambda_d}{M}H(\bar{d}^\lambda_j d^\lambda_j) + \tfrac{ig}{2}\tfrac{m^\lambda_u}{M}\phi^0(\bar{u}^\lambda_j\gamma^5 u^\lambda_j) - \tfrac{ig}{2}\tfrac{m^\lambda_d}{M}\phi^0(\bar{d}^\lambda_j\gamma^5 d^\lambda_j) + \bar{X}^+(\partial^2 - M^2)X^+ + \bar{X}^-(\partial^2 - M^2)X^- + \bar{X}^0(\partial^2 -$$

$$\tfrac{M^2}{c^2_w})X^0 + \bar{Y}\partial^2 Y + igc_w W^+_\mu(\partial_\mu\bar{X}^0X^- - \partial_\mu\bar{X}^+X^0) + igs_w W^+_\mu(\partial_\mu\bar{Y}X^- - \partial_\mu\bar{X}^+Y) + igc_w W^-_\mu(\partial_\mu\bar{X}^-X^0 -$$

$$\partial_\mu\bar{X}^0X^+) + igs_w W^-_\mu(\partial_\mu\bar{X}^-Y - \partial_\mu\bar{Y}X^+) + igc_w Z^0_\mu(\partial_\mu\bar{X}^+X^+ - \partial_\mu\bar{X}^-X^-) + igs_w A_\mu(\partial_\mu\bar{X}^+X^+ -$$

$$\partial_\mu\bar{X}^-X^-) - \tfrac{1}{2}gM[\bar{X}^+X^+H + \bar{X}^-X^-H + \tfrac{1}{c^2_w}\bar{X}^0X^0H] + \tfrac{1-2c^2_w}{2c_w}igM[\bar{X}^+X^0\phi^+ - \bar{X}^-X^0\phi^-] +$$

$$\tfrac{1}{2c_w}igM[\bar{X}^0X^-\phi^+ - \bar{X}^0X^+\phi^-] + igMs_w[\bar{X}^0X^-\phi^+ - \bar{X}^0X^+\phi^-] + \tfrac{1}{2}igM[\bar{X}^+X^+\phi^0 - \bar{X}^-X^-\phi^0]$$

The Standard Model Lagrangian of Particle Physics

... so why are we here?

Indeed this a question asked by mankind for generations! In our quest for the truth, we traverse our entire intellectual progress as human beings. As the first amino-acids multiplied in the primordial soup, did they possess our same curiosity, or were their minds simply too primitive? Are the bacteria of petri-dishes aware of themselves being studied, and that some almighty entity influences their existence? Mankind has kowtowed to this principle for millennia. The so called 'acts of god', the idea of 'fate' that everything in the universe is pre-determined (incidentally, a concept refuted by the EPR experiment). Certain individuals refuse to take these ideas at face value, and seek a more concise and practical means of explaining everyday observation. From the first works of geometry by Euclid, to Galileo, Newton and Einstein; they have all sought the truth as to why certain things behave in certain ways. But supposing such inspirational minds never existed, or like Galileo, were all convicted of heresy for their beliefs. Where exactly would this place our society today? As a consequence of their efforts, have emerged evermore intriguing, and somewhat radical theories of gravitation and quantum mechanics which are at the forefront of modern-day physics. A personal favorite is the Copenhagen interpretation of quantum mechanics, concerning probabilities and the acts of measurement. We recall how Schrodinger's cat was *hypothetically* in a superposition of being both dead and alive. By opening the box, the state-vector was collapsed, thus rendering the result of the experiment. But is the same necessarily true vice-versa on the grand cosmological scale? If we were placed in an indestructible box, such that no information could be extracted from outside (not even gravita-

tional influence), would the universe be in a superposition of both existent and non-existent? Yet more controversially, would the universe even exist if you yourself were not around to collapse the state-vector and observe it?

Messier 42 - The Great Orion Nebula as captured by myself at our departmental observatory (December 2010).

Contents

Part I

A Short Recap of General Relativity

Chapter 1

Why is General Relativity Needed?

1.1 Introduction

Published in 1915, Einstein's General Theory of Relativity was quite simply a theory of gravitation; an extension of his original work [1] to include non-inertial frames of reference. This was necessary, since the special theory broke down for an observer who either deviated from a straight path, changed speed, or approached a significantly large mass. Recall the famous twin paradox, in which one twin remains on Earth while the other makes the return trip to a nearby star and back. Why does one twin appear to age more than the other if the two viewpoints are physically equivalent? The answer is simple; the travelling twin must turn at some point which invokes an acceleration, and as such, would momentarily occupy a non-inertial frame of reference.

"the happiest thought of my life" - A. Einstein

Einstein's motivation initially arose in 1907. His argument was clear, namely that a universe abiding by Newtonian gravity would not coincide with the laws of Special Relativity. This was evident, since Newton's law of gravity makes no reference to time. Thus, a mass m_1 would *instantaneously* feel a change in gravitational force if mass m_2 were to be displaced (since gravitational force is inversely proportional to the square of separation). This physical effect, seemingly capable of being mediated at a speed greater than that of light, was of course inconsistent with the laws of Special Relativity. His answer to this dilemma was simple, eliminate gravity and Special Relativity will work! My belief is the following; Einstein found he could eliminate gravity if he were to simply prevent the iconic apple from hitting Sir Isaac's head in the first place. From Galileo, we recall that (neglecting air resistance) objects released simultaneously will fall at the same rate, irrespective of their mass or physical nature.

As an example, let us consider placing Newton and the apple tree in a stationary elevator, which upon release will hurtle towards the ground at a steady $9.81\,\mathrm{ms}^{-2}$. Supposing the act of release dislodges an apple from one of its branches, Newton will remain completely oblivious to the fact that an apple is now 'floating' directly above his head. It is only when Newton stands up, that he realises something is not quite right. He finds himself moving towards not only a floating apple, but the roof of the elevator. It was almost as if the magical force keeping him on the floor had completely disappeared! Einstein likened this to an astronaut in outer space, in a region free from gravitational influence (a necessary requirement for Special Relativity to work). Einstein considered this to be "the happiest thought of his life" - more specifically, that for an observer falling freely from the roof of

a house, no gravitational field would *locally* exist. Thus, in the immediate surroundings of an event, space-time appears locally flat! Conversely, one may look at this from a different perspective; the Earth has a curved surface, yet as we zoom in closer and closer, the geometry indeed appears locally flat.

1.1.1 The Principle of Equivalence

Einstein's insight would come to be known as the Principle of Equivalence, of which many versions exist. The Weak Equivalence Principle (WEP) merely states that an accelerated system is equivalent to a system which is subject to gravitational influence. Let us again consider the apple falling on Newton's head, this time whilst he rests on terra firma. The apple experiences a gravitational force F which accelerates it towards him at $9.81\,\mathrm{ms}^{-2}$,

$$F = \frac{GMm_g}{r^2} = m_g g \ . \tag{1.1}$$

Here M corresponds to the mass of the Earth, m_g is the *gravitational* mass of the apple, and g is the acceleration due to gravity. Observe that g is independent of m_g. This is nothing more than a derivative restatement of Galileo's work - objects fall at the same rate, irrespective of their mass. Now imagine Newton being seated in a vessel in outer space, free from gravitational influence, and coincidentally travelling upwards from his point of view with an acceleration $a = 9.81\,\mathrm{ms}^{-2}$ (i.e., mimicking gravity). Supposing he looks up, he would observe an apple being accelerated towards him, mediated by a force governed by his second law of motion. In fact, it is the apple which remains stationary... a classic example of relativity!

$$F = m_i a = m_i g \ , \tag{1.2}$$

where m_i is the *inertial* mass of the apple. Since the two scenarios are physically equivalent, from Eqs.(1.1,1.2), we may conclude that gravitational and inertial mass are equivalent (i.e., $m_g = m_i$). Hitherto, this is something which has been experimentally proven to an incredibly high accuracy (cf. for details Eötvös [2]). However, in the presence of colossal gravitational fields (e.g., a black hole), the condition of locality becomes evermore difficult to satisfy, and the weak equivalence principle begins to break down. This is a consequence of phenomena known as 'tidal forces', which we shall now discuss.

1.1.2 Tidal Forces

Let us begin with the following question - what shape is the Earth? Of course, one does not expect the reader to roll *'oblate spheroid'* straight off the tongue. This deformed sphere is caused not only by the fact that the Earth is rotating, but because there is a large mass orbiting us which dictates the advancing and receding tides of our oceans. Suppose now we take this argument further via a reversed example. If the moon has a measurable effect on the Earth, surely the Earth would impose a much more considerable effect upon anything in orbit. Suppose then we place a spherical, uniform distribution of particles above the Earth's atmosphere (cf. Figure 1.1). Assuming negligible air resistance, what would then follow is that the arrangement of particles becomes 'pear' shaped. This is because particles which are closer to the Earth's surface are subject to a more powerful gravitational influence, and thus accelerate more quickly. Additionally, the particles follow paths called geodesics (straight lines on a curved geometry), which are directed towards Earth's core. Particles at the same *initial* height will therefore become closer with time.

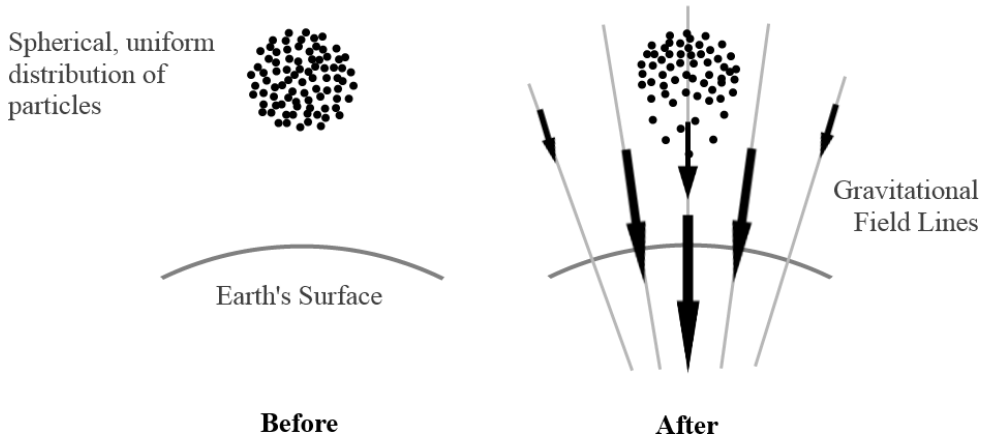

Figure 1.1: A spherical, uniform distribution of particles which are subject to a nearby gravitational field. The particles follow gravitational field lines that are directed towards the Earth's core, and thus converge with time. When considering a more localised distribution, the effect of tidal forces becomes almost negligible.

1.2 Non-Inertial Clocks

Those familiar with Special Relativity will no doubt have met the light clock; a clock which ticks every time a light ray strikes the emitter or receiver. The thought experiment shows how moving clocks 'run slower', since the light has a greater distance to travel. We shall now extend the premise to a situation involving non-inertial reference frames (cf. Figure 1.2). At point 1 in this figure, a light ray is emitted and reaches the receiver in the *inertial* reference frame at point 2. In the non-inertial reference frame, the receiver is moving in the direction of the light ray with an ever increasing speed. As a consequence, the light ray travels a greater distance, meeting the receiver a finite time later at point 3. Since the speed of light is an invariant quantity, the most logical argument is that time had slowed down in the non-inertial

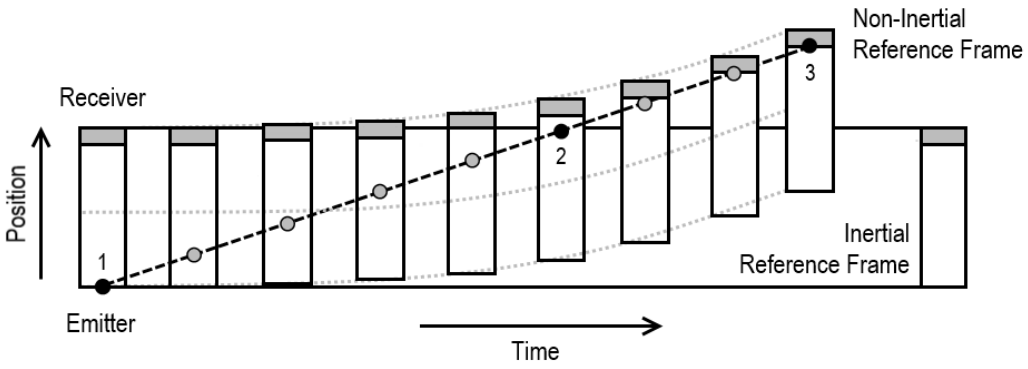

Figure 1.2: A light ray is emitted in both inertial, and non-inertial reference frames. Since the light ray has further to travel in the non-inertial reference frame, and the speed of light is an invariant quantity, one must conclude that the rate of passage of time has decreased.

reference frame - an effect commonly referred to as *time dilation*. Via the equivalence principle (cf. Section 1.1.1), this implies that the same can be assumed of a clock residing within Earth's gravitational field. Observational evidence has confirmed that clocks on Earth's surface do indeed tick slower than those in outer space, where acceleration due to gravity is weaker [3]. Although such discrepancies account for merely a few microseconds per day, this remains outside the tolerance of precision-oriented devices such as GPS systems.

Returning to the twin paradox (cf. Section 1.1), how may we distinguish between who *really* occupies the non-inertial reference frame? Suppose that a light ray travels perpendicular to the direction of motion (cf. Figure 1.3). For an observer occupying a 'stationary' inertial reference frame, the light ray will travel from left to right without deviation. However, the observer in the non-inertial reference frame views something completely different. Suppose the moving observer were to travel with uniform velocity. The light ray

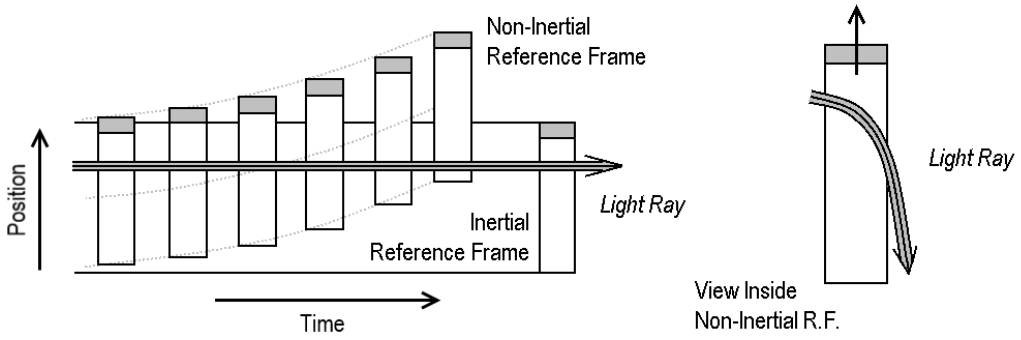

Figure 1.3: A light ray travelling perpendicular to the direction of motion as viewed in both the inertial, and non-inertial reference frames. Inside the non-inertial reference frame, the observer will see the light bend towards the bottom of the clock.

would appear slanted, but nonetheless, follow a straight trajectory. However, since the system is accelerating, the light ray appears to bend. Thus we conclude that light in non-inertial reference frames does not conform to straight lines. Once again, the principle of equivalence implies that light entering a gravitational field will bend as a direct result.

1.2.1 Gravitational Red-Shift

Finally, suppose that in Figure 1.3, our observer in the non-inertial frame is fixed at the receiving end. As a consequence of the Doppler effect, he would observe the light continuously red-shifting in wavelength at an increasing rate. The same can be said of an observer positioned at the receiver in Figure 1.2. The light is red-shifted because it takes longer to reach this point. Recall that time period is inversely proportional to frequency, and frequency is inversely proportional to wavelength. So, as time dilates (i.e., increases), wavelength increases. Via the equivalence principle, the same can

be applied to a yellow submarine entering a black hole. As it accelerates, the light we observe from its hull is red-shifting at an increasing rate, before finally turning infra-red. This observed effect is termed *Gravitational Red-Shift*.

Chapter 2

Introducing the Mathematics

The basic idea of General Relativity, is that the laws of physics should be *independent* of our choice of coordinate system (e.g., Cartesian or polar). To accomplish this, we require tensors (objects which transform in a certain way under coordinate transformations). A brief overview of tensor calculus has been included in Appendix A of this thesis.

2.1 Riemannian Geometry

From Special Relativity, recall that space-time is a four dimensional pseudo-Riemannian manifold (three dimensions of space, one dimension of time); otherwise known as Minkowski space-time or $\mathbb{R}^{3,1}$. The prefix 'Riemannian' simply means that a 'metric' is involved - a Rank-2 covariant tensor that tells us everything concerning the geometry of our manifold. The prefix 'pseudo' refers to a minus sign, thus distinguishing Lorentzian from Euclidean geometries. Normally, a metric would subscribe to three axioms - those of positivity, symmetry, and the triangle inequality. Here, positivity is the exception. Any metric must also satisfy the properties of invertability (i.e.,

non-vanishing determinant), and must be diagonalisable with eigenvalues (-,+,+,+).

Any point lying on this manifold is called an event, specified by four coordinates. Any vectors which then exist in space-time (i.e., four-vectors) are always fixed to a particular event. It is also known that the distance ds between two events is an invariant quantity (i.e., independent of our choice of coordinate system). For a four dimensional space-time, the invariant interval is given as follows,

$$\begin{aligned} ds^2 &= -c^2dt^2 + dx^2 + dy^2 + dz^2 \\ &= -(dx^0)^2 + (dx^1)^2 + (dx^2)^2 + (dx^3)^2 \\ ct = x^0 \qquad x = x^1 \qquad y = x^2 \qquad z = x^3 \end{aligned}$$

For the remainder of this text, we shall take the speed of light c to be normalised to one.

It is far more convenient to adopt tensors for writing these kind of formulae. The term x^μ (a set of four numbers, with index μ running from zero to three) specifies the location of an event in space-time. It is a widely accepted convention to use Greek indices for space-time coordinates. Latin indices are used only if spatial coordinates are being dealt with. Displacing the event then gives us a set of basis vectors dx^μ to work with. Similarly, one could label an event as x^ν (again with $\nu = 0 \ldots 3$), giving another set of basis vectors dx^ν. Half way there, we now require a means of summing these vectors and giving them the necessary coefficients. To do this, we utilise the Minkowski metric $\eta_{\mu\nu}$.

$$\eta_{\mu\nu} = \begin{pmatrix} -1 & 0 & 0 & 0 \\ 0 & +1 & 0 & 0 \\ 0 & 0 & +1 & 0 \\ 0 & 0 & 0 & +1 \end{pmatrix}$$

$$ds^2 = \eta_{\mu\nu} dx^\mu dx^\nu = \eta_{00} dx^0 dx^0 + \eta_{11} dx^1 dx^1 + \eta_{22} dx^2 dx^2 + \eta_{33} dx^3 dx^3$$

$$= -(dx^0)^2 + (dx^1)^2 + (dx^2)^2 + (dx^3)^2 \tag{2.1}$$

This equation employs the use of the Einstein Summation Convention (cf. Appendix A.3).

2.2 Telling the Time

In the previous chapter, we discovered that clocks which occupy non-inertial frames of reference, tick at a slower rate. How exactly does one calculate the difference? How does one calculate the time elapsed inside an accelerating spaceship (i.e., the *proper time* τ)? To answer this, we first require a space-time diagram (cf. Figure 2.1). The first thing to notice is how the vessel is constrained to travel at less than the speed of light (the worldline must always reside within a light cone). A worldline is represented as $x^\mu(\lambda)$, where each component is a function of an affine parameter λ. The change of interval 's' with respect to parameter λ, is the absolute magnitude (or two-norm) of the velocity (i.e., tangent) vector v^μ. This is an example of a *contravariant* vector (possessing a single upper index).

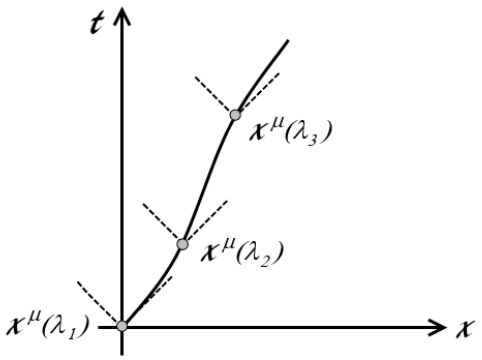

Figure 2.1: A space-time diagram, throughout which a spaceship's course is plotted. The worldline $x^\mu(\lambda)$ is parametrised by an affine parameter λ, and always constrained to be time-like (i.e., residing within the local light cone). Points along the worldline, for example $x^\mu(\lambda_2)$, are referred to as 'events'.

Suppose then we have the following worldline,

$$x^\mu(\lambda) = \left\{x^0(\lambda), x^1(\lambda), x^2(\lambda), x^3(\lambda)\right\} \ .$$

The tangent vector v^μ is given as the worldline $x^\mu(\lambda)$ differentiated with respect to the parameter λ,

$$v^\mu = \left\{\frac{dx^0}{d\lambda}, \frac{dx^1}{d\lambda}, \frac{dx^2}{d\lambda}, \frac{dx^3}{d\lambda}\right\} \ .$$

Its absolute magnitude (i.e., the two-norm) $|v^\mu|$ is then,

$$|v^\mu| = \left(\left(\frac{dx^0}{d\lambda}\right)^2 + \left(\frac{dx^1}{d\lambda}\right)^2 + \left(\frac{dx^2}{d\lambda}\right)^2 + \left(\frac{dx^3}{d\lambda}\right)^2\right)^{\frac{1}{2}} = \frac{ds}{d\lambda} \ . \qquad (2.2)$$

Eqs.(2.1,2.2) do not look too dissimilar - however, the coefficient of dx^0

in Eq.(2.1) is negative. This is because space-time is not Euclidean, but Lorentzian in nature. Let us now give Eq.(2.2) the minus sign it requires. To do this we divide Eq.(2.1) by $d\lambda^2$,

$$\frac{ds^2}{d\lambda^2} = \eta_{\mu\nu}\frac{dx^\mu}{d\lambda}\frac{dx^\nu}{d\lambda} = -\left(\frac{dx^0}{d\lambda}\right)^2 + \left(\frac{dx^1}{d\lambda}\right)^2 + \left(\frac{dx^2}{d\lambda}\right)^2 + \left(\frac{dx^3}{d\lambda}\right)^2 \ .$$

We also recall from Special Relativity, that if an observer is seated in the moving spaceship (i.e., the change in spatial components are zero), then the observer will record the proper time τ,

$$\frac{ds^2}{d\lambda^2} = \eta_{\mu\nu}\frac{dx^\mu}{d\lambda}\frac{dx^\nu}{d\lambda} = -\left(\frac{d\tau}{d\lambda}\right)^2 \ .$$

Re-arranging a little and integrating gives,

$$\tau = \int_{\lambda_1}^{\lambda_2} \sqrt{-\eta_{\mu\nu}\frac{dx^\mu}{d\lambda}\frac{dx^\nu}{d\lambda}}\ d\lambda \ ,$$

which is the proper time τ as recorded inside the moving spaceship. Under initial inspection, it may seem as though we are taking the root of a negative quantity. However, bare in mind that $ds^2 < 0$ for a time-like worldline; the minus sign makes the entity being square rooted, positive.

2.2.1 Numerical Relativity

So as to emphasise the effect of a non-inertial frame of reference, we shall now consider a few numerical examples. Figure 2.2 traces out several worldlines (i.e., trajectories), with our aim being to calculate the proper time for each observer. For simplicity, we shall first consider the Minkowski space-time,

and all intermediary calculations can be referred to in Appendix B.1. Relatively speaking, it is clear that observer 2 ages by the least amount. This is because in addition to the velocity x-component $v_x = \sqrt{0.4999}$, there is (at times) a velocity y-component of equal magnitude. When added together, these two components imply that observer 2 is travelling very close to the speed of light.

To fully realise the effects of time dilation, it is more convenient to express in terms of the *average* gamma factor γ. This can be determined by the ratio of the observed and proper times $\gamma = t_o/\tau$

$$\gamma_2 = 2.188 \qquad \gamma_3 = 1.414 \qquad \gamma_4 = 1.273.$$

Gamma Factors for Figure 2.2

Staying with Minkowski space-time, we shall now consider the relativistic effects of circular motion (cf. Figure 2.3). Again, we plot several trajectories, and calculate the respective proper times elapsed. The gamma factors are given by (γ_2, γ_3) in the next paragraph. Irrespective of your orbital radius, the gamma factor remains the same (provided tangential velocity remains fixed).

We now consider a more 'exotic' arena within which to perform these calculations. The Schwarzschild metric describes the global geometry in the presence of a massive gravitational object (e.g., a star or a black hole). Again, we present several worldlines and calculate the proper time and gamma factor for each scenario (cf. Figure 2.3),

$$\gamma_2 = 1.033 \qquad \gamma_3 = 1.033 \qquad \gamma_4 = 1.512$$

$$\gamma_5 = 1.287 \qquad \gamma_6 = 1.252.$$

Gamma Factors for Figure 2.3

Whereas in Minkowski space-time the orbital radius has no effect upon the gamma factor, when orbiting a black hole, this is not necessarily true. Observer 4 has a smaller orbit than observer 5, and its effect can be seen in the difference between γ_4 and γ_5. It is important to note that all observed times (t_4, t_5, t_6) are recorded by an observer positioned very far away from the gravitational well, so as not to affect any measurements.

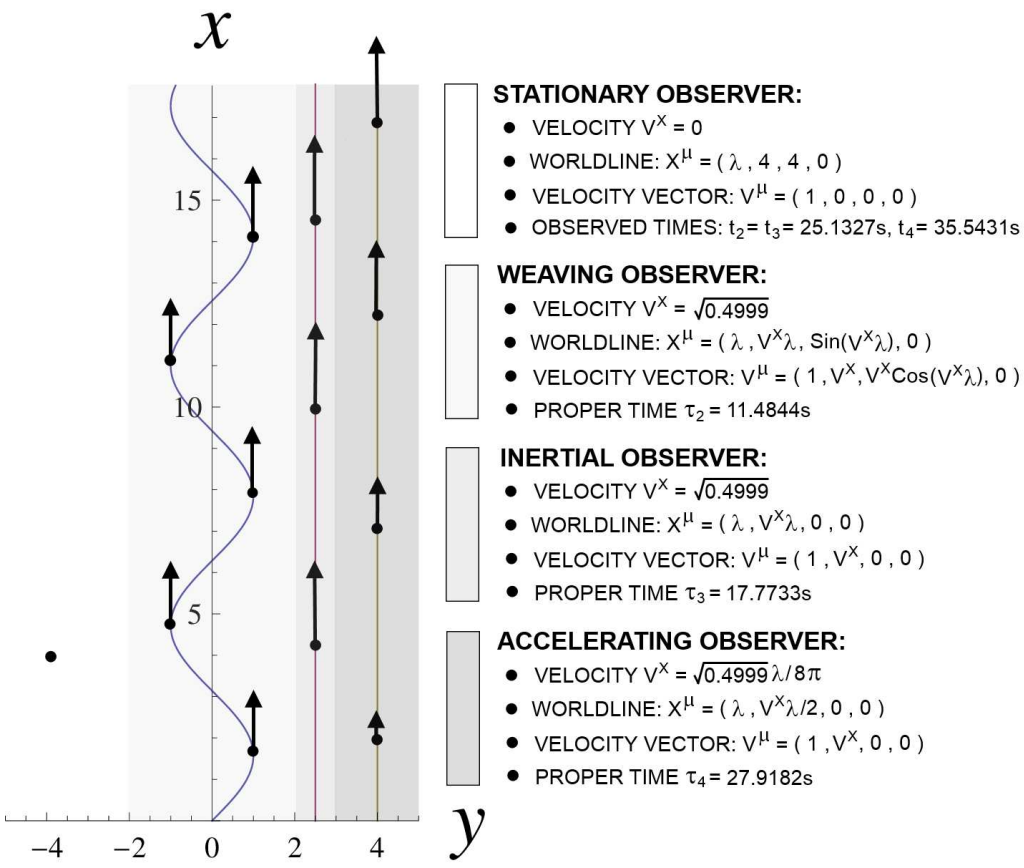

Figure 2.2: Here, we consider several trajectories within the Minkowski space-time. For simplicity, we choose temporal coordinate $t = \lambda$ for all calculations throughout (cf. for further details Appendix B.1.1). The most furtherleft trajectory (i.e., the single point) is that of a stationary observer. This observer notes the elapsed time for other observers to travel from start to finish. Comparing the observed times (t_2, t_3) to the proper times (τ_2, τ_3), we can see that despite arriving at the same time $(i.e., t_2 = t_3)$, observer 2 ages by a lesser amount $(\tau_2 < \tau_3)$. This is because observer 2 is continually accelerating. Finally, we consider an observer 4 accelerating from rest. Calculating the gamma factors for each observer can provide an apt realisation of time dilation effects (cf. main body of text).

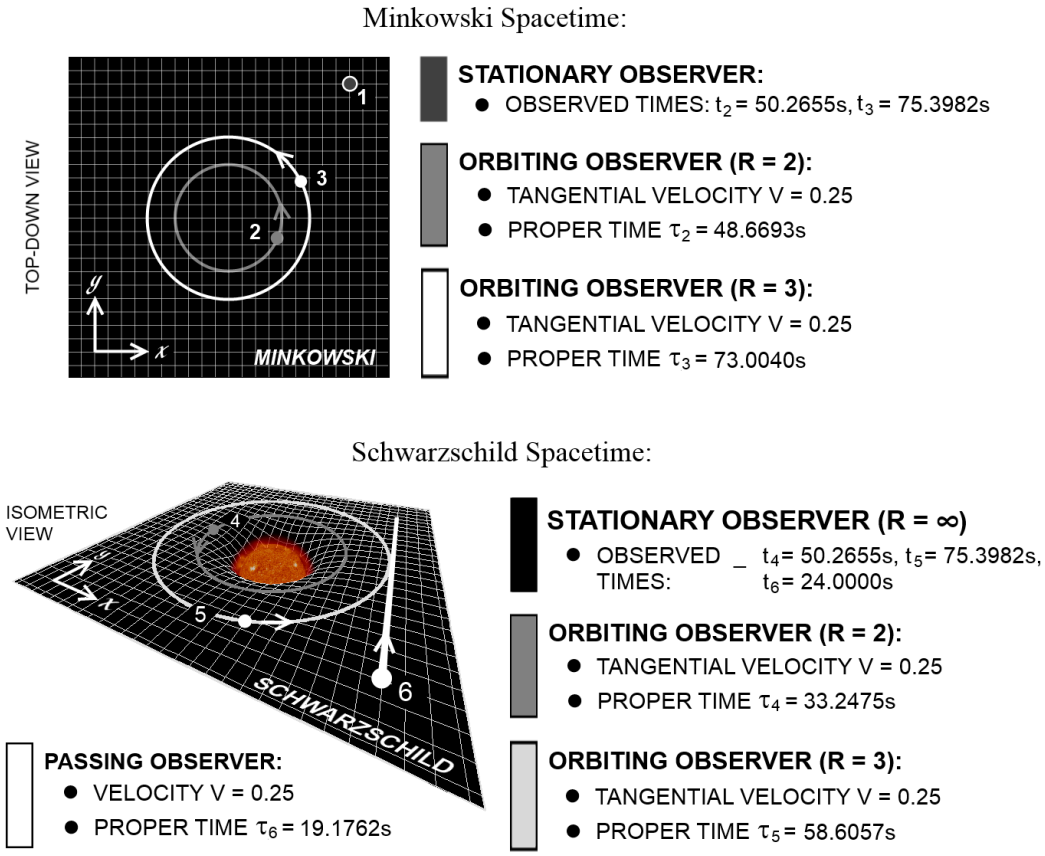

Figure 2.3: This figure outlines the effects of time dilation for circular orbits in both Minkowski and Schwarzschild space-times. By comparing proper times (τ_2, τ_3) to (τ_4, τ_5) respectively, we clearly see that a massive gravitational object can impose a substantial effect. For the Schwarzschild space-time, we assume a Schwarzschild radius $r_s = 1$. All trajectories must reside outside this value in order to avoid being sucked into the black hole. We also position a stationary observer very far away from the object (so as to not be affected), who will again record the elapsed times for the other observers. Finally, we consider an observer who simply passes by the large object.

Chapter 3

Gravitation and Space-Time Curvature

From Figure 1.3, we discussed that light entering the vicinity of a gravitational field will bend as a result. The same would be true if, for example, we replace the light ray with a ball. Suppose now we have an asteroid, which is about to enter the vicinity of a black hole's gravitational field. The asteroid accelerates, but this is not a property unique to the asteroid. The same would be observed for a comet, or even a yellow submarine. Galileo himself proved that all objects, regardless of their mass or physical nature, all fall at the same rate and follow the same path (neglecting air resistance). Thus, we conclude that the acceleration imposed is a property of the space itself. Consequently this implies that gravity not only affects time, but also space - both of which constitute the single entity of space-time. This leads us very nicely to a well known adage in Relativity,

"...space-time grips mass, telling it how to move; and mass grips space-time, telling it how to curve" - John A. Wheeler.

We have deduced then, that gravitational fields modify space in some way. To prove this, we consider another thought experiment. Suppose we have two discs of equal size, one of which rotates and the other remains stationary. Around the circumference of each disc, we attach a large quantity of minuscule yardsticks, the total number of which will tell us the circumference of each disc. However, for the rotating disc, the length of these yardsticks contracts as a consequence of Special Relativity. Therefore we can place more yardsticks into the circumference of the rotating disc. However, this would imply a circumference greater than 2πr because the rotating disc has more yardsticks than the non-rotating equivalent. It follows then that we have two discs of equal size, and yet differ in circumference. Here is the solution; it is the radius which changes, but not in the way one would expect.

Imagine a farmer who is measuring the circumference of a crop circle using its radius. From his point of view, it seems perfectly viable he will gain the correct answer. But suppose the crop circle is now the equator, and that its *apparent* centre is the north pole. Will the circle still have a circumference of 2πr?... yes, but only if the radius is measured directly from the Earth's centre. However, the farmer will measure an actual circumference of $4r$! This is smaller than the value he actually predicts, since he inhabits a spherical geometry (cf. Figure 3.1). Conversely, supposing he were to occupy a hyperbolic geometry, he would measure the circumference to be larger than $2\pi r$. This is analogous to the trouble we faced with the discs. Two discs, two differing values of circumference, imply two differing radii. Since the rotating disc yields a value for circumference greater than 2πr, it follows that this disc occupies a non-Euclidean, hyperbolic geometry. However, recall that the rotating disc carries yardsticks which are constantly changing velocity, and

thus imply an acceleration. This is an acceleration which is directed towards the centre of the disc, and modifies the geometry of space accordingly. Via the equivalence principle, we may assume that gravity (an accelerative field in its own right) will have the same effect.

Of course, there are other means of visualising why gravity is the same as curvature. Perhaps the most convincing is the following scenario. Consider two boats in the Atlantic Ocean, both positioned at the equator and three miles apart. They agree to set a course, due north, at a specified time with equal speed. For a short time interval, it would appear as if the two boats travel parallel to one another. However, due to the Earth's spherical geometry, they decrease their initial separation. This is analogous to the effect of gravitation, in that as time passes by, the separation between two massive objects will decrease.

However, if one wishes to approach curvature from a purely mathematical treatise, we must re-introduce the machinery of manifolds and tensor calculus. A manifold is simply an n-dimensional space, which may be curved, but locally appears flat. This is the same as defining a manifold as smooth, continuous and differentiable, and must have the same dimensionality everywhere. For example, you cannot glue the end of some string to a plane and call this a 'manifold'.

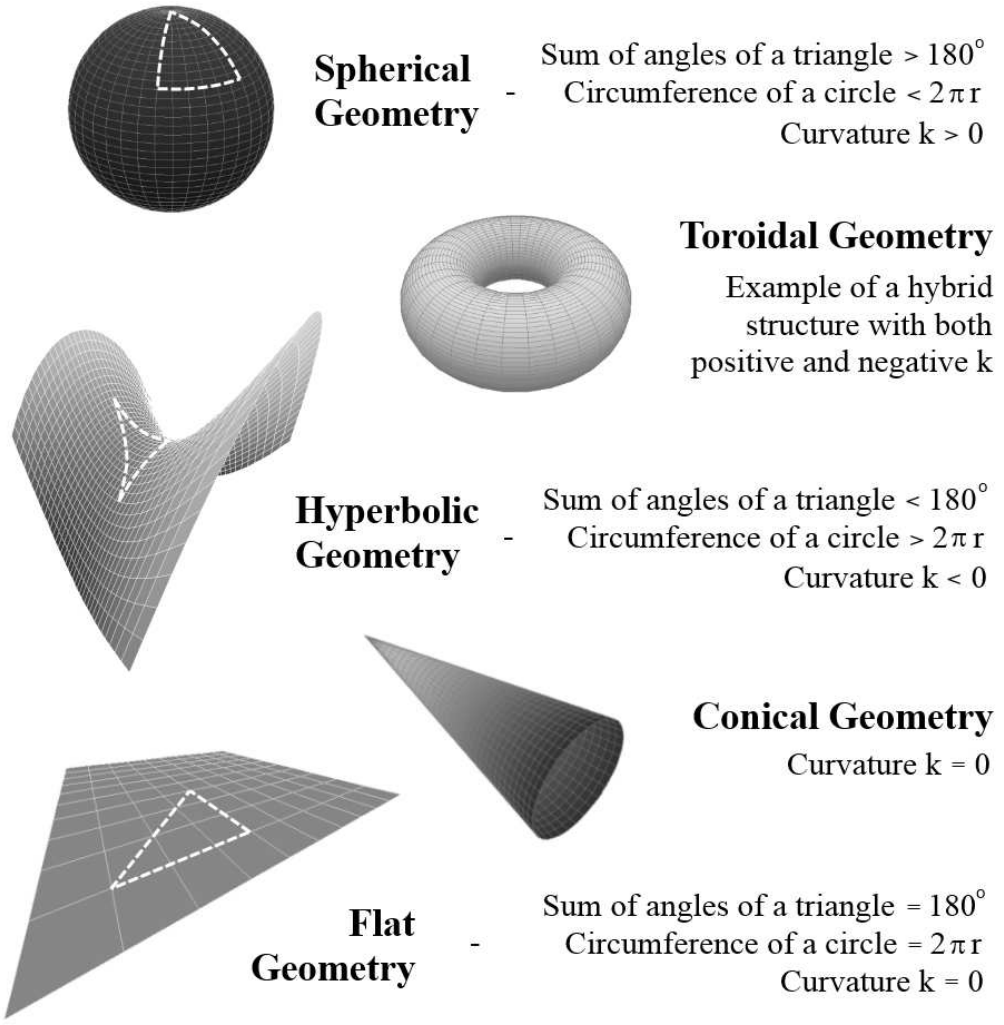

Figure 3.1: Here, we present several geometries and their properties. The three geometries which are commonplace in modern cosmology are those of spherical, hyperbolic and flat. These correspond to a global curvature of $k = (1, -1, 0)$ respectively. Measurements of tiny fluctuations in the cosmic microwave background have indicated that our observable universe is flat to within an error of one percent [4]. In addition, we may also consider hybrid and derivative geometries. The torus is an example possessing both positive and negative curvature - specifically, negative on the inside. Furthermore, the cone is a derivative structure of the standard flat geometry. A geometry is considered to be flat, if it can be formed using a simple piece of paper.

Part II

Non-Linear Systems and Modern Cosmology

Chapter 4

The Simple Pendulum

4.1 Laying the Cosmological Foundations

The bulk of this text has been structured in such a way as to allow the reader to re-ignite their intuition. Most research in physics is, after all, modelled around much simpler systems of which a lot may already be understood. This text constitutes no exception. In reality we begin with the equations specific to our research, and then refer, via analogy, to systems which behave in a similar manner. After a few tweaks, we return to our original starting point with a more concise understanding. In this section, the intellectual ammunition will be supplied before traversing the cosmological battlefield.

As a starting point, we assume a simple pendulum of mass m, fixed radius r, and subject to gravitational constant g. Via transformation of Cartesian to polar coordinates, we derive an expression for velocity v of the bob, acting tangential to its path. It is assumed variables x, y and φ are all time-dependent,

$$x = r\sin\varphi \quad \Rightarrow \quad \dot{x} = r\dot{\varphi}\cos\varphi \ ,$$

$$y = -r\cos\varphi \quad \Rightarrow \quad \dot{y} = r\dot{\varphi}\sin\varphi \ ,$$

$$v^2 = \dot{x}^2 + \dot{y}^2 = r^2\dot{\varphi}^2 \ .$$

We now consider the Lagrangian $L = T - V$, where T and V represent the total kinetic and potential energies respectively. Distinction is drawn here between Lagrangian L and Lagrangian density $\mathcal{L}$, since we are not referring to mass densities within infinitesimal spatial cuts. The mass under consideration is concentrated at a distance r from the point of suspension. Upon considering scalar fields, the general consensus within literature subscribes to Lagrangian density. The key reason for this being that we are not concerned with total energy, but how that energy is distributed throughout spatial domains.

Returning to the pendulum, we proceed with the derivation of the inherent equation of motion. This is achieved via use of the Euler-Lagrange equation (cf. Eq.(4.1)).

$$L = \frac{1}{2}mv^2 - V(\varphi) \ ,$$

$$= \frac{1}{2}mr^2\dot{\varphi}^2 - mg(r\cos\varphi_0 - r\cos\varphi) \ ,$$

where potential energy $V(\varphi)$ is proportional to dy; the change in height of the bob (cf. Figure 4.1). It is here where the non-linearity will arise. As the cosine term is expanded out in Taylor series, the system will become increasingly difficult to solve for the higher order terms of φ.

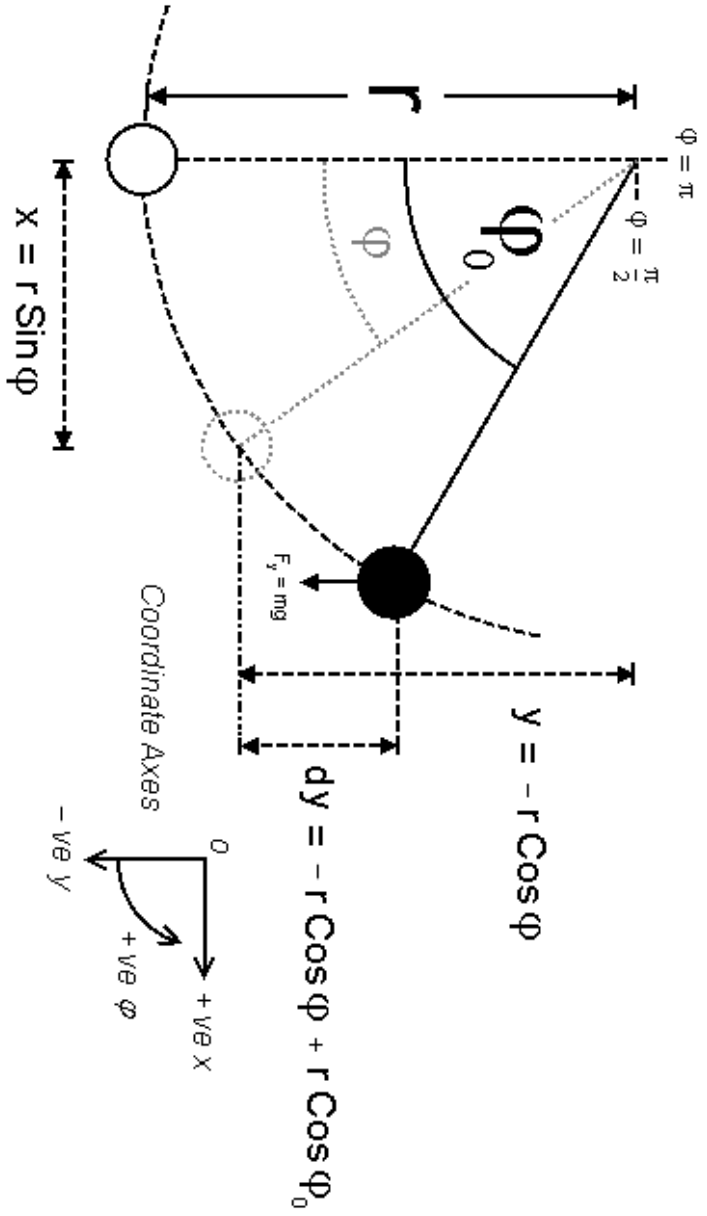

Figure 4.1: Schematic for a pendulum of length r, mass m and subject to gravitational field strength g. Location of the bob is specified for all times via the transformation of Cartesian to polar coordinates.

$$\frac{\partial L}{\partial \varphi} - \frac{d}{dt}\frac{\partial L}{\partial \dot{\varphi}} - \frac{d}{dx}\frac{\partial L}{\partial \varphi_x} = 0 \ , \tag{4.1}$$

$$\frac{\partial L}{\partial \varphi} = -mgr\sin\varphi \ , \qquad \frac{\partial L}{\partial \dot{\varphi}} = mr^2\dot{\varphi} \quad \Rightarrow \quad \frac{d}{dt}\frac{\partial L}{\partial \dot{\varphi}} = mr^2\ddot{\varphi} \ ,$$

$$-mgr\sin\varphi - mr^2\ddot{\varphi} = 0 \ .$$

$$\boxed{\ddot{\varphi} = -\frac{g}{r}\sin\varphi} \tag{4.2}$$

It is at this point one can solve for angle $\varphi(t)$. To provide intuition for how the system will behave, we first constrain the system to small amplitudes of φ (i.e., $\varphi_0 \approx 0$). Thus after Taylor expansion, the higher order terms of $\sin\varphi$ can be disregarded. The corresponding equation of motion is then read as,

$$\ddot{\varphi} = -\frac{g}{r}\,\varphi \ ,$$

for which the following solution exists,

$$\varphi(t) = A\cos\left(\sqrt{\frac{g}{r}}\ t\right) + B\sin\left(\sqrt{\frac{g}{r}}\ t\right) \ . \tag{4.3}$$

Constants A and B are proportional to the initial angle of release φ_0, and angular velocity term $\dot{\varphi}_0$ respectively. This behaviour is characteristic of simple harmonic motion (SHM).

However, as previously mentioned, the solution is valid only for small amplitudes of φ. This is evident via the following scenario. Supposing at time $t = 0$, we have constant $A = \varphi_0 = \pi$, with constant B set to zero. The

pendulum is at its separatrix point (i.e., pointing directly upwards), and will continue to rest at this point unless otherwise acted upon by an external force. Thus angle $\varphi = \pi$; in direct contradiction to (4.3) which continues to imply an oscillating system (cf. Figure 4.2).

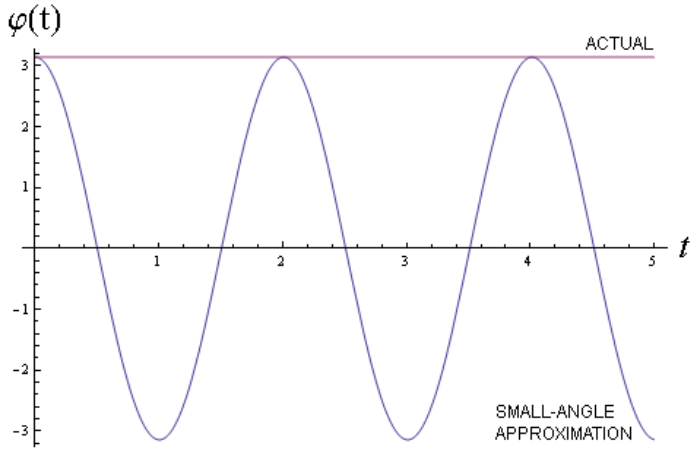

Figure 4.2: The angle subtended by a pendulum as a function of time. Both the exact solution, and that given by the small-angle approximation are plotted for comparison. Initial angle $\varphi_0 = \pi$. Note how that even when subject to no external stimulus, the small-angle approximation continues to exhibit simple harmonic motion.

Additionally, the solution (4.3) is only valid for small values of $\dot{\varphi}_0$. For example, supposing constant $A = \varphi_0 = 0$, with constant B being sufficiently large as to exceed the separatrix value. We would expect the pendulum to complete *at least* one full revolution. Hence, if at any instant $\varphi(t) = B \sin\left(\sqrt{\frac{g}{r}}\, t\right) > \pi$, then $\varphi(t)$ must surpass the point $\varphi(t) = 2\pi$ also. To do so otherwise would imply a defiance of gravity (cf. Figure 4.3).

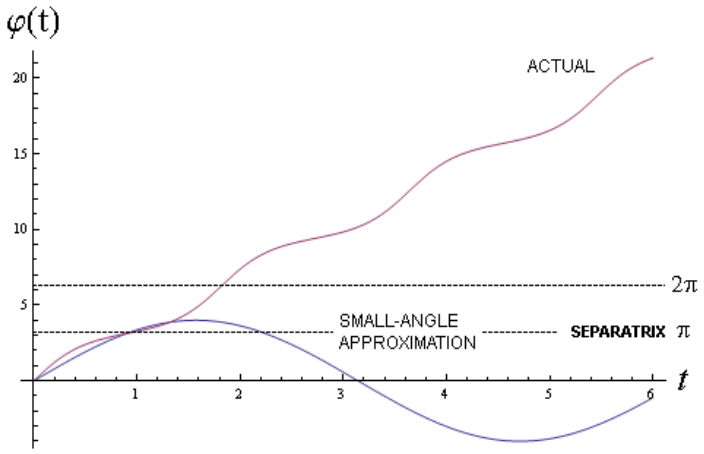

Figure 4.3: The angle subtended by a pendulum as a function of time. Both the exact solution, and that given by the small-angle approximation are plotted for comparison. Initial angle $\varphi_0 = 0$. Initial value of $\dot{\varphi}_0 = 4$ (i.e., sufficiently large to surpass the separatrix).

Fortunately, an exact solution of Eq.(4.2) does exist which takes into consideration all aforementioned drawbacks.

First multiply the equation of motion by $\dot{\varphi}$,

$$\ddot{\varphi} = -\frac{g}{r}\,\sin\varphi \qquad \Longrightarrow \qquad \dot{\varphi}\ddot{\varphi} = -\frac{g}{r}\,\dot{\varphi}\,\sin\varphi\ ,$$

and express as a time-derivative,

$$\frac{1}{2}\,\frac{d}{dt}\left(\dot{\varphi}^2 + \alpha\right) = -\frac{g}{r}\,\frac{d}{dt}\left(\beta - \cos\varphi\right)\ ,$$

where α and β are constants of integration. Constant α represents an initial angular-velocity term, while constant β serves as an initial angular term (or at least some function thereof). Now integrate with respect to time,

$$\frac{1}{2}\left(\dot{\varphi}^2 + \alpha\right) \; = - \; \frac{g}{r} \; \left(\beta - \cos\varphi\right) \; .$$

To understand the form of constants α and β, we solve for initial conditions. At $t = 0$, we have $\varphi = \varphi_0$ and $\dot{\varphi} = \dot{\varphi}_0$. Thus after substituting $\alpha = -\dot{\varphi}_0^2$, we find that constant $\beta = \cos\varphi = \cos\varphi_0$. This gives,

$$\frac{1}{2}\left(\dot{\varphi}^2 - \dot{\varphi}_0^2\right) \; = - \; \frac{g}{r} \; \left(\cos\varphi_0 - \cos\varphi\right) \; . \tag{4.4}$$

For simplicity, we shall first consider the case for $\dot{\varphi}_0 = 0$. After re-arranging for $\dot{\varphi}$, we then express as its reciprocal,

$$\frac{dt}{d\varphi} = \frac{1}{\sqrt{2}} \sqrt{\frac{r}{g}} \; \frac{1}{\sqrt{\cos\varphi - \cos\varphi_0}} \; .$$

Here, the $\pm$ notation of the square roots has been omitted. It should be noted that, depending upon the choice of sign, each will give different solutions. For the purposes of this text, only positive solutions will be considered. Following integration, we then have,

$$t \; = \; \frac{1}{\sqrt{2}} \sqrt{\frac{r}{g}} \; \int_0^{\varphi} \frac{d\varphi}{\sqrt{\cos\varphi - \cos\varphi_0}} \; .$$

Making use of the trigonometric identities;

$$\cos\varphi = 1 - 2\sin^2\frac{\varphi}{2} \qquad \Longrightarrow \qquad \sin\ \frac{\varphi}{2} = \sqrt{\frac{1-\cos\varphi}{2}}\ ,$$

$$t\ =\ \frac{1}{\sqrt{2}}\sqrt{\frac{r}{g}}\int_0^{\varphi}\frac{d\varphi}{\sqrt{1-2\sin^2\frac{\varphi}{2}-\cos\varphi_0}}\ ,$$

$$=\ \frac{1}{\sqrt{2}}\sqrt{\frac{r}{g}}\int_0^{\varphi}\frac{d\varphi}{\sqrt{1-\cos\varphi_0}\sqrt{1-\frac{2\sin^2\frac{\varphi}{2}}{1-\cos\varphi_0}}}\ ,$$

$$=\ \frac{1}{\sqrt{2}}\sqrt{\frac{r}{g}}\int_0^{\varphi}\frac{d\varphi}{\sqrt{2}\ \sin\frac{\varphi_0}{2}\sqrt{1-\frac{\sin^2\frac{\varphi}{2}}{\sin^2\frac{\varphi_0}{2}}}}\ ,$$

$$=\ \frac{1}{2}\ csc\ \frac{\varphi_0}{2}\sqrt{\frac{r}{g}}\int_0^{\varphi}\frac{d\varphi}{\sqrt{1-csc^2\frac{\varphi_0}{2}\ \sin^2\frac{\varphi}{2}}}\ .$$

Making the substitution $\varphi\ =\ 2\theta$, and hence $d\varphi\ =\ 2d\theta$ gives,

$$t\ =\ csc\ \frac{\varphi_0}{2}\sqrt{\frac{r}{g}}\int_0^{\frac{\varphi}{2}}\frac{d\theta}{\sqrt{1-csc^2\frac{\varphi_0}{2}\ \sin^2\theta}}\ .$$

Use the Jacobi elliptic function $F(\varphi\mid m)$ as defined,

$$\boxed{u\ =\ F\ (\varphi\ \mid m)\ =\ \int_0^{\varphi}\frac{d\theta}{\sqrt{1-m\ \sin^2\theta}}\ ,}$$

$$\Rightarrow\ \ t\ =\ csc\ \frac{\varphi_0}{2}\sqrt{\frac{r}{g}}\ F\left(\frac{\varphi}{2}\mid csc^2\ \frac{\varphi_0}{2}\right)\ .$$

We then re-arrange for the incomplete integral F, and attribute this with the following relation,

$$\varphi\ =\ am\ (u\mid m)\ ,$$

$$\Rightarrow \quad \frac{\varphi(t)}{2} = am\left(\sqrt{\frac{g}{r}}\, t \, \sin\frac{\varphi_0}{2} \mid csc^2\frac{\varphi_0}{2}\right) .$$

A plot of this solution can be found in Figure 4.4, for differing values of φ_0.

Numerical Analysis

It is at this point worthwhile to introduce numerical analysis as a potential tool for future study. A system may not necessarily possess an exact solution which can be found via analytical means alone. Numerical analysis provides a safeguard should such complications arise. By specifying the equation of motion and initial/boundary conditions, mathematical software is capable of running a simulated version of events. For comparison, a numerical simulation of the pendulum is included in Figure 4.5, for differing values of φ_0 with $\dot{\varphi}_0$ set to zero.

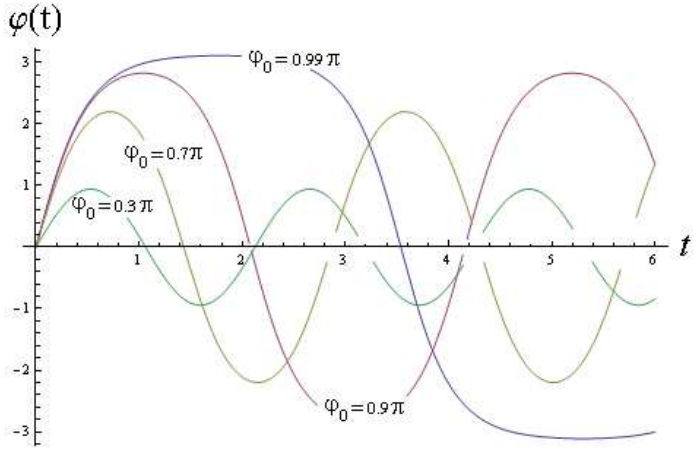

Figure 4.4: The analytic solution for angle φ subtended by a pendulum as a function of time. Various choices of initial angle φ_0 are plotted for comparison.

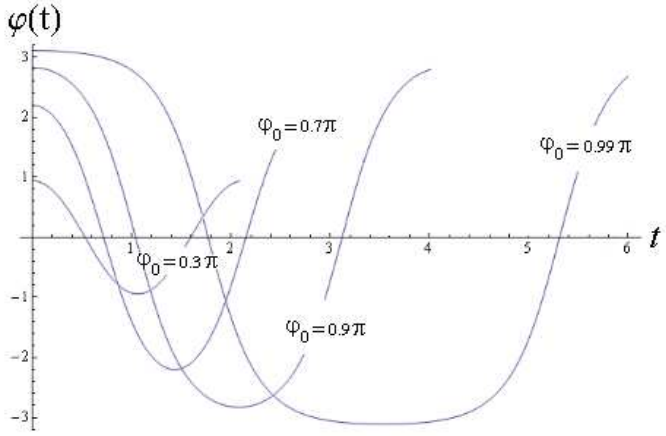

Figure 4.5: Numerical simulations for angle φ subtended by a pendulum as a function of time. Various choices of initial angle φ_0 are plotted for comparison.

Chapter 5

Developments in Modern Cosmology

5.1 Introduction

Ever since 1929 when universal expansion was first observed, physicists have wrestled to develop an explanation as to precisely why. From *steady-state* universe, to *big-bang* and inflationary scenarios; with evermore enticing observational evidence at our disposal, we are beginning to converge upon its precise nature.

Today's state of cosmology is epitomised by the accelerative expansion of the universe, with the so called *dark energy* being responsible for this elusive driving force. Numerous experiments, of which include the WMAP [4] and COBE [5] satellite projects, and further via detailed analyses of Type Ia supernovae [6, 7], have proven to exhibit conclusive evidence that our universe is subject to accelerated growth. In particular, both COBE and WMAP have provided detailed maps of the cosmic microwave background (CMB) within the universe. Such patterns are characteristic of the energy density

structure at the instant of matter–radiation decoupling. The conclusion of both studies, was that the principal constituents of the universe take the form of dark matter and dark energy, of which there is believed to be a constant battle between the two [8, 9]. One pushes the universe to expand, while the other - to collapse. More objective observations present a universe whereby billions of stars are self-organised into spiralling galaxies, which group into larger, more stable galactic clusters. These structures extend further into enormous superclusters that thread throughout the universe, all of which are moving apart. These observed structures which are entirely compatible with inflation theory and big-bang, show that an understanding of dark energy and its role to play structure formation, is one the most fundamental problems in modern cosmology.

More recently, the Planck satellite sought to map the CMB in greater detail than ever before. The mission which was carried out by the European Space Agency (ESA), certainly held true to its word, and after four years of gathering data, Planck delivered its spectacular results [10]. A key feature which has further motivated this thesis, is an apparent lensing of CMB photons due to all intermediary matter. Furthermore, the patterns of localised distortions show no random characteristic, with hot or cold spots moving coherently in a single direction [11]. This implies that structure formation in the universe has been influenced by a well-defined external influence. This thesis will seek to explain how one may obtain such a scenario.

Einstein's remarkable theory of general relativity (cf. Part I), tells us that matter and energy distort space-time. On a cosmic scale, the net matter/energy density of the universe determines its overall space-time curvature. This, in turn, determines the geometry of the universe (i.e., either open, closed or flat). For further details, one may refer to Figure 3.1. Most

believe that the answers reside within the CMB; the primordial light from some half a million years after the big-bang. The geometry of space affects the observed size of hot and cold spots within the CMB. Measurements of these variations have indicated that our observable universe is flat to within an error of one percent [4].

As mentioned by Steinhardt [12], today's universe is part of an endless cycle of big-bangs and big-crunches, with each cycle lasting the order of a trillion years. Despite the amount of matter and radiation in the universe being reset after each cycle, the cosmological constant Λ is not. Instead, this constant gradually diminishes over many cycles to the small value observed today [6, 7, 13, 14]. Indeed, the proposed cyclic universe can incorporate a dynamical mechanism which automatically relaxes the value of the cosmological constant, via a series of quantum phase transitions. This implies that quantum phenomena are essential to our universe. Conversely, it is unclear how the role of other fields or particles (created via quantum fluctuations, as predicted by QCD) must then also exist, and consequently providing the large value for the vacuum energy [15, 16, 17].

Overall, this motivates us to consider two possible contributions within an *effective* cosmological constant Λ_{eff} - one originating from a quintessence scalar field, while the other being some constant Λ, chosen to describe the vacuum energy associated with quantum fluctuations. Within this thesis, the scalar field is considered (likewise to [12, 18]) to be driven by an axion sine-Gordon potential, which shall be elaborated upon in Section 5.3.2. Ultimately, we would like to show that these two contributions may compensate or screen one another entirely.

5.2 Higher/Lower Dimensional Gravity

In 1997, one scientist made a surprising revelation that would come to both haunt and astound the scientific community. In short, his proposal managed to show that Type IIB string theory in 10 dimensional space-time ($\mathrm{AdS}_5 \times S^5$), describes the same physics as that of the maximally supersymmetric $SU(N)$ Yang-Mills theory living on some distant boundary. The theory (formally known as the AdS/CFT correspondence), implies we may be nothing more than a 3D projection, determined by a series of quantum processes over which we have no control. As such, the idea is more commonly referred to as the *'holographic principle'*.

Aside from higher-dimensional theories, the late 1980s played host to an intensive investigation of non-trivial solutions which were targeted specifically at lower-dimensional systems [19, 20, 21, 22, 23, 24, 25]. In particular, [26] presents an in-depth discussion of cosmology within a (1+1) dimensional framework, emphasising the dynamically rich content that can be extracted. Presented are numerous analogues that can be attributed to a (3+1) dimensional counterpart (e.g., gravitational waves, cyclic expansion etc.). Furthermore, the mathematical basis offers a proving ground for establishing connections between classical and quantum gravity [27].

In the thesis presented, we wish to re-ignite the possibility of such lower-dimensional space-time metrics, with the inclusion of the dynamical scalar field φ. When restricting expansion of the universe to that of a (1+1) dimensional framework, this allows the curvature k associated with the Friedmann-Robertson-Walker (FRW) metric to be eliminated via a change of variable - for example, $d\tilde{x}^2/(1-k\tilde{x}^2) \to dx^2$ [27]. Thus, the three cosmological models corresponding to $k = 0, \pm 1$ are physically equivalent to one another. An example of obtaining such a lower-dimensional metric will be demonstrated

in Section 5.4.

5.3 An Approach to Unifying Dark Matter and Dark Energy

5.3.1 Dark Matter

Particle physicists have postulated WIMPs (Weakly Interacting Massive Particles) such as axions, dilatons or neutralinos as dark matter candidates [28, 29], while the nature of dark energy is somewhat more elusive. Heterotic string theory even provides as the candidate, a very light universal axion, convenient to describe the nearly massless pseudoscalar field theory [30].

There is common belief that dark matter and dark energy have nothing to do with each other. However, it has been shown that both may arise from some kind of scalar field [31, 32]. Both may account, on different scales, for inflation [33, 34], dark matter halos of galaxies [35, 36], or even dark matter condensations (the so-called boson stars) [37, 38] as candidates for Massive Compact Halo Objects (MACHOs). Independently, the views of superstring theory [39] suggest an importance of the scalar field with as small a mass as $\sim 10^{-23}$ eV.

In this paper, we follow an approach similar to those of [12, 18, 40], where axion-like scalar models with periodic self-interaction have been studied. Additionally, the authors of [41] show that an axion Bose-Einstein condensate can provide a substantial contribution to the observed rotation curves of galaxies [41], and has probably been observed via gravitational lensing in merging clusters. Recent images captured by the Hubble Space Telescope

(HST) reveal a mysterious clump of dark matter, thought to be the remnants of a massive galactic collision [42]. It seems that the soliton-type dark matter bullets described in [41] provide a natural explanation as to the formation of these dark matter clumps.

5.3.2 Dark Energy

Cosmological Constant: At first glance of the Friedmann equations, such a phenomenon can be described by the cosmological constant, for which many sub-candidates have been proposed (cf. [31, 32] and references within). This was first introduced by Albert Einstein, in order to obtain static, stable solutions to the gravitational field equations. In effect, dark energy was used to prevent the gravitational collapse of the universe. Little was it known at the time, that should spatial inhomogeneities be present post-inflation, these could lead to an unstoppable expansion of the universe. Furthermore, the major crux here is an apparent screening of this parameter; the value predicted by experimental observation [6, 7, 13, 14] remaining inconsistent with the energy scale predictions from particle physics [15, 16, 17]. The observed value of $7 \times 10^{-30} g/cm^3$ (or in natural units $\approx 10^{-35} s^{-2}$), is more than 120 orders of magnitude smaller than the Planck density ($\approx 10^{93} g/cm^3$) at the instant of the big-bang [12]. The value itself is merely representative of an overall averaging of the quantum vacuum fluctuations (the so-called *quantum foam*), and thus the characteristic energy-density associated with empty space [15].

Scalar Fields and Higher Order Curvature Lagrangians: A scalar field, minimally coupled to Einstein's general relativity is equivalent [31, 32, 43, 44] to a modified gravity in the relativistic framework of higher-order

curvature Lagrangians. Such effective Lagrangians may also arise from the low-energy limit of superstrings (cf. for example [45]), which use a non-linear higher-order curvature Lagrangian to explain the present cosmic accelerated expansion. Our choice of Lagrangian will be outlined in Section 5.4.

Scalar fields are something we are very much familiar with. They assign numerical value to all points within the domain for which they exist, the temperature of a room being a prime example. Of all the proposed candidates for dark energy, perhaps the most elegant is the quintessence scalar field φ. The theory posits that some dynamic function (the scalar field), driven by an inherent universal potential $V(|\varphi|)$, constitutes the underlying mechanism for the observed expansion of the universe.

Axions: The existence of scalar fields is also predicted by the standard model of particle physics and quantum chromodynamics (QCD). However, QCD is afflicted with the issue of strong-CP symmetry breaking. Peccei-Quinn theory seeks to remedy this by adding a CP-violating term (the so-called φ parameter) [40, 18] to the Yang-Mills Lagrangian. Not only does the theory predict that φ is representative of some dynamical field rather than some constant numerical value, but because quantum fields produce particles, the theory predicts the existence of a new particle also - the axion. This particle, as previously mentioned, is regarded by many as one of the best motivated candidates for cold dark matter (CDM) [46].

Although the cosmological constant will be able to describe the effects of dark energy, we are curious to consider the contribution of axions - investigating how an induced dynamical scalar field potential may relax this value to within observable parameters. An effective potential $V(|\varphi|)$, arising from the chiral anomaly after integration of the gluon field, is given as follows

[18, 47],

$$V(|\varphi|) = \frac{m^4}{\lambda}\left[1 - \cos\left(\frac{\sqrt{\lambda}}{m}\,\varphi\right)\right] \ . \tag{5.1}$$

Each of the minima within this potential are associated with different vacuum states, each possessing the same energy. The curvature of the potential at each minimum is related to the axion mass m.

Due to the nature of the potential under consideration, a perfectly apt analogy can be associated with that of a pendulum with a time-dependent radius. Since the attached mass is subject to a gravitational potential energy, a consequent effect will be observed upon the radius when transformed into a kinetic equivalent. As such, the precise motivation of this study has been to investigate how a driven scalar field will influence the cosmological radius (i.e., scale-factor) of the universe.

5.4 Hybrid Quintessence

Into our cosmological recipe, we wish to include all we have touched upon in the previous sections. This includes everything from lower-dimensional metrics, to scalar fields, non-linear potentials, higher-order curvature Lagrangians (with a dash of Kaluza-Klein) and even the possibility of some holographic conjecture, useful for describing equivalent physics in two separate mathematical domains.

We begin first with lower-dimensional metrics. Since, the metric outlines the geometry of the space-time domain which we shall be working in, this needs to be carefully defined. An ideal starting point is the FRW metric for an expanding universe. Since, as previously mentioned, the universe is

flat to within an error of one percent [4], we shall assume the curvature k of the universe to be equal to zero. In the familiar (3+1) dimensional universe, the metric in Cartesian coordinates (denoted by $x^\mu = \{t, x, y, z\}$) is given as follows,

$$g_{\mu\nu} = diag[\ -1\ ,\ a(t)^2\ ,\ a(t)^2\ ,\ a(t)^2\ ]\ , \tag{5.2}$$

where $diag[\ldots]$ denotes a diagonal matrix. Here we subscribe to the sign convention ($-$, $+$, $+$, $+$) of Misner-Thorne-Wheeler (MTW) [48]. The standard kinetic term of any Lagrangian density is of the form $g^{\mu\nu}\partial_\mu\varphi\partial_\nu\varphi$, where $\partial_\mu\varphi = \partial\varphi/dx^\mu = \varphi_{,\mu}$. Note that because φ is a scalar quantity, there is no requirement to use the covariant derivative $\nabla_\mu\varphi$. Due to the Einstein summation convention, this gives,

$$\mathcal{L} = -\dot{\varphi}^2 + a(t)^{-2}\left(\varphi_{,x}^2 + \varphi_{,y}^2 + \varphi_{,z}^2\right)\ . \tag{5.3}$$

Assuming a new coordinate $r = \sqrt{x^2 + y^2 + z^2}$, we can use the chain rule of differentiation to modify the spatial derivatives of (5.3) as follows,

$$\frac{\partial\varphi}{\partial x} = \frac{\partial\varphi}{\partial r}\frac{\partial r}{\partial x} = \frac{x}{r}\ \varphi_{,r}\ .$$

Performing the same transformation for both $\varphi_{,y}$ and $\varphi_{,z}$ gives Eq.(5.3) as

$$\mathcal{L} = -\dot{\varphi}^2 + a(t)^{-2}\varphi_{,r}^2\ . \tag{5.4}$$

Thus, our metric can be compactified to a diagonal matrix with only two elements, applicable to a new coordinate system $x^\mu = \{t, r\}$.

Continuing our surgery of the FRW metric, we now seek to add some motivation for including electromagnetic fields. For this, we shall adopt the Kaluza-Klein method, whereby an extra dimension is included. In principle, this alternate dimension (of which we have no experience) may be compactified via a periodic boundary condition to such small size, that it evades even the most powerful particle accelerators. On the other hand, the holographic principle (which requires a holographic dimension), may pay claim to filling this void. To introduce electromagnetic fields, the vector potential A_μ becomes an integral part of the metric [49, 50]. Modifying accordingly the metric implied by Eq.(5.4) gives,

$$\tilde{g}_{\mu\nu} = \begin{pmatrix} -1+\xi A_0 A_0 & \xi A_0 A_1 & \xi A_0 \\ \xi A_1 A_0 & a(t,r)^2 + \xi A_1 A_1 & \xi A_1 \\ \xi A_0 & \xi A_1 & \xi \end{pmatrix} \tag{5.5}$$

where ξ is a constant. This ultimately presents a $(2+1)$ dimensional metric for a new coordinate system $x^\mu = \{t, r, \chi\}$, where χ is an unseen extra dimension. A tilde is chosen to denote a variable in the Kaluza-Klein framework. However, these can be expressed in terms of the original metric (without vector potential A_μ included). The new metric has three overall effects. Firstly, the determinant of the metric transforms as $\tilde{g} = \det|\tilde{g}_{\mu\nu}| \to \xi g$. Secondly, the Ricci scalar curvature $\tilde{\mathcal{R}} \to \mathcal{R} + \frac{1}{4}\xi F_{\mu\nu}F^{\mu\nu}$. Finally, the kinetic term $g^{\mu\nu}\partial_\mu\varphi\partial_\nu\varphi$ becomes gauge invariant, transforming into $|\mathrm{D}\varphi|^2 = (\partial_\mu\varphi - i\sqrt{\xi}A_\mu\varphi)g^{\mu\nu}(\partial_\nu\varphi^* + i\sqrt{\xi}A_\nu\varphi^*)$. Here φ^* denotes the complex conjugate of the scalar field.

Generally speaking, no parameters should depend upon the coordinate χ. Furthermore, it is not often that cosmologists consider a spatially-dependent

scale-factor within the universe. We have chosen to include this, in order to model large-scale spatial perturbations. The premise is analogous to that of Einstein standing on a trampoline (the trampoline representing space-time). The presence of Einstein's mass, stretches the material to a larger degree in the immediate vicinity. Towards the edges of the trampoline, little stretching occurs.

All ingredients have now been thrown into our cosmological soup. All that remains, is to formulate the required Lagrangian density $\mathcal{L}$. For an action $S = \int \mathcal{L}\sqrt{-\xi g}\; d^3x$, this gives,

$$S = \int d^3x \, \frac{\sqrt{-\xi g}}{2\kappa} \left(\mathcal{R} + 2\Lambda + \frac{1}{4}\, \xi F_{\mu\nu} F^{\mu\nu} + \kappa \left[|\mathrm{D}\varphi|^2 - 2V(|\varphi|) \right] \right) \tag{5.6}$$

where gravitational coupling constant $\kappa = 8\pi G$, Λ is the cosmological constant, $F_{\mu\nu} = \partial_\mu A_\nu - \partial_\nu A_\mu$ is the electromagnetic (field strength) tensor, $\mathrm{D}_\mu = \partial_\mu - i\sqrt{\xi} A_\mu$ is the gauge covariant derivative, and $V(|\varphi|)$ is the driving potential (to be chosen in parallel with Eq.(5.1)). The definition of $F_{\mu\nu}$ would appear to oblige the use of a covariant derivative (e.g., $\nabla_\mu A_\nu = \partial_\mu \varphi - \Gamma^\sigma_{\mu\nu} A_\sigma$), since we are working with a non-scalar quantity. However, because the indices of $F_{\mu\nu}$ are anti-symmetric, and the bottom two indices of the Christoffel symbol $\Gamma^\sigma_{\mu\nu}$ are symmetric, this therefore reduces to the standard partial derivative.

Overall, we have a surprisingly beautiful result. Via explicit inclusion of the electromagnetic vector potential A_μ within our metric, we have inadvertently reproduced the Lagrangian term that governs axion electrodynamics $\Delta\mathcal{L} = (\theta e^2/4\pi^2)\mathrm{tr} F_{\mu\nu}\tilde{F}_{\mu\nu}$ (cf. for details [51, 52, 53, 54]). Here, the parameter θ denotes a specific vacuum of the potential $V(\varphi)$.

5.5 Screening the Cosmological Constant

Ultimately, we wish to screen the value of the cosmological constant, to an effective value Λ_{eff} which is more consistent with experimental observation. To achieve this, we begin with the original Einstein-Hilbert action given as,

$$S = \int d^3x \, \frac{\sqrt{-g}}{\kappa} \left(\mathcal{R}_{\text{eff}} + 2\Lambda_{\text{eff}} \right) \ .$$

Comparing with (5.6) yields an effective cosmological constant,

$$\Lambda_{\text{eff}} = \sqrt{\xi}\, \Lambda + \frac{1}{8} \xi^{3/2} \, F_{\mu\nu} F^{\mu\nu} + \kappa \sqrt{\xi} \, \left[\frac{1}{2} \left| \mathrm{D}\varphi \right|^2 - V(|\varphi|) \right] \ , \tag{5.7}$$

and an effective scalar curvature,

$$\mathcal{R}_{\text{eff}} = \sqrt{\xi}\, \mathcal{R} \ .$$

Provided the value of ξ is very small, this may provide a means of screening both values.

Upon variation of the action (5.6) with respect to the background metric $g^{\mu\nu}$, emerge the Einstein-Maxwell field equations. An extended derivation of these equations can be found in Appendix A.9.

$$\begin{aligned} R_{\mu\nu} - \frac{g_{\mu\nu}}{2} \mathcal{R} - g_{\mu\nu} \Lambda = & -\frac{\xi}{2} \, F_{\mu\alpha} F^{\alpha}_{\nu} + \frac{\xi}{8} \, g_{\mu\nu} F_{\sigma\alpha} g^{\alpha\beta} F_{\beta\rho} g^{\rho\sigma} \\ & - \frac{\kappa}{2} \left[(\partial_\mu \varphi - iqA_\mu \varphi)(\partial_\nu \varphi^* + iqA_\nu \varphi^*) + \mu \leftrightarrow \nu \right] \\ & + \kappa g_{\mu\nu} \left[\frac{1}{2} \left| \mathrm{D}\varphi \right|^2 - V(|\varphi|) \right] = -\kappa \, T_{\mu\nu} \ , \end{aligned} \tag{5.8}$$

where we have performed a final symmetrisation process upon the gauge covariant derivative term (cf. Appendix A.5 for details).

Chapter 6

Holographic Methods

6.1 What is Holographic Theory?

Otherwise known as the AdS/CFT correspondence, the theory posits that (under certain semi-classical approximations) a strongly coupled field-theory in D-dimensional Minkowski space-time, can be entirely dual to a theory of quantum gravity living in $D+1$-dimensional Anti-de Sitter (AdS) space-time. Recall that $D = d + 1$, where d is the number of non-holographic spatial dimensions. One approaches the asymptotically flat boundary of AdS space as the holographic dimension $\chi \to 0$, and our boundary theory of quantum gravity reduces to D-dimensionality. It is this holographic dimension χ which will determine our energy scale. We shall also discover that upon consideration of a negative cosmological constant (parametrised by the AdS radius L, or length scale $(1/L)$), one retrieves the AdS Schwarzschild black hole solution. As such, we shall encounter a singularity as $\chi \to \chi_0$ - the scaling of the holographic dimension thus becoming divergent. For a more in-depth discussion as to precisely why an AdS ansatz is considered, one may refer to [55].

6.2 Applications to Condensed Matter

In may seem counter-intuitive for one to consider energy scales that reside well below those at the instant of the big bang. However, there likewise exist many strongly coupled systems in condensed matter physics, which present an inherent computational nightmare. The corresponding theoretical models can only be established upon considering weak approximations and various assumptions, and thus may fail to capture the full spectrum of phenomena at hand. Fortunately, one may employ the AdS/CFT correspondence to study these systems in full detail [56]. We shall discover later that upon considering *holographic superconductors*, one may encounter a new class of black hole solutions that carry charged scalar hair. The two energy regimes (superconductor/black hole) are entirely interchangeable, and constitute a dual theory. Condensed matter systems may thus offer a laboratory environment upon which to study many facets of high-energy phenomena.

6.2.1 Holographic Superconductors

The BCS theory encapsulates a wide range of phenomena exhibited by conventional superconductors [57]. Typically, a *Cooper pair* will condense at low temperatures due to a strong phonon interaction between fermionic quasiparticles. However, there do exist cases (e.g., the high-T_C cuprates) which are known to digress from BCS theory. Possible explanations may include additional interactions (e.g., paramagnons), or systems which can no longer be explained from a quasiparticle standpoint. Such instances when the latter may occur, are upon consideration of a phase transition that is very close to some quantum critical point (i.e., at absolute zero temperature). This critical point then has a cascading effect upon high temperatures. For example,

given an energy band-gap less than some critical value $E_g < E_{gc}$, second order phase transitions (e.g. the onset of superconductivity) may occur at higher temperatures. Such phenomena may all be realised by, for example, varying hole doping concentration, pressure, or an external magnetic field at a given fixed temperature.

6.3 Mathematical Framework

We shall now consider a simple example, demonstrating how one may compute various quantities residing within a boundary field theory. Once again, all simulation code can be referred to in Appendix B.2. We begin by considering a two-component action S as follows,

$$S = -\underbrace{\int d^{D+1}x \, \frac{\sqrt{|g|}}{2\,\kappa}\left(\mathcal{R} + \frac{D(D-1)}{L^2}\right)}_{\text{BULK}} + \ldots$$

$$\int d\chi \underbrace{\int d^{D}x \, \frac{\sqrt{\tilde{\eta}}}{2\,\kappa}\left(\tilde{\mathcal{R}} + \frac{D(D-1)}{L^2} + \frac{1}{4}\,F_{\mu\nu}F^{\mu\nu} + \kappa\left[|\mathrm{D}\psi|^2 - 2V(|\psi|)\right]\right)}_{\text{BOUNDARY}} \quad (6.1)$$

For our example, we shall consider the case $D+1 = 4$ - whereby $D = 3$ constitutes the space-time dimensions $x^\mu = \{t, x, y\}$ (i.e., the boundary). For convenience, we shall temporarily switch to the sign convention $(+, -, -, -)$. Upon consideration of a scale-invariant, asymptotically AdS space-time given by,

$$ds^2 = \frac{L^2}{\chi^2}\left(f(\chi)\,dt^2 - \frac{1}{f(\chi)}\,d\chi^2 - dx^2 - dy^2\right), \quad (6.2)$$

the volume element $\sqrt{|g|} = L^4/\chi^4$ in the bulk part of the action goes to

infinity as one approaches the holographic boundary $\chi \to 0$. Subsequent calculations are then incredibly difficult to solve. However, suppose we consider the contents of the bulk action to be zero (i.e., empty space) - this can then be disregarded. Using the metric components outlined by Eq.(6.2) and setting $\mathcal{R} = -12/L^2$, one can solve the respective differential equation for $f(\chi)$,

$$f(\chi) = 1 + C_1\chi^3 + C_2\chi^4 \ ,$$

where C_1 and C_2 are constants. To obtain the asymptotically flat AdS Schwarzschild black hole solution, one may choose the constants $C_1 = -1/\chi_0^3$ and $C_2 = 0$ giving,

$$f(\chi) = 1 - \frac{\chi^3}{\chi_0^3} \ . \tag{6.3}$$

One must take care to remain dimensionally consistent throughout this process. Note that since our metric (6.2) is scale invariant (i.e., $g_{\mu\nu} = \Omega(\chi)\,\tilde{\eta}_{\mu\nu}$), one can manipulate the term $\Omega(\chi) = L^2/\chi^2$ in such a way to make the system computationally tractable. This process is achieved by absorbing $\Omega(\chi)$ into our original function and coordinate system. By making the following transformations,

$$t \to \frac{\chi^2}{L^2}\,t \ , \qquad \chi \to \chi \ ,$$

$$x \to \frac{\chi}{L}\,x \ , \qquad y \to \frac{\chi}{L}\,y \ , \qquad f(\chi) = \frac{L^2}{\chi^2}\,g(\chi) \ .$$

Eq.(6.2) becomes,

$$ds^2 = g(\chi)\, dt^2 - \frac{1}{g(\chi)}\, d\chi^2 - dx^2 - dy^2 \ ,$$

and rather importantly, we are presented with a non-divergent volume element $\sqrt{|\tilde{\eta}|} = 1$. Furthermore, we obtain a new function,

$$g(\chi) = \frac{\chi^2}{L^2}\left(1 - \frac{\chi^3}{\chi_0^3}\right) \ .$$

The conformal metric $\tilde{\eta}_{\mu\nu}$ shall be used throughout the boundary part of the action (6.1).

The next step is to gain some insight as to the nature of our solutions. The functions we shall be working with, are the scalar field $\psi(\chi)$, and vector potential $A_\mu = \{\ g(\chi)\,\phi(\chi)\ ,\ 0\ ,\ 0\ ,\ 0\ \}$ where $\phi(\chi)$ is the scalar potential. Written explicitly, the action (6.1) takes the following form,

$$S = \int d\chi \int d^D x\, \frac{1}{2\,\kappa}\left(-g''(\chi) + \frac{12}{L^2} - \frac{1}{2}\ \left(\phi(\chi)\, g'(\chi) + \phi'(\chi)\, g(\chi)\right)^2\ \ldots\right.$$
$$\left. \ldots + \kappa\left[g(\chi)\left(q^2\phi(\chi)^2\psi(\chi)\psi^*(\chi) - \psi'(\chi)\psi^{*\prime}(\chi)\right) - 2\,m^2\psi(\chi)\psi^*(\chi)\right]\right) . \quad (6.4)$$

The next step is to derive the two equations of motion by performing a variation of Eq.(6.1) with both $\psi^*(\chi)$ and $\phi(\chi)$ respectively. The key point here is that our boundary terms are required to vanish,

$$\delta S = -\left[g(\chi_0)\psi'(\chi_0)\delta\psi(\chi_0) - g(0)\psi'(0)\delta\psi(0)\right]\ \ldots$$
$$\ldots\ +\ \int d\chi \int d^D x\ \mathcal{O}(\delta\psi)\ .$$

Since we have $g(\chi_0) = 0$ and $g(0) = 0$, one may conclude that $\psi'(0)$ itself does not necessarily vanish. However, previous studies [55, 58] with 'inverse' coordinate systems show that the conditions $\psi'(0) = 0$ and $\psi''(0)$ should be satisfied (i.e., our scalar field falls off asymptotically to a constant value as $\chi \to 0$).

$$\delta S = -\frac{1}{2\,\kappa}\,\left[g(\chi_0)^2\phi'(\chi_0)\delta\phi(\chi_0) - g(0)^2\phi'(0)\delta\phi(0)\right]\;\ldots$$
$$\ldots - \frac{1}{2\,\kappa}\,\left[g(\chi_0)g'(\chi_0)\phi(\chi_0)\delta\phi(\chi_0) - g(0)g'(0)\phi(0)\delta\phi(0)\right] + \int d\chi \int d^D x\,\mathcal{O}(\delta\phi)\,.$$

Again, it is not necessarily clear that one must impose the condition $\phi'(0) = 0$ (i.e., scalar potential falls off asymptotically to a constant value). However, the work of [58] once again verifies this criterion. The full equations of motion in all their glory are as follows,

$$\delta S/\delta\psi^* = 0 \quad \Rightarrow \quad g\psi'' + g'\psi' + (gq^2\phi^2 - 2m^2)\psi = 0\,, \tag{6.5}$$

$$\delta S/\delta\phi = 0 \quad \Rightarrow \quad g\phi'' + 2g'\phi' + (2\kappa q^2\psi\psi^* + g'')\phi = 0\,. \tag{6.6}$$

Upon first inspection, we note a slight discrepancy of dimensionality. We can remedy this by re-parametrising the scalar field mass $m = M/L$, and charge $q = Q/L$. Since the AdS radius L is fixed, these parameters thus remain constant throughout our system. These equations now allow us to determine the precise boundary conditions at $\chi = 0$. Firstly, let us bear in mind what we already know: $g(0) = 1$, $g'(0) = 0$, $g''(0) = 2$, $\psi'(0) = 0$, $\phi'(0) = 0$, $\psi''(0) = 0$ and $\phi''(0) = 0$. Since we prefer not to have vanishing scalar potential (i.e., $\phi(0) \neq 0$), we may conclude from Eq.(6.6) that $\psi(0) = \pm\, i/q\sqrt{\kappa}$. For a

massless scalar field (i.e., $m = 0$), solutions can be approximated as the following,

$$\psi(\chi) = \frac{1}{q\sqrt{\kappa}}\left(i + \psi_3 \frac{\chi^3}{L^3}\right) \quad , \quad \psi^*(\chi) = \frac{1}{q\sqrt{\kappa}}\left(-i + \psi_3 \frac{\chi^3}{L^3}\right) \ , \tag{6.7}$$

$$\phi(\chi) = \phi_0 + \phi_3 \frac{\chi^3}{L^3} \ . \tag{6.8}$$

Note that since we require both $\psi''(0) = 0$ and $\phi''(0) = 0$, the polynomials of both functions should be of order greater than three. Given a change in horizon distance χ_0, we shall now investigate the precise behaviour of constants ψ_3 and ϕ_3. To achieve this, we first substitute Eqs.(6.7,6.8) into the action (6.4), and integrate over the holographic dimension between the limits $\chi = 0$ and $\chi = \chi_0$. We then set $\partial S/\partial\psi_3 = 0$ and $\partial S/\partial\phi_3 = 0$, and solve for both parameters.

We note that the solution investigated is merely an approximation. Of course, one may include higher-order terms (e.g., the scalar field contributions ψ_4, ψ_5) if they so desire. Regardless, from Figure 6.1, we clearly note the disappearance of the ψ_3 contribution for a specific value of horizon radius χ_0. Since the size of a black hole is related to its temperature, most applications of holographic methods focus upon a phase transition that occurs at some critical temperature. For example, the contribution ψ_3 could be related to the order parameter $\langle\mathcal{O}\rangle$ of superconductivity. However, our ultimate objective would be to use this holographic framework within the context of cosmology and inflationary models.

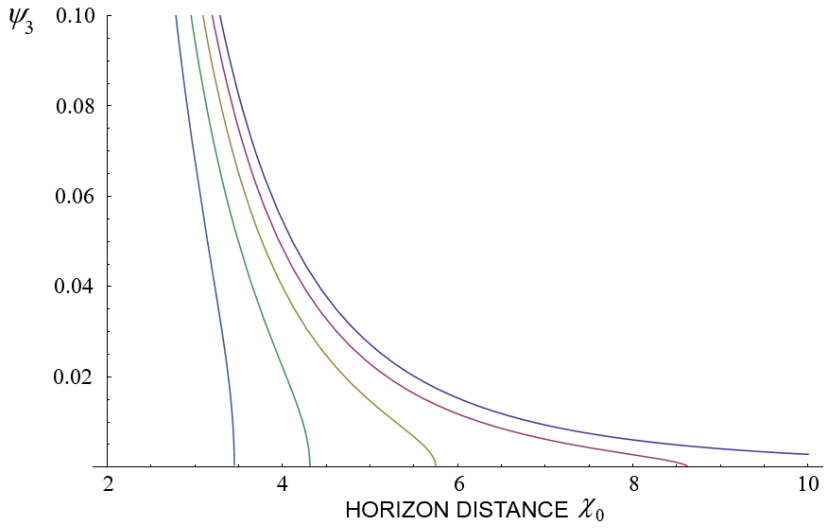

Figure 6.1: Here, we plot the parameter ψ_3 as a function of horizon radius χ_0. The lines (from left to right) correspond to the values $Q = 2.5\,,\, 2\,,\, 1.5\,,\, 1\,,\, 0.5$. For each value of charge Q, a critical point occurs at which the scalar field ψ_3 vanishes.

Chapter 7

Inflationary Cosmology

7.1 Locally Flat Space-Time

We first consider the simplest case of a locally flat space-time, subject to the Minkowski metric $\eta_{\mu\nu} = diag(-1, 1)$. For this, we shall adopt the Hamiltonian formalism, rather than the Lagrangian equivalent. The Hamiltonian density of the system will then be chosen, as necessary, to be proportional to the cosmological constant Λ. From Eq.(5.6), we find that this this should be equal to Λ/κ. The potential chosen to drive the scalar field is the axion potential (5.1). For simplicity, we shall assume no electromagnetic interaction $A_\mu = 0$, and a real scalar field $\varphi = \varphi^*$ which does not depend upon our holographic dimension χ.

The Hamiltonian density is now read as,

$$\mathcal{H} = \frac{\dot{\varphi}^2}{2} + V(\varphi, \varphi_r) \ ,$$

$$\implies \quad \frac{\Lambda}{\kappa} = \frac{\dot{\varphi}^2}{2} + \frac{\varphi_r^2}{2} + \frac{m^4}{\lambda}\left(1 - \cos\left(\frac{\sqrt{\lambda}}{m}\,\varphi\right)\right) \ . \tag{7.1}$$

As a side remark; for a homogeneous scalar field, Eq.(7.1) reduces to the Hamiltonian density for a pendulum. Indeed, the temporal derivative of Eq.(7.1) (with $\varphi_r = 0$), yields the equation of motion for a pendulum. Since much is already known of the simple pendulum as a classical system, we shall not discuss the solutions in detail. However, for an inhomogeneous scalar field $\varphi(t, r)$, Eq.(7.1) has the exact solution in terms of the Jacobi amplitude,

$$\varphi(t, r) = \frac{2m}{\lambda}\,\mathrm{am}\left[\sqrt{\frac{\Lambda\lambda}{2\kappa m^2(1+v^2)}}\,(r + vt) \mid \frac{2\kappa m^4}{\Lambda\lambda}\right] \ . \tag{7.2}$$

Here we subscribe to the notation adopted by Abramowitz and Stegun - $\varphi = am(u|M)$ where $M = k^2$. Plots of this solution can be found in Figure 7.1 for various choice of Λ. For convenience, the constants λ, m, κ and v are normalised to 1. The constant v refers to the velocity of the wave, as a fraction of the speed of light (since the speed of light $c = 1$).

Figure 7.1**(A)** is merely analogous to a pendulum swinging back and forth, whilst travelling through the r-domain with speed v. As we begin to surpass a separatrix value of $\Lambda \approx 2$, the scalar field gains enough angular-momentum to 'roll' into the next vacuum state (i.e., minima) of the potential $V(\varphi)$ (cf. Figure 7.2). Furthermore, as $\Lambda \to 3$, the system becomes analogous to an orbiting body performing circular motion.

However, as previously mentioned, the system is partly analogous to that of a swinging pendulum. It was therefore natural to investigate how a pendulum would behave when given an extra degree of freedom (e.g., a time-dependent radius). Rather co-incidentally, the subsequent equations of mo-

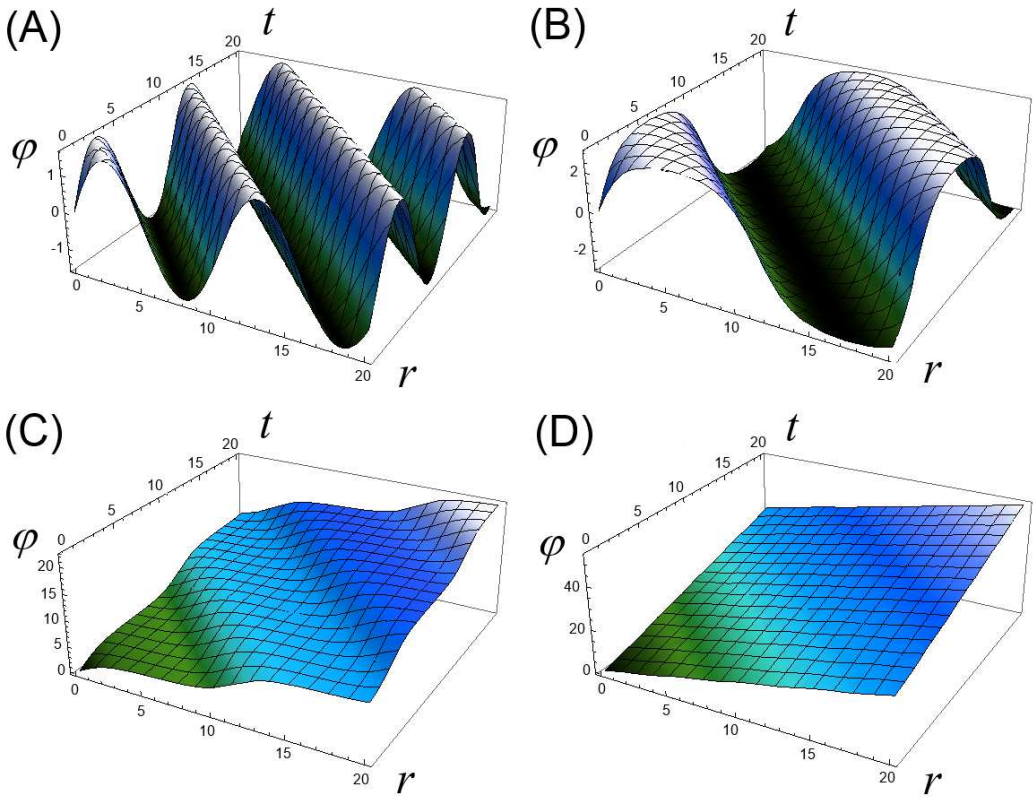

Figure 7.1: Space-time plots of scalar field $\varphi(t, r)$ for various values of cosmological constant Λ. Constants v, λ, m, and κ are all set equal to one. **(A)** $\Lambda = 1$ Here, the system is analogous to a pendulum oscillating back and forth, whilst travelling through the spatial domain with speed v. **(B)** $\Lambda = 1.99$ Similar to the previous case, a pendulum continues to oscillate but with much larger amplitude and time period. **(C)** $\Lambda = 2.01$ Here, the scalar field now has enough energy to roll into the next vacuum state, and continues to increase in value. **(D)** $\Lambda = 3$ The system is now analogous to that of an orbiting body performing circular motion.

tion are identical in nature to those for a quintessence scalar field φ, coupled to a scaling factor a across the spatial component of the metric.

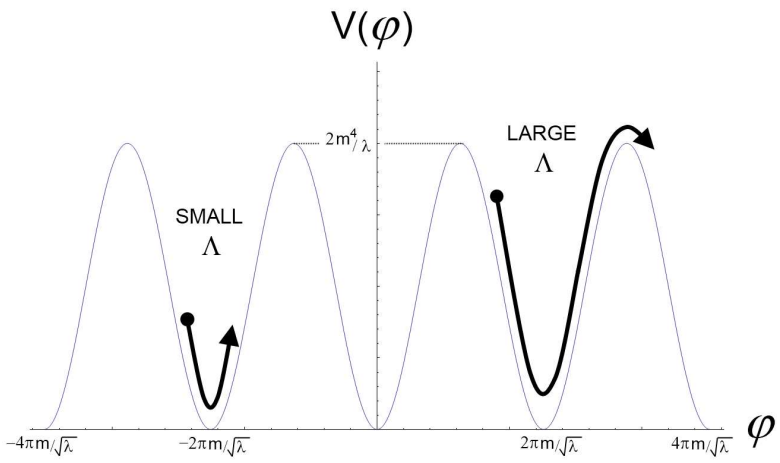

Figure 7.2: Plotted is the axion potential $V(\varphi) = \frac{m^4}{\lambda}\left[1 - \cos\left(\frac{\sqrt{\lambda}}{m}\,\varphi\right)\right]$. Additionally emphasised is the effect of the cosmological constant Λ. For small values of Λ, the scalar field will *roll* inside one of the vacuum states (cf. Figure 7.1**(A)**). These vacuum states are centered about the positions $\varphi = 2\pi nm/\sqrt{\lambda}$, for integer values of n. Conversely, for large values of Λ, the scalar field has the capability to roll from one vacuum state and into another (cf. Figures 7.1**(C-D)**).

7.2 Maximal Spatial Homogeneity: $\varphi(t)$, $a(t)$

We now consider the maximally homogeneous scenario, with a scalar field $\varphi(t)$ coupled to a scale-factor $a(t)$ across the spatial domain. This scaling factor constitutes the g_{11} component of the flat FRW metric to give $g_{\mu\nu} = diag(-1, a^2(t))$. The function is squared to ensure that adjacent points remain a positive distance apart.

All of the necessary parameters are then evaluated, and substituted into

the Lagrangian density $\mathcal{L}$ specified within (5.6). This is then substituted into the gauge covariant Euler-Lagrange equation [59],

$$\frac{\partial\left(\sqrt{-g}\mathcal{L}\right)}{\partial\varphi} - \partial_\mu\left(\frac{\partial\left(\sqrt{-g}\mathcal{L}\right)}{\partial\left(\partial_\mu\varphi\right)}\right) = 0 \ , \tag{7.3}$$

subsequently giving the following two equations of motion:

$$\ddot{\varphi} + \frac{\dot{a}}{a}\dot{\varphi} - \frac{m^3}{\sqrt{\lambda}}\left[1 - \cos\left(\frac{\sqrt{\lambda}}{m}\,\varphi\right)\right] = 0 \ , \tag{7.4}$$

$$\frac{\Lambda}{\kappa} = \frac{\dot{\varphi}^2}{2} + \frac{m^4}{\lambda}\left[1 - \cos\left(\frac{\sqrt{\lambda}}{m}\,\varphi\right)\right] \ . \tag{7.5}$$

Eq.(7.5) has the following exact solution,

$$\varphi(t) = \frac{2m}{\lambda}\,\mathrm{am}\left[\sqrt{\frac{\Lambda\lambda}{2\kappa m^2}}\,t \mid \frac{2\kappa m^4}{\Lambda\lambda}\right] \ . \tag{7.6}$$

The solution for $\varphi(t)$ given above, is now substituted into Eq.(7.4). The subsequent differential equation is then solved for the scale-factor $a(t)$ to give the following Jacobi relation,

$$a(t) = \frac{C_1}{\mathrm{dn}\left[\sqrt{\frac{\Lambda\lambda}{2\kappa m^2}}\,t \mid \frac{2m^4\kappa}{\Lambda\lambda}\right]^2} \ .$$

The constant C_1 merely influences the amplitude of $a(t)$. For simplicity, this has been normalised to one. Plots of this solution can be found in Figures 7.3**(A-D)** for various choice of Λ.

As previously mentioned, for small values of Λ, the scalar field does not have the capability to roll from one vacuum state to another (cf. Figure 7.2).

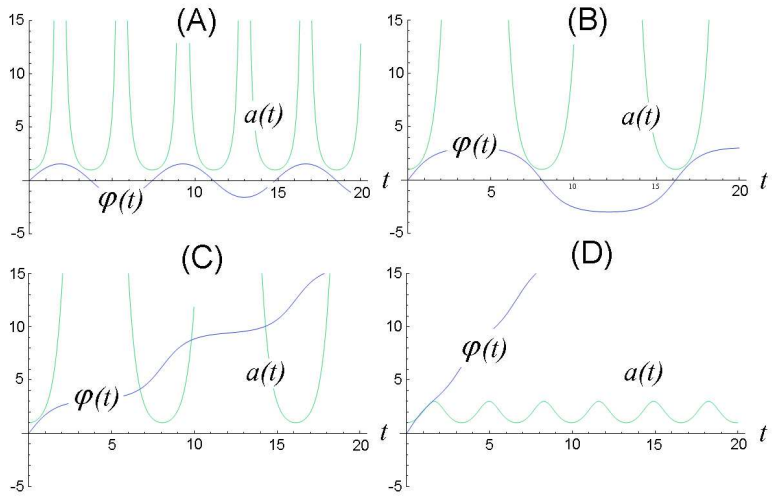

Figure 7.3: Plots of scalar field (blue) and scale-factor (green) for various choice of Λ. Constants v, λ, m, and κ are all set equal to one. **(A)** $\Lambda = 1$, **(B)** $\Lambda = 1.99$, **(C)** $\Lambda = 2.01$, **(D)** $\Lambda = 3$. For values of $\Lambda > 2$, the scalar field continues to increase. As the kinetic $\dot{\varphi}$ contribution diminishes, this energy is transformed into an elastic potential energy, manifesting itself as growth of the scale-factor.

This implies the scalar field will eventually have a $\dot{\varphi}$ (i.e., kinetic) component equal to zero. However, for a pendulum, as $\dot{\varphi}$ approaches zero, this kinetic energy would transform into an elastic potential energy, and thus an expansion of its radius (i.e., our spatial domain). As the constant Λ is increased, so does the overall $\dot{\varphi}$ contribution, and the relative change in scale-factor is found to be much smaller (cf. Figure 7.3**(D)**). Therefore, the constant Λ can be considered to be analogous to a spring-constant, determining the elasticity of the spatial domain. As previously mentioned, if Λ is sufficiently large, the system will exhibit circular motion, and thus the pendulum length (i.e., scale-factor of the universe) will be constant.

7.3 Partial Homogeneity: $\varphi(t)$, $a(t,r)$

In this section, we consider an inhomogeneous scale-factor $a(t,r)$, as this possesses a surprisingly simple result. From this point on, we disregard the values of Λ which result in an infinite expansion (cf. Figures 7.3**(A-B)**).

After performing all the necessary steps, the obtained equations of motion are found to be identical to those for the maximally homogeneous scenario. However, after substituting the solution (7.6) for $\varphi(t)$ into Eq.(7.4), we instead solve the differential equation for a scale-factor $a(t,r)$. The solution is given as the following Jacobi relation,

$$a(t,r) = \frac{C_1(r)}{\mathrm{dn}\left[\sqrt{\frac{\Lambda\lambda}{2\kappa m^2}}\, t \;|\frac{2m^4\kappa}{\Lambda\lambda}\right]^2} \ .$$

This is just the same as before, with the exception that amplitude C_1 now has an added spatial dependence. This allows one to specify the initial perturbation that is present in the scale-factor. Plots are shown in Figure 7.4 for various choice of $C_1(r)$. Within Figures 7.4**(C-D)**, we have $C_1(r) = 2 - \cos(r)$. The boundaries of the spatial domain are specified accordingly, so as to satisfy the topological identification $P_1 = P_2 \leftrightarrow r(P_1) = r(P_2) + 2\pi Rn$ where $n \in \mathbb{Z}$. It is evident from the gridlines, that certain regions are subject to a faster rate of expansion. For Figure 7.4**(E)**, five distinct regions across the spatial domain now undergo an accelerated expansion, with the topological identification remaining in-situ. Figure 7.4**(F)** on the other hand, has the effect of modelling an infinite universe (via the scale-factor) within a finite-sized domain. No topological identifications are specified here.

Physical representations of Figures 7.4**(C)(E)** are shown in Figures 7.5**(A-B)** respectively. Regions of large scale-factor have an observable effect upon

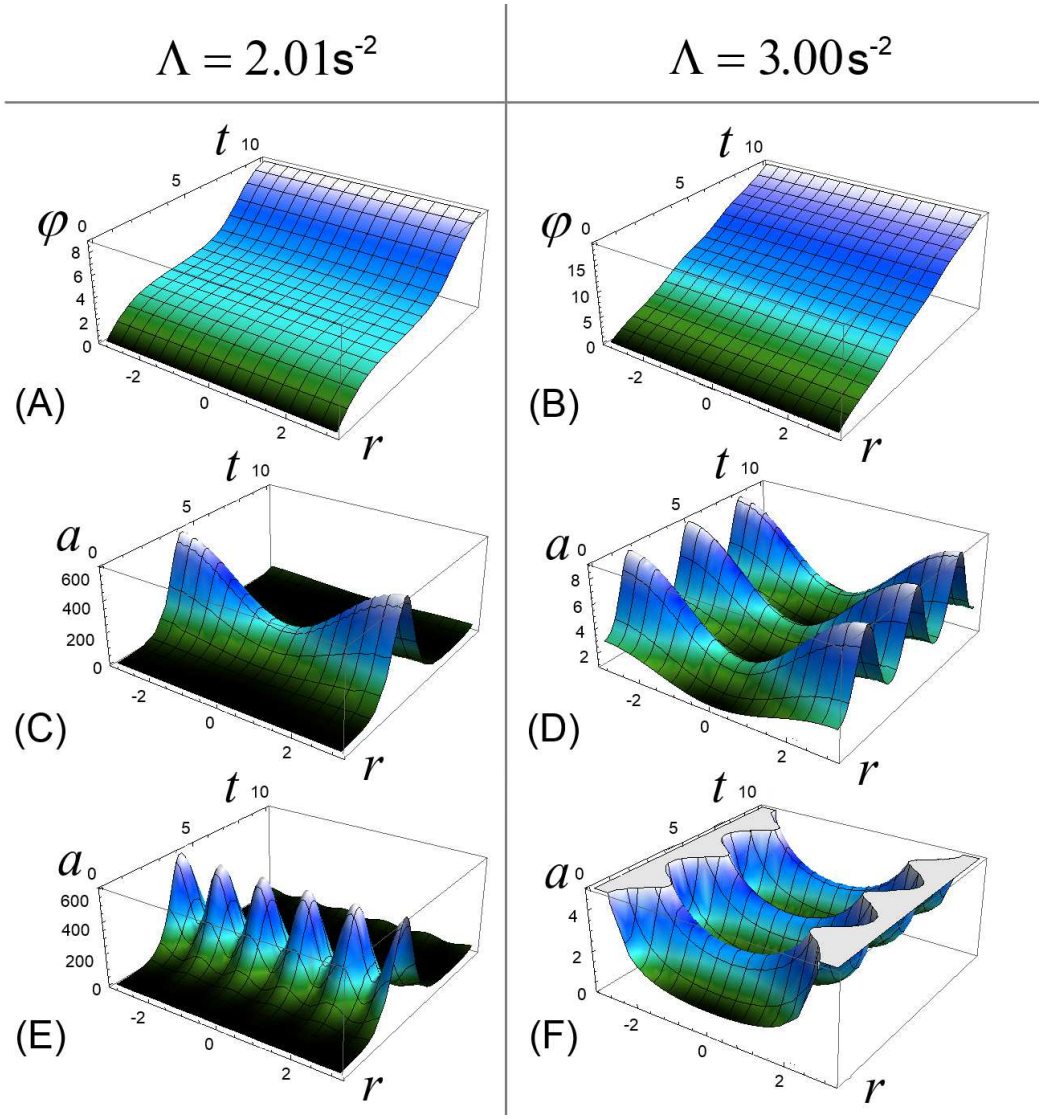

Figure 7.4: **(A-B)** Space-Time plots of a homogeneous scalar field φ for two differing choices of Λ. **(C-D)** Space-Time plots of an inhomogeneous scale-factor with $C_1(r) = 2 - \cos(r)$. **(E)** Space-Time plot of an inhomogeneous scale-factor with $C_1(r) = 2 - \cos(5r)$. **(F)** Space-Time plot of an inhomogeneous scale-factor with $C_1(r) = \sec(r)$.

the r-coordinate grid axis. An observer positioned at $r = 0$ would observe adjacent r-coordinate lines receding at a rate which is proportional to their distance away. This has the desired effect of modelling Hubble's law.

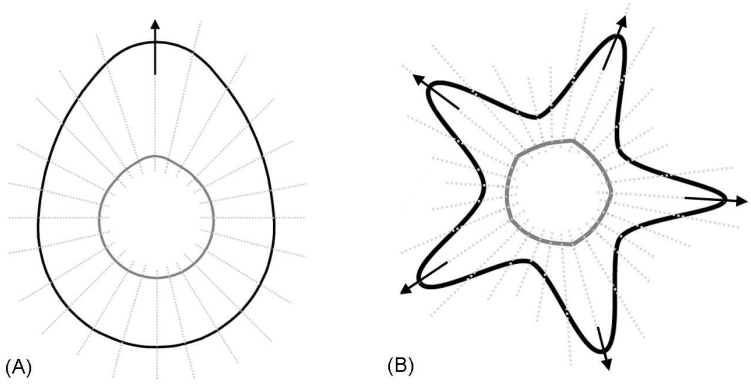

Figure 7.5: (A) A periodic one-dimensional universe with $C_1(r) = 2 - \cos(r)$. The dashed lines indicate the r-coordinate grid axis. The arrow indicates a region with large scale-factor $a(t, r)$. Adjacent points accelerate away from one another with a velocity proportional to their separation; thus mimicking the effect of Hubble's law. **(B)** A periodic one-dimensional universe with $C_1(r) = 2 - \cos(5r)$. The arrows indicate five distinct regions of accelerated expansion.

7.4 Maximum Inhomogeneity $\varphi(t, r)$, $a(t, r)$

For this scenario, the derived equations of motion are as follows;

$$a^3\ddot{\varphi} - a\varphi_{rr} + a^2\,\dot{a}\dot{\varphi} + a_r\varphi_r - a^3\,\frac{m^3}{\sqrt{\lambda}}\sin\left(\frac{\sqrt{\lambda}}{m}\,\varphi\right) = 0\ , \tag{7.7}$$

$$\frac{\Lambda}{\kappa} = \frac{\dot{\varphi}^2}{2} + \frac{\varphi_r^2}{2a^2} + \frac{m^4}{\lambda}\left[1 - \cos\left(\frac{\sqrt{\lambda}}{m}\,\varphi\right)\right]\ . \tag{7.8}$$

By specifying initial conditions at $t = t_0$ that we have $\varphi = \varphi_0$, $\dot{\varphi} = \dot{\varphi}_0$, $\varphi_r = \varphi_{0r}$, and $a_0 = 1$, Eq.(7.8) can once again be solved analytically;

$$\varphi(t = t_0, r) = \frac{2m}{\lambda} \,\mathrm{am}\left[\sqrt{\frac{\Lambda\lambda}{2\kappa m^2(1+v^2)}}\,(r + vt_0) \mid \frac{2\kappa m^4}{\Lambda\lambda}\right] . \tag{7.9}$$

Furthermore, one may also re-arrange Eq.(7.8) for the scale factor $a(t, r)$, and substitute this into Eq.(7.7). This then gives an equation of motion that requires solving only in the scalar field $\varphi(t, r)$.

$$a(t, r) = \sqrt{\frac{\kappa\lambda\,\varphi_r^2}{2\lambda\Lambda - 2m^4\kappa\left[1 - \cos\left(\frac{\sqrt{\lambda}}{m}\,\varphi\right)\right] - \kappa\lambda\dot{\varphi}^2}} . \tag{7.10}$$

This can then solved numerically by specifying (7.9) and its temporal derivative as the initial conditions. Following the computation of $\varphi(t, r)$, $\dot{\varphi}(t, r)$ and $\varphi_r(t, r)$ (cf. Figures 7.6 (left) - 7.7 (left/right) respectively), subject to a certain choice of parameters ($\Lambda = 3$, $\lambda = 1$, $m = 1$, $\kappa = 1$, $v = 0.9$), one may then use Eq.(7.10) to retrieve the scale-factor $a(t, r)$. A plot of this can be found in Figure 7.6 (right). In these figures, the vertical axis corresponds to the time component, and the horizontal axis - the spatial component.

As in previous sections, the constant Λ must be made sufficiently large, so as to prevent an infinite expansion. We also note how Figure 7.6 initially bares some resemblance to Figure 7.4**(D)**. Except here, the scale-factor is propagating through the spatial domain, distorting the geometry of space in the process. Thus at this point, questions arise as to whether dark-energy could be the consequence of an oscillating gravitational wave. These are physical phenomena (although, as of yet, not been detected directly), which

due to their localised energy-density, distort the space-time domain. This energy-density associated with the scalar field can be obtained via the effective cosmological constant of Eq.(5.7) (cf. Figures 7.8-7.9).

7.5 A Deflationary Mechanism?

The model which we study here, sheds light upon the various scenarios of inflation within the primordial universe [60]. These are generally characterised by the choice of initial potential $V_0(\varphi)$ which simulates a temporarily non-vanishing cosmological term [61]. Furthermore, the classification of allowed inflationary potentials and scenarios, has been explored in [61] via the use of the catastrophe theory (cf. for details [62]).

Inflation was first proposed more than 30 years ago now [63], and suggested that our universe may have undergone a period of rapid expansion in its early stages. Three major problems exist in modern cosmology; these are dubbed the horizon, flatness, and monopole problems. The two which we are most concerned with are the flatness and horizon problems. Specifically, why does the universe appear so flat, and almost homogeneous everywhere? Of course, as the universe expands, any initial perturbations in space will be flattened out. Still, how is it that our universe can appear so homogeneous over such vast cosmological scales? For two regions of space that are not in causal contact with each other, how could such an equilibrium between the two be attained? The answer resides within inflation theory, proposing that our universe was once much smaller, with all regions residing within the causal sphere. Inflation would then expand the universe beyond all proportion, to the grandest of scales, and in a mere fraction of a second.

Throughout Figures 7.6-7.9, it is evident our toy model is undergoing

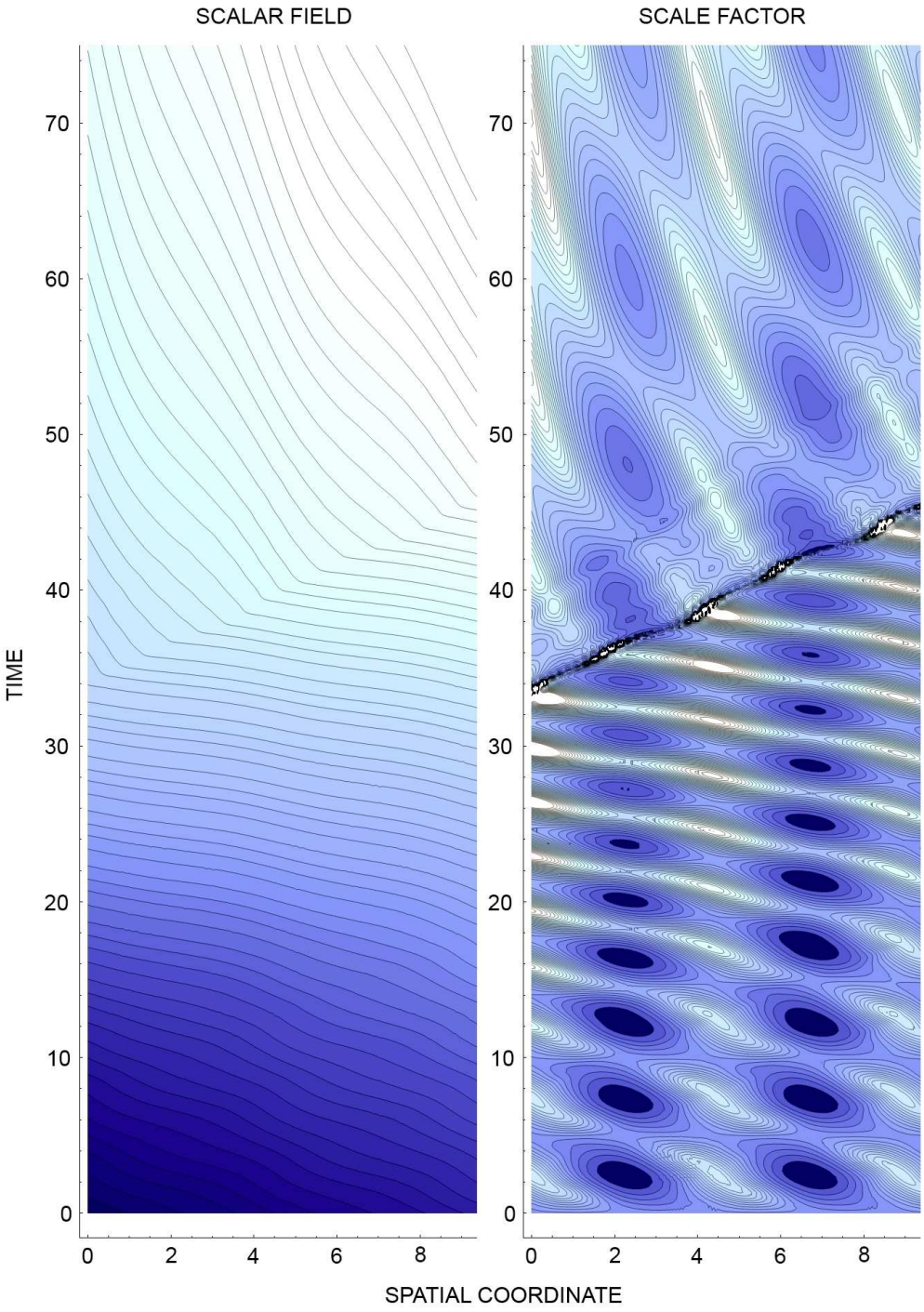

Figure 7.6: The vertical and horizontal axes represent the temporal and spatial dimensions respectively. The scalar field φ (left) is plotted across the range $1.6 < \varphi < 96.0$ (60 contours), with darker colours representing a smaller value. The scale-factor a (right) is plotted across the range $0.657 < a < 2.774$ (30 contours), although higher values are omitted.

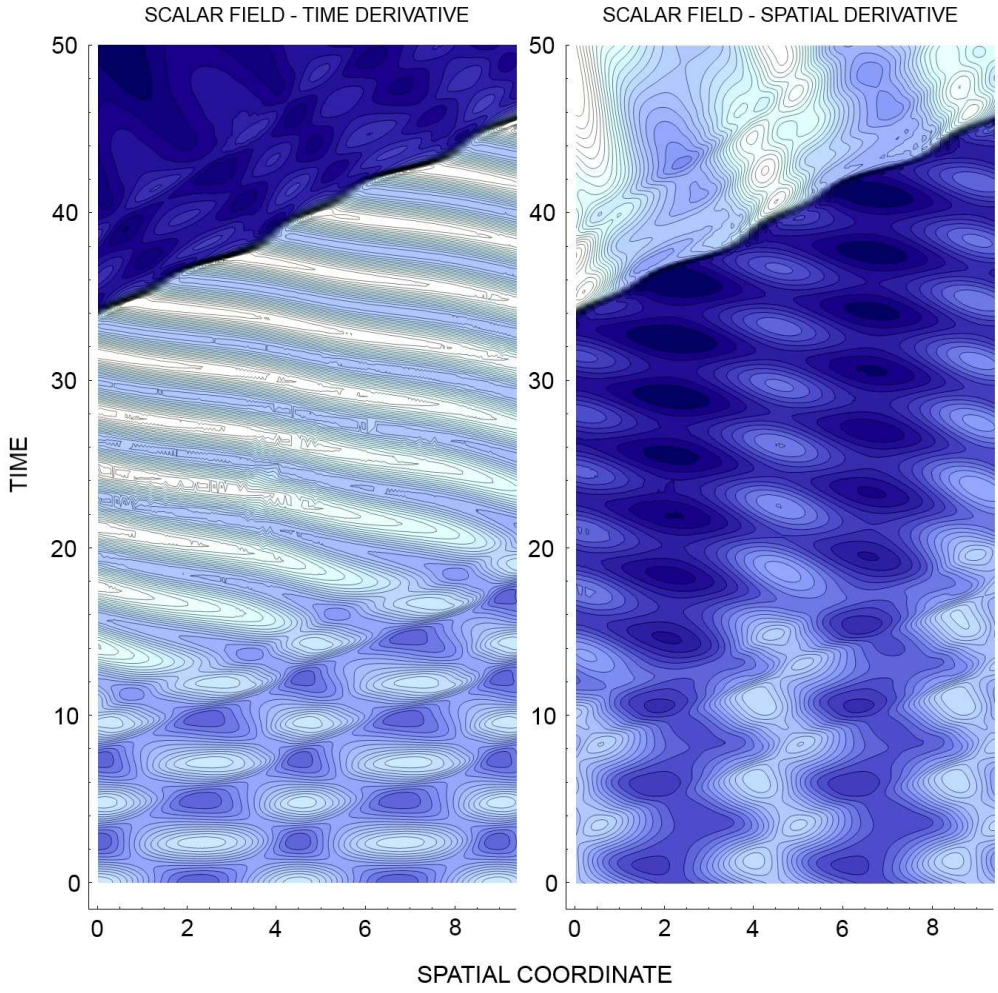

Figure 7.7: The vertical and horizontal axes represent the temporal and spatial dimensions respectively. The time derivative of scalar field $\dot{\varphi}$ (left) is plotted across the range $0.531 < \dot{\varphi} < 2.242$ (30 contours), with darker colours representing a smaller value. The spatial gradient of the scalar field φ_r (right) is plotted across the range $0.5 < \varphi_r < 3.4$ (30 contours).

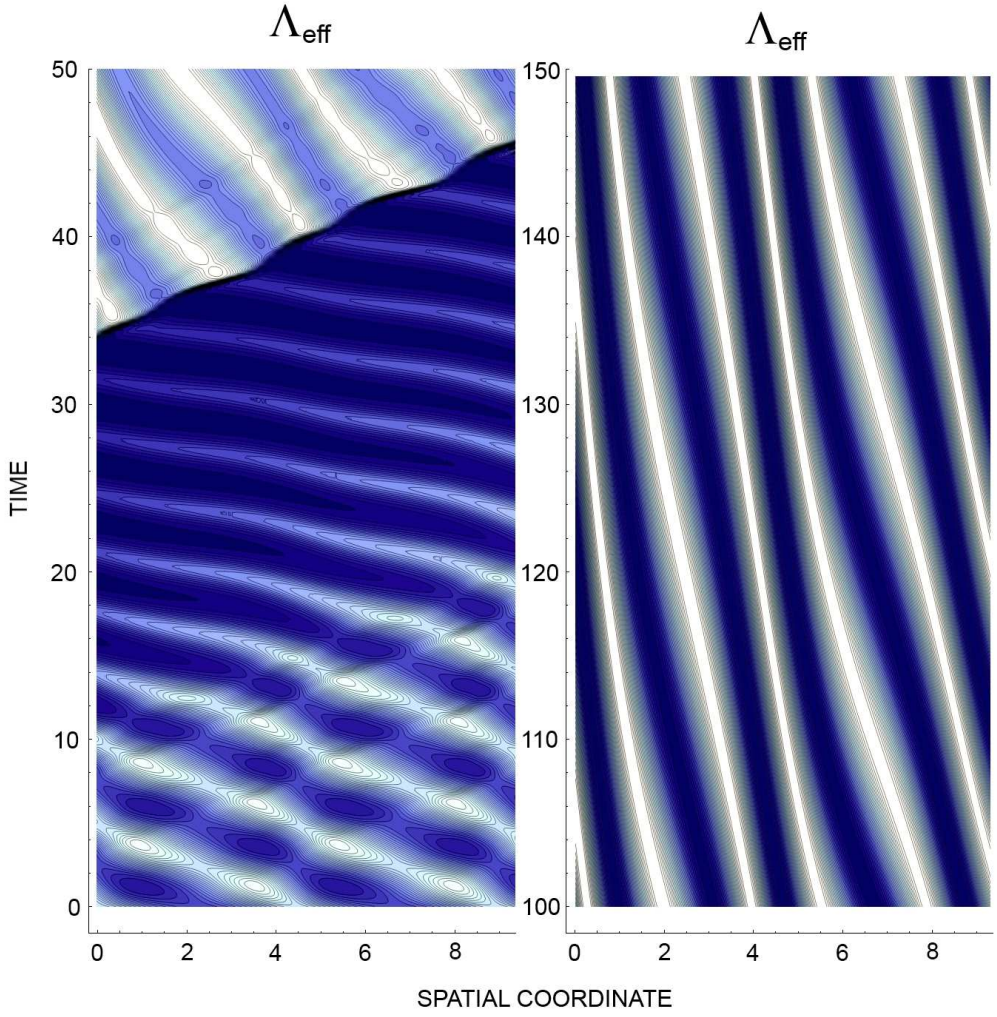

Figure 7.8: The vertical and horizontal axes represent the temporal and spatial dimensions respectively. The effective cosmological constant Λ_{eff} is plotted (left) for times $t \in [0, 50]$ across the range $0.25 < \Lambda_{\text{eff}} < 7.50$ (30 contours), with darker colours representing a smaller value. The effective cosmological constant has also been plotted (right) for later times $t \in [100, 150]$ across the range $2.88 < \Lambda_{\text{eff}} < 8.10$ (30 contours).

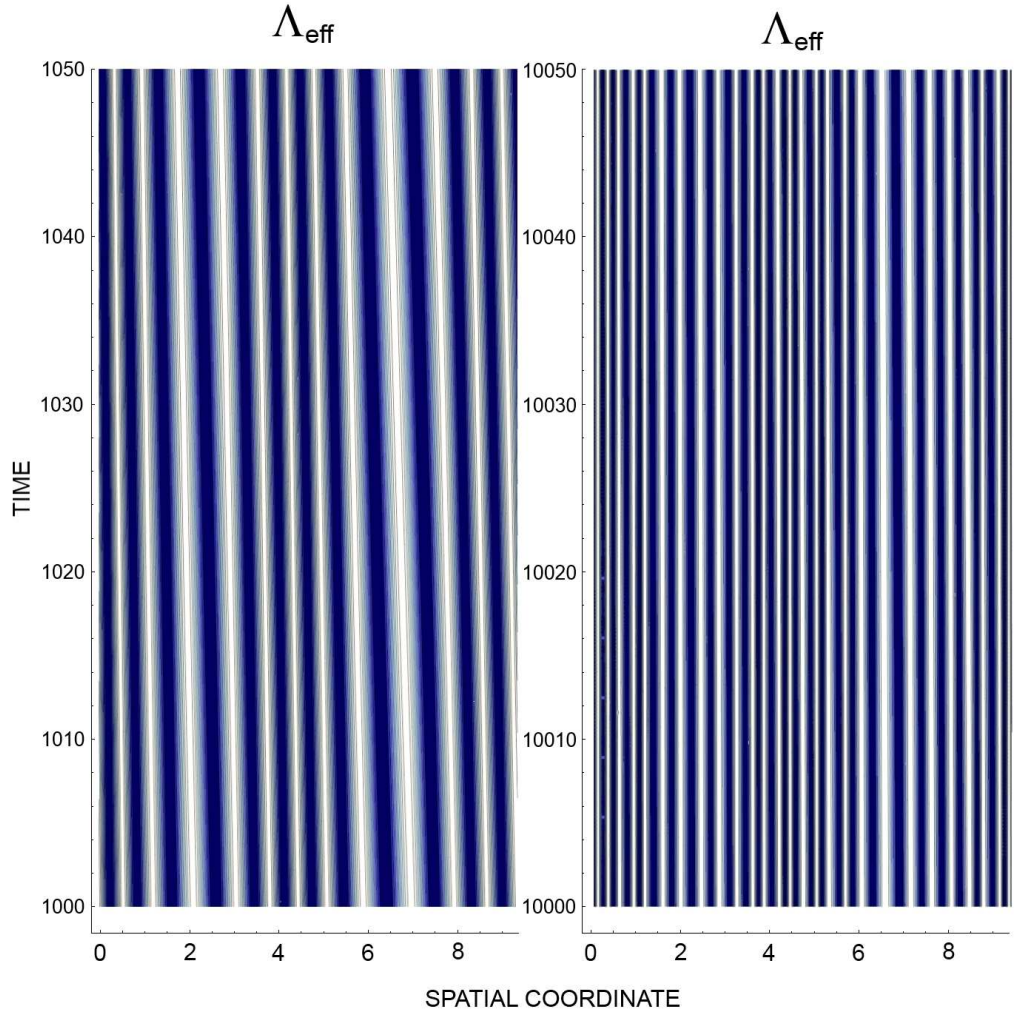

Figure 7.9: The vertical and horizontal axes represent the temporal and spatial dimensions respectively. The effective cosmological constant Λ_{eff} is plotted (left) for times $t \in [1000, 1050]$ across the range $3.57 < \Lambda_{\text{eff}} < 8.16$ (10 contours), with darker colours representing a smaller value. The effective cosmological constant has then been plotted (right) for later times $t \in [10000, 10050]$ across the range $3.76 < \Lambda_{\text{eff}} < 7.52$ (5 contours). The key result to note is that the range of Λ_{eff} is becoming smaller. In this present epoch, one may therefore not expect huge spatial variations within the observed cosmological constant.

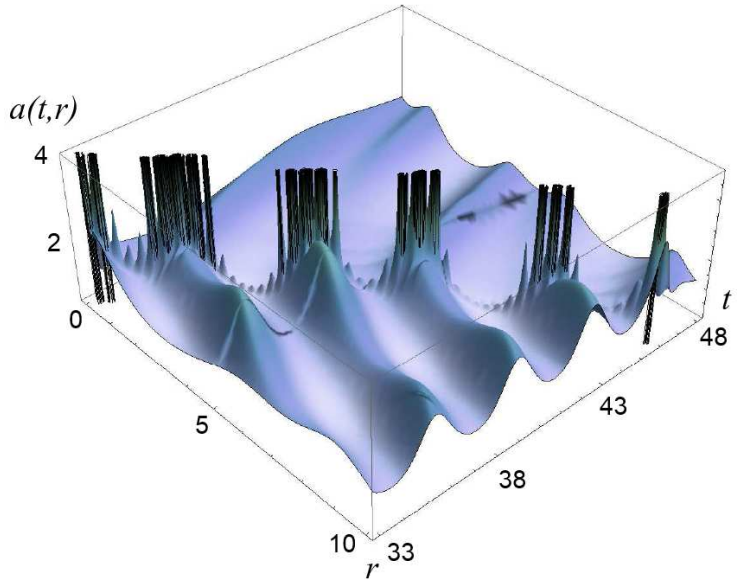

Figure 7.10: Space-time plot of the scale-factor $a(t, r)$. Constants are chosen as $\Lambda = 3$, $\lambda = 1$, $m = 1$ and $\kappa = 1$, subject to initial condition $a_0 = 1$. A highly localised spatial distortion can be seen moving from left to right. This is due to an interaction of the scalar field with the boundary, and propagating back along the system.

different phases of its evolution. At $t = 0$, the scale-factor was specified as homogeneous. However, as t progresses, some regions appear to undergo a cyclic expansion; the amplitude of which becoming successively larger with each oscillation. These peaks correspond to the scalar field $\varphi(t, r)$ traversing various vacuum states of the potential $V(\varphi)$. Supposing the cosmological constant Λ were smaller in value; the scalar field would not traverse as many of these states, thus leading to less oscillations. A value similar to that used in Figure 7.4**(A)**, would present a means of a modelling a single period of expansion.

As t progresses further, the $\dot{\varphi}$ contribution begins to dominate. We also

note the presence of a a highly localised spatial distortion commencing at coordinates (32,0), and ending at (46,9). This distortion is plotted within Figure 7.10 as a three-dimensional space-time plot. This shows a propagating singularity; the consequent effect of which, is a warping of the spatial domain. However, the process (lasting a fraction of a second) is more likened to a deflationary process - regions of space undergo momentary collapse, and then re-expanding. This phenomena propagates throughout the spatial domain with speed v, identical to that of the incident wave. Furthermore, the process is not global, and does not permit all regions of space to be in causal contact with one another. For such a scenario to occur, the scale-factor must be zero at all points in space at a given value of time t. Luckily, there is another possibility which we shall discuss momentarily.

So how does one explain Figure 7.7 after such a process? There is a negligible $\dot{\varphi}$ contribution, yet the scale-factor $a(t, r)$ has not undergone a substantial increase. As we have noted in the previous section; when $\dot{\varphi}$ approaches zero, the scale-factor increases to a large value (cf. Figure 7.3). To explain this, we must first consider the mechanics of the system in all their gory detail. One has a travelling wave solution, which propagates with speed v. When the wave solution reaches the boundary of our system, it then seeks to propagate back along the spatial axis with speed $-v$. The secondary wave carries form of a soliton, and disrupts all further incoming waves, nullifying the $\dot{\varphi}$ contribution. As such, there are instances when φ_r either grows rapidly, or becomes zero. From Eq.(7.10), this has clear consequences for the scale-factor. Furthermore, we note that the scalar field φ as given by Eq.(7.9), is not bound by the speed of light (i.e., the speed v could, in principle, be greater than 1). This implies that the reflected wave from the boundary would also travel with a speed greater than light, and communicate information over

vast distances. This may offer possible reprieve from the horizon problem we highlighted upon earlier.

One must also consider the conservation of energy. With a negligible $\dot{\varphi}$ contribution, the transformed energy can only manifest itself as the scalar gradient φ_r, which competes with both the scale-factor a and axion potential $V(\varphi)$ until equilibrium is reached. As an aside, a physical representation of the scalar field is shown in Figure 7.11. This shows the scalar field increasing by a factor of 2π each time as r increases. As time t progresses, this assembly will typically perform a 'screwing' motion throughout the spatial domain.

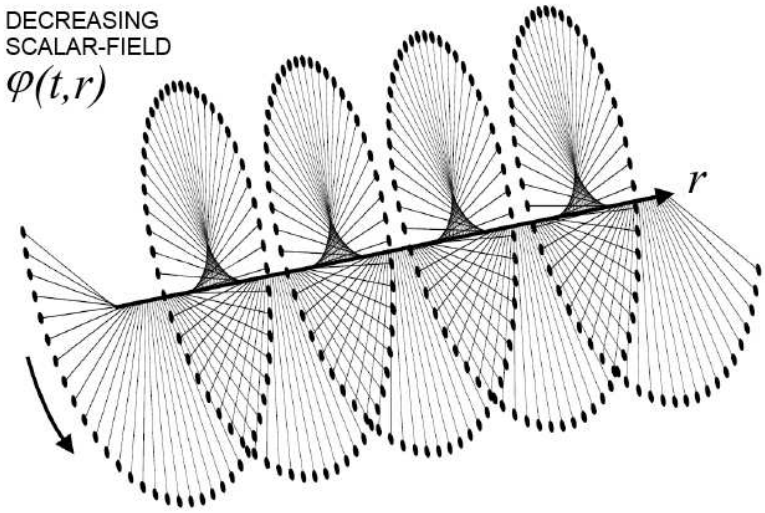

Figure 7.11: A physical representation of the scalar field $\varphi(t, r)$. As time t progresses, the assembly performs a 'screwing' motion throughout the spatial domain and travels with speed v. However, it is viable that the scalar gradient φ_r may compete with both the scale-factor $a(t, r)$ and axion potential $V(\varphi)$, such that no screwing motion occurs. Here, the scale-factor is representative of the length for each individual pendulum. This instance first occurs at the end of the chain - the final pendulum performs a revolution, and then propagates back with speed $-v$, thus affecting all further incoming waves.

7.6 Discussion

We have studied all possible scenarios for modelling dark-energy via the quintessence scalar field φ. Upon considering FRW models, the cosmological constant Λ was found to be analogous to a spring-constant, and thus determining the elasticity of the spatial domain. As the scalar field's kinetic energy (given by the $\dot{\varphi}$ contribution) diminishes, this energy was found to transform into an elastic potential energy. This presented a desirable mechanism for expansion of the spatial domain. The consideration of an added spatial dependence within the scale-factor also lead to a means of modelling Hubble's law. It has been found that irrespective of one's position in the universe, the more distant r-axis grid-lines recede at a faster rate.

When investigating the fully inhomogeneous scenario, solutions for the scale-factor were representative of a wave-like structure, initially propagating through the spatial domain with an oscillatory amplitude. This wave had the overall effect of distorting the geometry as it travelled. For late times, the effective cosmological constant Λ_{eff} is found to be almost homogeneous (cf. Figures 7.8 – 7.9). The variations present are characteristic of the observed microwave background, tiny fluctuations that can ultimately lead to large-scale structure formation of both filaments and voids.

A key result was also the relaxation of both the effective cosmological constant Λ_{eff}, and the effective Ricci scalar $\mathcal{R}_{\text{eff}}$, to be consistent with the small values that are observed today. From Eq.(5.7), it was found that both quantities depend upon some parameter ξ which determines the scaling of some unseen extra dimension. Supposing this extra dimension χ were to be 2π periodic, the parameter ξ would then determine the radius of this extra dimension. For an observed cosmological constant $\Lambda_{\text{eff}} \sim 10^{-35}$, this truly puts into perspective the energies required to access such small dimensions,

well beyond that of any particle accelerator. For convenience, simulation results for Figures 7.8 – 7.9 use a value $\xi = 2\kappa = 2$. However, this value of ξ merely affects the amplitude of the result, and can be scaled as necessary.

At this stage, the cosmological constant looks improbable as an overall contribution to Λ_{eff} (cf. Eq.(5.7)). As mentioned previously, theoretical predictions for the energy-density Λ at the instant of the big-bang [12] are of the order $\sim 10^{93} g/cm^3$. Using Eq.(5.7), to relax this parameter to its present day value of $\approx 7 \times 10^{-30} g/cm^3$, one would require an extra dimension of radius $\sim 10^{-246}$m. Ideally then, this energy-density Λ should be screened completely by the scalar field. What remains, is the tiny contribution from electromagnetism. Electromagnetic phenomena are seldom considered in gravitational physics and cosmology. However, this stark conclusion implies that their effects could be fundamental to understanding why indeed the cosmological constant is so small!

Appendix A

Tensor Calculus

I have condensed the material in this section into as much a concise and simple form as possible for the reader's benefit, whilst maintaining an integrity of the mathematical formulae being dealt with. There are certain aspects one should remain aware of - namely, that different authors adhere to their own conventions and definitions, which may not explicitly be outlined. In particular, one convention which requires clarification is when to use Greek or Latin indices. Throughout this text, Latin indices (e.g., a,b,c,d etc) are used to denote the spatial coordinates. Greek indices (e.g., $\alpha, \beta, \gamma, \delta$ etc) are used to denote the components of space-time (i.e., spatial coordinates and one time coordinate).

A.1 Coordinate Transformation

Supposing we have an n-dimensional space - one then requires n independent coordinates $x^i = \{x^1, x^2, \ldots, x^n\}$ to specify the location of a single point. It is important for the reader not to confuse upper indices throughout this text with those of powers. If powers are being dealt with, the convention shall be

to position them outside the bracket - for example, $(\ldots)^n$. We are most familiar with the world of three spatial dimensions (i.e., $x^i = \{x^1, x^2, x^3\}$). If these coordinate axes are then altered in some manner, for example via translation or rotation, the components will differ from previous entries. Since the newly formed coordinates $x^{i'}$ are related to the previous set x^i via some transformation f, the coordinates $x^{i'}$ are functions of x^i. Conversely, the coordinates x^i can be expressed as functions of the $x^{i'}$ via a corresponding inverse transformation g.

$$x^{i'} = f(x^1, x^2, \ldots, x^n) \quad or \quad f : x^i \longrightarrow x^{i'} \ , \tag{A.1}$$

$$x^i = g(x^{1'}, x^{2'}, \ldots, x^{n'}) \quad or \quad g : x^{i'} \longrightarrow x^i \ . \tag{A.2}$$

A.2 Kronecker Delta

We first recall the chain rule of differentiation for functions of multiple variables. Applying this to Eq.(A.2) gives the following:

$$\begin{aligned}
\frac{\partial x^i}{\partial x^1} &= \frac{\partial x^i}{\partial x^{1'}}\,\frac{\partial x^{1'}}{\partial x^1} + \frac{\partial x^i}{\partial x^{2'}}\,\frac{\partial x^{2'}}{\partial x^1} + \ldots + \frac{\partial x^i}{\partial x^{n'}}\,\frac{\partial x^{n'}}{\partial x^1} \ , \\
\frac{\partial x^i}{\partial x^2} &= \frac{\partial x^i}{\partial x^{1'}}\,\frac{\partial x^{1'}}{\partial x^2} + \frac{\partial x^i}{\partial x^{2'}}\,\frac{\partial x^{2'}}{\partial x^2} + \ldots + \frac{\partial x^i}{\partial x^{n'}}\,\frac{\partial x^{n'}}{\partial x^2} \ , \\
&\ldots \quad \ldots\ldots\ldots \quad \ldots\ldots\ldots \quad \ldots \quad \ldots\ldots\ldots \ , \\
\frac{\partial x^i}{\partial x^j} &= \frac{\partial x^i}{\partial x^{1'}}\,\frac{\partial x^{1'}}{\partial x^j} + \frac{\partial x^i}{\partial x^{2'}}\,\frac{\partial x^{2'}}{\partial x^j} + \ldots + \frac{\partial x^i}{\partial x^{n'}}\,\frac{\partial x^{n'}}{\partial x^j} \ .
\end{aligned} \tag{A.3}$$

This is more conveniently expressed as,

$$\frac{\partial x^i}{\partial x^j} = \sum_{k=1}^{n} \frac{\partial x^i}{\partial x^{k'}} \frac{\partial x^{k'}}{\partial x^j} \ . \tag{A.4}$$

Since our coordinates are independent of one another, the left hand side of Eq.(A.4) is zero unless $i = j$, in which case it is unity. Thus the following statement holds,

$$\sum_{k=1}^{n} \frac{\partial x^i}{\partial x^{k'}} \frac{\partial x^{k'}}{\partial x^j} = \delta^i_j \ , \tag{A.5}$$

where δ^i_j is the Kronecker delta.

A.3 Summation Convention

If an index appears in the RHS of an equation exactly twice (a so called dummy index), then it is assumed that this index is summed for all values 1 to n. This is the basis of the Einstein summation convention. Thus Eq.(A.5) becomes,

$$\frac{\partial x^i}{\partial x^{k'}} \frac{\partial x^{k'}}{\partial x^j} = \delta^i_j \qquad\qquad (k = 1 \ldots n) \ .$$

Due to interchangeability of coordinates x^i and $x^{i'}$, the following is also valid,

$$\frac{\partial x^{i'}}{\partial x^k} \frac{\partial x^k}{\partial x^{j'}} = \delta^{i'}_{j'} \qquad\qquad (k = 1 \ldots n) \ .$$

A.3.1 Indexing: A Quickfire Method

To ensure that an equation is consistent, we analyse the indexing of our coordinate system. Incidentally, it should be mentioned that a superscript in

the denominator of a fraction is treated as a subscript, and that a subscript in the denominator is treated as a superscript. Indices within the numerator retain their usual meaning. In general, the following criteria must be met:

- If unprimed indices i, j, k appear as superscripts on the LHS of an equation, they must appear as superscripts on the RHS of the equation.
- If unprimed indices i, j, k appear as subscripts on the LHS of an equation, they must appear as subscripts on the RHS of the equation.
- If primed indices i', j', k' appear as superscripts on the LHS of an equation, they must appear as superscripts on the RHS of the equation.
- If primed indices i', j', k' appear as subscripts on the LHS of an equation, they must appear as subscripts on the RHS of the equation.
- If an index appears as both superscript and subscript on the RHS of an equation, then it is not necessary for that index to appear on the LHS. This is a process known as the *contraction* of indices (cf. Appendix A.3: Summation Convention).

As a brief example, let us check for consistency within the Riemannian curvature tensor,

$$R^{\rho}_{\sigma\mu\nu} = \partial_{\mu}\Gamma^{\rho}_{\nu\sigma} - \partial_{\nu}\Gamma^{\rho}_{\mu\sigma} + \Gamma^{\rho}_{\mu\lambda}\Gamma^{\lambda}_{\nu\sigma} - \Gamma^{\rho}_{\nu\lambda}\Gamma^{\lambda}_{\mu\sigma} \qquad (\lambda = 1 \ldots n) \ .$$

Each of the terms has ρ as a superscript, and $\mu\nu\sigma$ as subscripts. The λs in the final two terms contract with one another, thus λ does not appear on the LHS of the equation. Both of these terms are summed over for values of $\lambda = 1 \ldots n$. As another example, consider the following,

$$a^{r'_1, r'_2, \ldots, r'_m}_{p'_1, p'_2, \ldots, p'_q} = a^{s_1, s_2, \ldots, s_m}_{t_1, t_2, \ldots, t_q} \left(\frac{\partial x^{r'_1}}{\partial x^{s_1}} \frac{\partial x^{r'_2}}{\partial x^{s_2}} \cdots\cdots \frac{\partial x^{r'_m}}{\partial x^{s_m}} \right) \left(\frac{\partial x^{t_1}}{\partial x^{p'_1}} \frac{\partial x^{t_2}}{\partial x^{p'_2}} \cdots\cdots \frac{\partial x^{t_q}}{\partial x^{p'_q}} \right)$$

The sets of primed indices $\{r'_1, r'_2, \ldots r'_m\}$ and $\{p'_1, p'_2, \ldots p'_q\}$ are present on both sides - the set $\{r'_1, r'_2, \ldots r'_m\}$ appearing as the superscript, and the set $\{p'_1, p'_2, \ldots p'_q\}$ as the subscript. The sets of unprimed indices $\{s_1, s_2, \ldots s_m\}$ and $\{t_1, t_2, \ldots t_q\}$ both occur twice on the RHS. These indices thus contract with one another, and do not appear on the LHS of the equation. Each contracted variable, $s_1, s_2 \ldots$, $t_1, t_2 \ldots$ etc is summed for all values 1 to n; returning $(n)^{m+q}$ different terms; thus the convenience of tensor analysis. By applying these simple conditions laid out to forthcoming equations, the reader will become more familiar with indexing of variables.

A.4 Contravariants, Covariants and Invariants

A.4.1 Contravariant Vectors

Any direction in an n-dimensional space can be represented by the basis vectors dx^i and $dx^{j'}$, within the coordinate systems x^i and $x^{j'}$ respectively. One of the simplest coordinate transformations is achieved by applying the rotation matrix to some vector λ^i. Here the x^i coordinate system is rotated through an angle θ. This transformation will alter the individual components of the vector, although its magnitude will remain unchanged (cf. Figure A.1).

$$\lambda^{j'} = ROT(\lambda^i) = \begin{pmatrix} \cos\theta & -\sin\theta \\ \sin\theta & \cos\theta \end{pmatrix} \begin{pmatrix} \lambda^1 \\ \lambda^2 \end{pmatrix} = \begin{pmatrix} \frac{\partial x^{1'}}{\partial x^1} & \frac{\partial x^{1'}}{\partial x^2} \\ \frac{\partial x^{2'}}{\partial x^1} & \frac{\partial x^{2'}}{\partial x^2} \end{pmatrix} \begin{pmatrix} \lambda^1 \\ \lambda^2 \end{pmatrix} .$$

This yields the following two equations,

$$\lambda^{1'} = \frac{\partial x^{1'}}{\partial x^1}\lambda^1 + \frac{\partial x^{1'}}{\partial x^2}\lambda^2 \qquad (j = 1) \ , \tag{A.6}$$

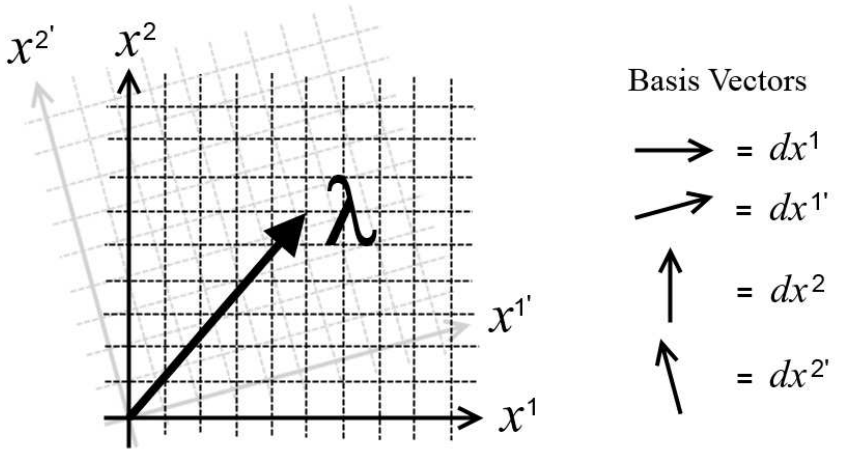

Figure A.1: Applying the rotation matrix to a vector leaves its magnitude unchanged

$$\lambda^{2'} = \frac{\partial x^{2'}}{\partial x^1}\lambda^1 + \frac{\partial x^{2'}}{\partial x^2}\lambda^2 \qquad (j = 2)\ . \tag{A.7}$$

or more generally speaking,

$$\lambda^{j'} = \lambda^i \frac{\partial x^{j'}}{\partial x^i} \qquad (i = 1 \ldots n)\ . \tag{A.8}$$

Note that in general, the Jacobian matrix $\partial x^{j'}/\partial x^i$ may not necessarily be a rotation matrix; its use here was unique to the problem at hand. In the event of such a relation as with Eq.(A.8), the two entities λ^i and $\lambda^{j'}$ in their respective coordinate systems are said to transform as contravariant vectors. Multiplying Eq.(A.8) by $\partial x^k/\partial x^{j'}$ gives,

$$\frac{\partial x^k}{\partial x^{j'}}\lambda^{j'} = \lambda^i \frac{\partial x^{j'}}{\partial x^i}\frac{\partial x^k}{\partial x^{j'}} = \lambda^i \delta^k_i = \lambda^k\ . \tag{A.9}$$

We note that the components of a contravariant vector are denoted via a single upper index. Thus a contravariant vector is defined as a contravariant tensor of first order or rank-1.

Covariant Vectors

The gradient of a function f with respect to coordinates $x^{j'}$, gives a covariant vector $\lambda_{j'}$. Conversely, the gradient of a function f with respect to coordinates x^i yields a covariant vector λ_i. Recall that a superscript in a denominator is treated as a subscript - hence the components of a covariant vector are denoted via a single lower index. More formally, a covariant vector is defined as a covariant tensor of first order or rank-1,

$$\frac{\partial f}{\partial x^{j'}} = \lambda_{j'} = \frac{\partial f}{\partial x^i}\,\frac{\partial x^i}{\partial x^{j'}} = \lambda_i\,\frac{\partial x^i}{\partial x^{j'}}\ . \tag{A.10}$$

A.4.2 Invariants

Finally we discuss an invariant; a scalar which remains unchanged under coordinate transformation. Multiplying Eq.(A.8) by Eq.(A.10) gives,

$$\lambda^{j'}\lambda_{j'} = \lambda^i\,\frac{\partial x^{j'}}{\partial x^i}\,\lambda_i\,\frac{\partial x^i}{\partial x^{j'}} = \lambda^i\lambda_i = \lambda^j\lambda_j\ . \tag{A.11}$$

In other words, if the same index appears once as both subscript and superscript (e.g. $\lambda^{i'}\mu_{i'}$), and no other indices appear, then we are dealing with an invariant. The same is true for unprimed indices (e.g., $\lambda^i\mu_i$), but not when a prime is mixed with an unprimed index such as $\lambda^{i'}\mu_i$.

A.4.3 Transforming Tensors

Suppose for a primed coordinate system $x^{i'}$, we let $\lambda^{i'}$ and $\mu^{j'}$ represent the components of two contravariant vectors, and $\lambda_{i'}$ and $\mu_{j'}$ represent the components of two covariant vectors. One can then formulate second order (i.e., rank-2) tensors via multiplication of these entities,

$$a^{i'j'} = \lambda^{i'}\mu^{j'} \ , \qquad a_{i'j'} = \lambda_{i'}\mu_{j'} \ , \qquad a^{i'}_{j'} = \lambda^{i'}\mu_{j'} \ , \tag{A.12}$$

where $a^{i'j'}$ is a contravariant tensor, $a_{i'j'}$ is a covariant tensor, and $a^{i'}_{j'}$ a mixed tensor, each of rank-2. Using the relations already shown in Eqs.(A.8,A.10),

$$\begin{aligned} a^{i'j'} &= \lambda^k \frac{\partial x^{i'}}{\partial x^k}\, \mu^l \frac{\partial x^{j'}}{\partial x^l} = a^{kl} \frac{\partial x^{i'}}{\partial x^k} \frac{\partial x^{j'}}{\partial x^l} \ , \\ a_{i'j'} &= \lambda_k \frac{\partial x^k}{\partial x^{i'}}\, \mu_l \frac{\partial x^l}{\partial x^{j'}} = a_{kl} \frac{\partial x^k}{\partial x^{i'}} \frac{\partial x^l}{\partial x^{j'}} \ , \\ a^{i'}_{j'} &= \lambda^k \frac{\partial x^{i'}}{\partial x^k}\, \mu_l \frac{\partial x^l}{\partial x^{j'}} = a^k_l \frac{\partial x^{i'}}{\partial x^k} \frac{\partial x^l}{\partial x^{j'}} \ . \end{aligned} \tag{A.13}$$

One can even transform tensors of higher order as follows:

A contravariant tensor of rank m

$$a^{r'_1,r'_2,\ldots r'_m} = a^{s_1,s_2,\ldots s_m} \left(\frac{\partial x^{r'_1}}{\partial x^{s_1}} \frac{\partial x^{r'_2}}{\partial x^{s_2}} \cdots\cdots \frac{\partial x^{r'_m}}{\partial x^{s_m}} \right) \ . \tag{A.14}$$

A covariant tensor of rank m,

$$a_{r'_1,r'_2,\ldots r'_m} = a_{s_1,s_2,\ldots s_m} \left(\frac{\partial x^{s_1}}{\partial x^{r'_1}} \frac{\partial x^{s_2}}{\partial x^{r'_2}} \cdots\cdots \frac{\partial x^{s_m}}{\partial x^{r'_m}} \right) \ . \tag{A.15}$$

A mixed tensor of rank $m+q$, contravariant of the m^{th} order and covariant of the q^{th} order,

$$a^{r'_1,r'_2,\ldots r'_m}_{p'_1,p'_2,\ldots p'_q} = a^{s_1,s_2,\ldots s_m}_{t_1,t_2,\ldots t_q} \left(\frac{\partial x^{r'_1}}{\partial x^{s_1}} \frac{\partial x^{r'_2}}{\partial x^{s_2}} \cdots\cdots \frac{\partial x^{r'_m}}{\partial x^{s_m}} \right) \left(\frac{\partial x^{t_1}}{\partial x^{p'_1}} \frac{\partial x^{t_2}}{\partial x^{p'_2}} \cdots\cdots \frac{\partial x^{t_q}}{\partial x^{p'_q}} \right) \ .$$

A.5 Symmetry

Any rank-2 tensor of indices 'ij' is simply a matrix, where rows and columns are denoted by the 'i' and 'j' components respectively.

Symmetric: If a tensor remains unaffected upon interchange of two indices, then the tensor is considered symmetric with respect to those indices. If this applies to all indices present, the tensor itself is symmetric.

$$a_{ij} = \begin{pmatrix} 1 & 2 & 3 \\ 2 & 4 & 5 \\ 3 & 5 & 6 \end{pmatrix} = a_{ji} = (a_{ij})^{\mathrm{T}} = \begin{pmatrix} 1 & 2 & 3 \\ 2 & 4 & 5 \\ 3 & 5 & 6 \end{pmatrix}$$

Symmetric Tensor with $n(n+1)/2$ different entries.

Skew-Symmetric: If a change in sign appears upon interchange of any two indices, then the tensor is considered skew-symmetric (anti-symmetric) with respect to those indices. If this applies to all indices, the tensor itself is skew-symmetric. Note that two consecutive permutations of indices would reproduce the original sign.

$$a_{ij} = \begin{pmatrix} 0 & 1 & 2 \\ -1 & 0 & 3 \\ -2 & -3 & 0 \end{pmatrix} = \text{-}a_{ji} = -(a_{ij})^{\mathrm{T}} = - \begin{pmatrix} 0 & -1 & -2 \\ 1 & 0 & -3 \\ 2 & 3 & 0 \end{pmatrix}$$

Skew-Symmetric Tensor with $n(n-1)/2$ different entries.

Asymmetric: If upon interchange of two indices there is a complete change in result, then the tensor is considered to be asymmetric with respect to

those indices. If this applies to all indices, the tensor itself is asymmetric.

$$a_{ij} = \begin{pmatrix} 1 & 2 & 3 \\ 4 & 5 & 6 \\ 7 & 8 & 9 \end{pmatrix} \neq a_{ji} = (a_{ij})^{\mathrm{T}} = \begin{pmatrix} 1 & 4 & 7 \\ 2 & 5 & 8 \\ 3 & 6 & 9 \end{pmatrix}$$

Asymmetric Tensor with n^2 different entries.

One may of course make a tensor a_{ijk} either symmetric or skew-symmetric via the processes of symmetrisation and skew-symmetrisation respectively. To make a tensor symmetric, round brackets ( ) enclose all indices. If a tensor is symmetric with respect to a portion of its indices, round brackets enclose only the indices concerned. The following equation shows how to make any rank-2 tensor symmetric,

$$a_{(ij)} = \frac{1}{p!}\left(a_{ij} + a_{ji}\right) \qquad (p = 2)\ . \tag{A.16}$$

Here, p is the number of indices that are being made symmetric. As a quick example, take the asymmetric tensor a_{ij} we dealt with previously.

$$a_{(ij)} = \frac{1}{2!}\left(\begin{pmatrix} 1 & 2 & 3 \\ 4 & 5 & 6 \\ 7 & 8 & 9 \end{pmatrix} + \begin{pmatrix} 1 & 4 & 7 \\ 2 & 5 & 8 \\ 3 & 6 & 9 \end{pmatrix} \right) = \begin{pmatrix} 1 & 3 & 5 \\ 3 & 5 & 7 \\ 5 & 7 & 9 \end{pmatrix} \qquad (p = 2)$$

We can even extend the method to any tensor of higher order,

$$a_{(ijk)} = \frac{1}{p!}\left(a_{ijk} + a_{ikj} + a_{jik} + a_{kji} + a_{jki} + a_{kij}\right) \qquad (p = 3)\ .$$

In almost the same manner, one can make a tensor skew-symmetric. Skew-symmetrisation is represented by square brackets [ ], and such that an interchange of any two indices gives a change in sign,

$$a_{[ij]} = \frac{1}{p!}\left(a_{ij} - a_{ji}\right) \qquad (p = 2)\ ,$$

$$a_{[ijk]} = \frac{1}{p!}\left(a_{ijk} - a_{ikj} - a_{jik} - a_{kji} + a_{jki} + a_{kij}\right) \qquad (p = 3)\ . \tag{A.17}$$

Finally, consider skew-symmetrising the tensor a_{ijk} for indices ij only (i.e., $a_{[ij]k}$), or indices ik only (i.e., $a_{[i|j|k]}$). Note the vertical bars (guards) which protect index j from the process, and that $p = 2$ for both cases. The same applies for the symmetrisation process, albeit with round brackets ( ) instead.

A.6 The Christoffel Symbol

The Christoffel symbols of the first and second kinds are defined as follows,

$$[ij, k] = \frac{1}{2}\left(\frac{\partial g_{ik}}{\partial x^j} + \frac{\partial g_{jk}}{\partial x^i} - \frac{\partial g_{ij}}{\partial x^k}\right), \tag{A.18}$$

$$\Gamma^l_{ij} = g^{lk}\,[ij, k] = \frac{1}{2} g^{lk}\left(\frac{\partial g_{ik}}{\partial x^j} + \frac{\partial g_{jk}}{\partial x^i} - \frac{\partial g_{ij}}{\partial x^k}\right). \tag{A.19}$$

Supposing the tensor g_{ij} is symmetric - interchanging the indices i and j

within Eq.(A.18) clearly has no effect upon the outcome. Thus, the Christoffel symbols are symmetric within indices i and j.

Checking the consistency of indexing, it also follows that the indices of $[ij, k]$ are considered as subscripts. Furthermore, we note that within Eq.(A.19), the index k is summed over for all values $1 \ldots n$. A derivation of Eq.(A.18) will be given later when discussing covariant derivatives.

A.7 Covariant Derivatives

The covariant derivative ∇_i gets its name from the fact that it possesses a single lower index, much like the partial derivative ∂_i. However, there is a slight difference. Whilst $\nabla_i \, g^{r_1 \ldots r_m}_{s_1 \ldots s_p}$ does transform as a tensor (giving a mixed tensor of rank $m + p + 1$), its partial equivalent $\partial_i \, g^{r_1 \ldots r_m}_{s_1 \ldots s_p}$ does not - except for the limiting case of a function (i.e., scalar quantity) which gives a covariant tensor of rank-1. Partial derivatives can be thought of generating a flat tangent space upon any curved surface, whereas covariant derivatives are slightly more difficult to envisage. It is convenient therefore to demonstrate covariant differentiation via means of a few examples:

$$\nabla_i \, f = \partial_i \, f \qquad \text{For a function / scalar} \tag{A.20}$$

$$\nabla_i \, \lambda^l = \partial_i \, \lambda^l + \Gamma^l_{ij} \, \lambda^j \qquad \text{For a } (1,0) \text{ tensor} \tag{A.21}$$

$$\nabla_i \, \lambda_l = \partial_i \, \lambda_l - \Gamma^j_{il} \, \lambda_j \qquad \text{For a } (0,1) \text{ tensor} \tag{A.22}$$

$$\nabla_i \, g^{lm} = \partial_i \, g^{lm} + \Gamma^l_{ij} \, g^{jm} + \Gamma^m_{ij} \, g^{lj} \qquad \text{For a } (2,0) \text{ tensor} \tag{A.23}$$

$$\nabla_i \, g_{lm} = \partial_i \, g_{lm} - \Gamma^j_{im} \, g_{lj} - \Gamma^j_{il} \, g_{jm} \qquad \text{For a } (0,2) \text{ tensor} \tag{A.24}$$

$$\nabla_i \, g^l_m = \partial_i \, g^l_m + \Gamma^l_{ij} \, g^j_m - \Gamma^j_{im} \, g^l_j \qquad \text{For a } (1,1) \text{ tensor} \tag{A.25}$$

Let us begin by considering the first term on the RHS of Eq.(A.20). It possesses the same indices as the LHS (as it should), the only difference being a partial derivative. Look through the rest of the equations, and observe that this statement holds true.

The next thing to observe is the number of Christoffel symbols which appear explicitly in each equation; for Rank-1 there is only one, for Rank-2 there are two and so forth. It is important to note that each Christoffel symbol is summed over, since a contraction is present.

Now observe in Eq.(A.21) that since a Christoffel symbol appears (which has three indices), one of these indices is required to contract with another (since there are only two indices on the LHS). The contraction is not within the Christoffel symbol itself, so the index of our tensor being acted upon must change. The new index in the tensor contracts with a lower index of the Christoffel symbol. The original index of the tensor becomes the upper index of the Christoffel symbol. Note also that within Eqs.(A.23-A.25), one index of the original rank-2 tensor is remains fixed; hence two Christoffel symbols.

The final observation (most evident from Eq.(A.25)), is that changing a contravariant index means a plus sign precedes the Christoffel symbol. Conversely, changing a covariant index means a minus sign precedes the Christoffel symbol.

Thus, one may draw up a quickfire guide to covariant differentiation:

- Step 1: The first term on the RHS will be the same as the LHS, just replace nabla ∇ with partial ∂ and use the same indices.
- Step 2: For the second term on the RHS, simply write the same tensor

you are trying to differentiate, but change one of the indices to another character. If you change an upper index in the original tensor, a plus sign will precede the new tensor. Conversely, use a minus sign if you change a lower index. Repeat this step until all indices have been changed. Note that only one index for each new tensor on the RHS should be different to the tensor on the LHS - all other indices remain unaffected.

- Step 3: Christoffel symbols are now required to precede to newly formed tensors on the RHS, and it is easy to know which indices the Christoffel symbols will possess. Each entity on the RHS must have the same indices as the LHS, and thus a contraction of indices will be present.

A.7.1 Metric Compatibility

A metric (a rank-2 covariant tensor) is said to be compatible if its covariant derivative is equal to zero; e.g. $\nabla_k \, g_{ij} = 0$. One may then use this relation to derive the Christoffel Symbol of Eq.(A.18).

$$
\begin{aligned}
&1) \qquad \nabla_k \, g_{ij} = \partial_k \, g_{ij} - \Gamma^l_{ik} \, g_{lj} - \Gamma^l_{jk} \, g_{il} = 0 \ , \\
&2) \qquad \nabla_j \, g_{ik} = \partial_j \, g_{ik} - \Gamma^l_{ij} \, g_{lk} - \Gamma^l_{jk} \, g_{il} = 0 \ , \\
&3) \qquad \nabla_i \, g_{jk} = \partial_i \, g_{jk} - \Gamma^l_{ij} \, g_{lk} - \Gamma^l_{ik} \, g_{jl} = 0 \ ,
\end{aligned}
$$

$$
2) \ + \ 3) \ - \ 1) \ = \ \partial_j \, g_{ik} + \partial_i \, g_{jk} - \partial_k \, g_{ij} - 2\Gamma^l_{ij} \, g_{lk} = 0 \ .
$$

Here, we have used the fact that Christoffel symbols and metrics are symmetric in their lower two indices (e.g., $\Gamma^l_{ik} \, g_{lj} = \Gamma^l_{ik} \, g_{jl}$). Thus, we have the following relation,

$$\Gamma^l_{ij}\, g_{lk} = \frac{1}{2}\left(\partial_j\, g_{ik} + \partial_i\, g_{jk} - \partial_k\, g_{ij}\right) = [ij,k] \ .$$

A.8 Derivation of the Riemann Tensor

Firstly, one must apply the commutator of two covariant derivatives $[\nabla_\mu, \nabla_\nu]$ to a contravariant vector V^ρ. This yields the following,

$$[\nabla_\mu, \nabla_\nu]\, V^\rho = \left(\nabla_\mu \nabla_\nu - \nabla_\nu \nabla_\mu\right) V^\rho = \underbrace{\nabla_\mu \nabla_\nu V^\rho}_{(1)} - \underbrace{\nabla_\nu \nabla_\mu V^\rho}_{(2)}$$

$$1) \qquad \nabla_\mu\left(\nabla_\nu V^\rho\right) = \partial_\mu \underbrace{\left(\nabla_\nu V^\rho\right)}_{a} - \Gamma^\lambda_{\mu\nu} \underbrace{\nabla_\lambda V^\rho}_{b} + \Gamma^\rho_{\mu\sigma} \underbrace{\nabla_\nu V^\sigma}_{c}$$

$$= \partial_\mu \underbrace{\left(\partial_\nu V^\rho + \Gamma^\rho_{\nu\sigma} V^\sigma\right)}_{a} - \Gamma^\lambda_{\mu\nu} \underbrace{\left(\partial_\lambda V^\rho + \Gamma^\rho_{\lambda\sigma} V^\sigma\right)}_{b} + \Gamma^\rho_{\mu\sigma} \underbrace{\left(\partial_\nu V^\sigma + \Gamma^\sigma_{\nu\lambda} V^\lambda\right)}_{c}$$

$$2) \qquad \nabla_\nu\left(\nabla_\mu V^\rho\right) = \partial_\nu \nabla_\mu V^\rho - \Gamma^\lambda_{\nu\mu} \nabla_\lambda V^\rho + \Gamma^\rho_{\nu\sigma} \nabla_\mu V^\sigma$$

$$= \partial_\nu\left(\partial_\mu V^\rho + \Gamma^\rho_{\mu\sigma} V^\sigma\right) - \Gamma^\lambda_{\nu\mu}\left(\partial_\lambda V^\rho + \Gamma^\rho_{\lambda\sigma} V^\sigma\right) + \Gamma^\rho_{\nu\sigma}\left(\partial_\mu V^\sigma + \Gamma^\sigma_{\mu\lambda} V^\lambda\right)$$

Subtracting 2) from 1) gives $[\nabla_\mu, \nabla_\nu]\, V^\rho \ =$

$$\underbrace{\partial_\mu \partial_\nu V^\rho}_{d} + \left(\partial_\mu \Gamma^\rho_{\nu\sigma}\right) V^\sigma + \underbrace{\Gamma^\rho_{\nu\sigma}\left(\partial_\mu V^\sigma\right)}_{e} - \Gamma^\lambda_{\mu\nu}\left(\partial_\lambda V^\rho\right) - \underbrace{\Gamma^\lambda_{\mu\nu}\Gamma^\rho_{\lambda\sigma} V^\sigma}_{*} + \underbrace{\Gamma^\rho_{\mu\sigma}\left(\partial_\nu V^\sigma\right)}_{f} + \underbrace{\Gamma^\rho_{\mu\sigma}\Gamma^\sigma_{\nu\lambda} V^\lambda}_{*} -$$

$$\underbrace{\partial_\nu \partial_\mu V^\rho}_{d} - \left(\partial_\nu \Gamma^\rho_{\mu\sigma}\right) V^\sigma - \underbrace{\Gamma^\rho_{\mu\sigma}\left(\partial_\nu V^\sigma\right)}_{f} + \Gamma^\lambda_{\nu\mu}\left(\partial_\lambda V^\rho\right) + \underbrace{\Gamma^\lambda_{\nu\mu}\Gamma^\rho_{\lambda\sigma} V^\sigma}_{*} - \underbrace{\Gamma^\rho_{\nu\sigma}\left(\partial_\mu V^\sigma\right)}_{e} - \underbrace{\Gamma^\rho_{\nu\sigma}\Gamma^\sigma_{\mu\lambda} V^\lambda}_{*}$$

The terms labelled d, e, f all cancel with one another. For terms labelled

with an asterix*, we interchange the indices λ and σ. This is a perfectly reasonable step since they are dummy indices, and how we label them is unimportant. We now have the following,

$$\begin{aligned}[\nabla_\mu, \nabla_\nu] V^\rho &= \left(\partial_\mu \Gamma^\rho_{\nu\sigma}\right) V^\sigma - \Gamma^\lambda_{\mu\nu} \left(\partial_\lambda V^\rho\right) - \Gamma^\sigma_{\mu\nu}\Gamma^\rho_{\sigma\lambda} V^\lambda + \Gamma^\rho_{\mu\lambda}\Gamma^\lambda_{\nu\sigma} V^\sigma \\ \ldots &- \left(\partial_\nu \Gamma^\rho_{\mu\sigma}\right) V^\sigma + \Gamma^\lambda_{\nu\mu} \left(\partial_\lambda V^\rho\right) + \Gamma^\sigma_{\nu\mu}\Gamma^\rho_{\sigma\lambda} V^\lambda - \Gamma^\rho_{\nu\lambda}\Gamma^\lambda_{\mu\sigma} V^\sigma\end{aligned}$$

$$= \left(\partial_\mu \Gamma^\rho_{\nu\sigma} - \partial_\nu \Gamma^\rho_{\mu\sigma} + \Gamma^\rho_{\mu\lambda}\Gamma^\lambda_{\nu\sigma} - \Gamma^\rho_{\nu\lambda}\Gamma^\lambda_{\mu\sigma}\right) V^\sigma - \left(\Gamma^\lambda_{\mu\nu}\partial_\lambda - \Gamma^\lambda_{\nu\mu}\partial_\lambda\right) V^\rho - \left(\Gamma^\sigma_{\mu\nu}\Gamma^\rho_{\sigma\lambda} - \Gamma^\sigma_{\nu\mu}\Gamma^\rho_{\sigma\lambda}\right) V^\lambda$$

$$= \left(\partial_\mu \Gamma^\rho_{\nu\sigma} - \partial_\nu \Gamma^\rho_{\mu\sigma} + \Gamma^\rho_{\mu\lambda}\Gamma^\lambda_{\nu\sigma} - \Gamma^\rho_{\nu\lambda}\Gamma^\lambda_{\mu\sigma}\right) V^\sigma - 2\Gamma^\lambda_{[\mu\nu]} \nabla_\lambda V^\rho$$

and thus, $$[\nabla_\mu, \nabla_\nu] V^\rho = R^\rho_{\sigma\mu\nu} V^\sigma - 2\Gamma^\lambda_{[\mu\nu]} \nabla_\lambda V^\rho$$

$$R^\rho_{\sigma\mu\nu} = \partial_\mu \Gamma^\rho_{\nu\sigma} - \partial_\nu \Gamma^\rho_{\mu\sigma} + \Gamma^\rho_{\mu\lambda}\Gamma^\lambda_{\nu\sigma} - \Gamma^\rho_{\nu\lambda}\Gamma^\lambda_{\mu\sigma} \tag{A.26}$$

where $R^\rho_{\sigma\mu\nu}$ is the Riemannian Curvature Tensor. The final term $2\Gamma^\lambda_{[\mu\nu]}\nabla_\lambda V^\rho$ is called the Torsion tensor, and incorporates the anti-symmetrisation of a Christoffel Symbol. However, since the Christoffel symbols are symmetric, this is therefore equal to zero.

It is imperative to note that there are two definitions of the Riemann tensor, and whichever one decides to use will determine subsequent formulae. All textbooks have their own conventions and definitions, and some fail to mention the distinction altogether. The issue arises later when one considers the Ricci tensor $R_{\sigma\mu}$. This rank-2 covariant tensor arises due to a contraction of two indices within the Riemann tensor - but which exactly? This depends entirely upon how one defines the Riemann tensor! As a brief summary, both definitions of the Riemann tensor are given below, and the contractions

required to obtain the valid Ricci tensor.

Convention #1 (adopted throughout this thesis):

$$R^{\rho}_{\sigma\mu\nu} = \partial_\mu \Gamma^{\rho}_{\nu\sigma} - \partial_\nu \Gamma^{\rho}_{\mu\sigma} + \Gamma^{\rho}_{\mu\lambda}\Gamma^{\lambda}_{\nu\sigma} - \Gamma^{\rho}_{\nu\lambda}\Gamma^{\lambda}_{\mu\sigma}$$

$$R_{\sigma\mu} = R^{\rho}_{\sigma\mu\rho} = \partial_\mu \Gamma^{\rho}_{\rho\sigma} - \partial_\rho \Gamma^{\rho}_{\mu\sigma} + \Gamma^{\rho}_{\mu\lambda}\Gamma^{\lambda}_{\rho\sigma} - \Gamma^{\rho}_{\rho\lambda}\Gamma^{\lambda}_{\mu\sigma}$$

Convention #2:

$$\tilde{R}^{\rho}_{\sigma\mu\nu} = \partial_\nu \Gamma^{\rho}_{\sigma\mu} - \partial_\mu \Gamma^{\rho}_{\sigma\nu} + \Gamma^{\rho}_{\nu\lambda}\Gamma^{\lambda}_{\sigma\mu} - \Gamma^{\rho}_{\mu\lambda}\Gamma^{\lambda}_{\nu\sigma}$$

$$\tilde{R}_{\sigma\nu} = \tilde{R}^{\rho}_{\sigma\rho\nu} = \partial_\nu \Gamma^{\rho}_{\sigma\rho} - \partial_\rho \Gamma^{\rho}_{\sigma\nu} + \Gamma^{\rho}_{\nu\lambda}\Gamma^{\lambda}_{\sigma\rho} - \Gamma^{\rho}_{\rho\lambda}\Gamma^{\lambda}_{\nu\sigma}$$

Note that for the second convention, one instead contracts with the middle index of the Riemann tensor.

A.9 Einstein Field Equations

In this final section, I wish to conclude with a derivation of the Einstein field equations. Numerous textbooks each have their own explicit form of these equations, commonly differing by a minus sign. However, seldom do they include a derivation, or any motivation for this rogue change of sign. As a starting point, we consider the Einstein-Hilbert action, with both matter and electromagnetic fields for a D-dimensional space-time,

$$S = \int d^D x \, \frac{\sqrt{|g|}}{2\,\kappa} \left[\mathcal{R} + 2\Lambda + \frac{1}{4} F_{\alpha\beta} F^{\alpha\beta} + \kappa \left[g^{\mu\nu} \partial_\mu \varphi \, \partial_\nu \varphi - 2V(|\varphi|) \right] \right] .$$

Here, we have Ricci scalar $\mathcal{R} = R_{\sigma\mu}\, g^{\sigma\mu}$, metric determinant $g = \det(\mathrm{g}^{\sigma\mu})$, cosmological constant Λ, EM fields given by $F_{\mu\nu} = \partial_\mu A_\nu - \partial_\nu A_\mu$ where A_μ is the usual vector potential, gravitational coupling constant $\kappa = 8\pi G$ and a scalar field φ. Expanding out this action gives,

$$= \int d^D x \left(\frac{\sqrt{|g|}}{2\,\kappa}\, g^{\mu\nu} R_{\mu\nu} + \frac{\sqrt{|g|}}{\kappa}\,\Lambda - \frac{\sqrt{|g|}}{8\,\kappa}\, F_{\beta\alpha} F^{\alpha\beta} + \frac{\sqrt{|g|}}{2}\, g^{\mu\nu} \partial_\mu\varphi\, \partial_\nu\varphi - \sqrt{|g|}\, V(|\varphi|) \right)$$

Note that we have flipped the indices of $F_{\alpha\beta} = -F_{\beta\alpha}$, for later convenience. We shall also rewrite the contravariant term as $F^{\alpha\beta} = g^{\alpha\gamma} F_{\gamma\delta} g^{\delta\beta}$.

$$\begin{aligned} \delta S = \int d^D x \,(\, & \frac{\mathcal{R}\,\delta\sqrt{|g|}}{2\,\kappa} + \frac{\sqrt{|g|}}{2\,\kappa}\, R_{\mu\nu}\,\delta g^{\mu\nu} + \frac{\Lambda\,\delta\sqrt{|g|}}{\kappa} - \frac{\delta\sqrt{|g|}}{8\,\kappa}\, F_{\beta\alpha} g^{\alpha\gamma} F_{\gamma\delta} g^{\delta\beta} \\ \ldots\; & - \frac{\sqrt{|g|}}{8\,\kappa}\, F_{\beta\alpha} \delta g^{\alpha\gamma} F_{\gamma\delta} g^{\delta\beta} - \frac{\sqrt{|g|}}{8\,\kappa}\, F_{\beta\alpha} g^{\alpha\gamma} F_{\gamma\delta} \delta g^{\delta\beta} + \frac{\delta\sqrt{|g|}}{2}\, g^{\mu\nu} \partial_\mu\varphi\, \partial_\nu\varphi \\ & \ldots + \frac{\sqrt{|g|}}{2}\, \partial_\mu\varphi\, \partial_\nu\varphi\, \delta g^{\mu\nu} - \delta\sqrt{|g|}\, V(|\varphi|)\,) \end{aligned}$$

Now we use the following relation,

$$\delta(g^{-1}) = \frac{1}{g}\, g_{\mu\nu}\, \delta g^{\mu\nu}$$

$$\begin{aligned} \delta(\sqrt{g}) = \delta((g^{-1})^{-1/2}) &= -\frac{1}{2}\,(g^{-1})^{-3/2}\,\delta(g^{-1}) \\ &= -\frac{1}{2}\,\sqrt{g}\, g_{\mu\nu}\,\delta g^{\mu\nu} \end{aligned}$$

This now gives us the following,

$$\delta S = \int d^D x \,(\, -\frac{\mathcal{R}}{4\,\kappa}\,\sqrt{|g|}\, g_{\mu\nu}\,\delta g^{\mu\nu} + \frac{\sqrt{|g|}}{2\,\kappa}\, R_{\mu\nu}\,\delta g^{\mu\nu} - \frac{\Lambda}{2\,\kappa}\,\sqrt{|g|}\, g_{\mu\nu}\,\delta g^{\mu\nu} \;\ldots$$

$$\ldots - \frac{\sqrt{|g|}}{16\,\kappa}\, g_{\mu\nu}\delta g^{\mu\nu} F_{\beta\alpha} g^{\alpha\gamma} F_{\gamma\delta} g^{\delta\beta} - \frac{\sqrt{|g|}}{8\,\kappa}\, F_{\beta\mu}\delta g^{\mu\nu} F_{\nu\delta} g^{\delta\beta} - \frac{\sqrt{|g|}}{8\,\kappa}\, F_{\nu\alpha} g^{\alpha\gamma} F_{\gamma\mu}\delta g^{\mu\nu}$$

$$\ldots - \frac{\sqrt{|g|}}{4}\,(g^{\alpha\beta}\partial_\alpha\varphi\,\partial_\beta\varphi)\, g_{\mu\nu}\,\delta g^{\mu\nu} + \frac{\sqrt{|g|}}{2}\,\partial_\mu\varphi\,\partial_\nu\varphi\,\delta g^{\mu\nu} + \frac{\sqrt{|g|}}{2}\, g_{\mu\nu}\,\delta g^{\mu\nu}\, V(|\varphi|)\ )$$

where we have performed several changes of index to avoid confusion. The labelling of indices which contract with one another is unimportant - we merely carry out this process to simplify the equations further.

$$\delta S = \int d^D x\ (\ \frac{\sqrt{|g|}}{2\,\kappa}\,[\, R_{\mu\nu} - \frac{1}{2}\,\mathcal{R}\, g_{\mu\nu} - \Lambda g_{\mu\nu}$$
$$\ldots\ - \frac{1}{8}\, g_{\mu\nu} F_{\beta\alpha} g^{\alpha\gamma} F_{\gamma\delta} g^{\delta\beta} - \frac{1}{4}\, F_{\beta\mu} F_{\nu\delta} g^{\delta\beta} - \frac{1}{4}\, F_{\nu\alpha} g^{\alpha\gamma} F_{\gamma\mu}$$
$$\ldots\ + \kappa\,\partial_\mu\varphi\,\partial_\nu\varphi - \frac{\kappa}{2}\, g_{\mu\nu} g^{\alpha\beta}\,\partial_\alpha\varphi\,\partial_\beta\varphi + \kappa\, g_{\mu\nu}\, V(|\varphi|)]\,\delta g^{\mu\nu}\ )$$

remembering to take careful note of the positions of round ( ) and square [ ] brackets. We again flip the indices of $F_{\beta\mu} = -F_{\mu\beta}$, and represent the covariant term in mixed form as $F_{\nu\delta} g^{\delta\beta} = F_\nu^\beta$. Likewise, $F_{\nu\alpha} g^{\alpha\gamma} = F_\nu^\gamma$. We then have,

$$\delta S = \int d^D x\ (\ \frac{\sqrt{|g|}}{2\,\kappa}\,[\, R_{\mu\nu} - \frac{1}{2}\,\mathcal{R}\, g_{\mu\nu} - \Lambda g_{\mu\nu} - \frac{1}{8}\, g_{\mu\nu} F_{\beta\alpha} g^{\alpha\gamma} F_{\gamma\delta} g^{\delta\beta}$$
$$\ldots\ + \frac{1}{2} F_{\mu\beta} F_\nu^\beta + \kappa\,(\partial_\mu\varphi\,\partial_\nu\varphi - g_{\mu\nu}\,(\frac{1}{2}\, g^{\alpha\beta}\partial_\alpha\varphi\,\partial_\beta\varphi - V(|\varphi|)))]\,\delta g^{\mu\nu}\ )$$

Now we simply take $\delta S\,/\,\delta g^{\mu\nu} = 0$, thus giving,

$$R_{\mu\nu} - \frac{1}{2}\, g_{\mu\nu}\,\mathcal{R} - \Lambda\, g_{\mu\nu} = -\kappa\,[\,\frac{1}{2\,\kappa} F_{\mu\beta} F_\nu^\beta - \frac{1}{8\,\kappa}\, g_{\mu\nu} F_{\beta\alpha} g^{\alpha\gamma} F_{\gamma\delta} g^{\delta\beta}\ \ \ldots$$

$$\ldots + \partial_\mu\varphi\,\partial_\nu\varphi - g_{\mu\nu}\,(\frac{1}{2}\,g^{\mu\nu}\partial_\mu\varphi\,\partial_\nu\varphi - V(|\varphi|))] \ .$$

One clearly notes the existence of a minus sign on the RHS of this equation. Most textbooks choose to omit this, although this depends entirely upon how one defines their action S. One may further simplify the equation as,

$$G_{\mu\nu} - \Lambda\, g_{\mu\nu} = -\kappa\, T_{\mu\nu},$$

where $G_{\mu\nu}$ and $T_{\mu\nu}$ are the Einstein and energy-momentum tensors respectively.

$$G_{\mu\nu} = R_{\mu\nu} - \frac{1}{2}\,g_{\mu\nu}\,\mathcal{R}$$

$$T_{\mu\nu} = \frac{1}{2\,\kappa}F_{\mu\beta}F^{\beta}_{\nu} - \frac{1}{8\,\kappa}\,g_{\mu\nu}F_{\beta\alpha}g^{\alpha\gamma}F_{\gamma\delta}g^{\delta\beta} + \partial_\mu\varphi\,\partial_\nu\varphi - g_{\mu\nu}\,\left(\frac{1}{2}\,g^{\mu\nu}\partial_\mu\varphi\,\partial_\nu\varphi - V(|\varphi|)\right)$$

Appendix B

Mathematica Code

In this section, I have included code required for intermediary calculations. Individual subsections will be referenced in the main body of the text.

B.1 Section 2.2.1

B.1.1 Figure 2.2

We first begin with the simplest case of observer 3, who travels with uniform motion at a velocity $v_x = \sqrt{0.4999}c$. For all calculations, one normalises the speed of light 'c' to unity. We may thus write a simple code as follows,

```
In[1]:=vx=Sqrt[0.4999];
In[2]:=NIntegrate[Sqrt[1-(vx^2)],{t,0,8*Pi}]
Out[2]=17.7733
```

This gives the proper time for τ_3, as recorded by observer 3. The time t_3 as recorded by observer 1 is merely the integration range of our affine parameter λ (i.e., $8\pi = 25.1327$).

We next calculate the proper time τ_2 for observer 2. The code is again given as follows,

```
In[1]:=vx=Sqrt[0.4999];
In[2]:=NIntegrate[Sqrt[1-(vx^2)*(1+Cos[vx*t]^2)],{t,0,8*Pi}]
Out[2]=11.4844
```

For observer 4, the integration limits are different to those of the previous two observers. This is because observer 1 measures a longer period from an outside perspective. To calculate this period, one must use the simple formula $s = at^2/2$ and re-arrange for time t. The acceleration a is given by differentiating the velocity component v_x with respect to the affine parameter λ. The distance x travelled is calculated from the previous two observers as $x = \sqrt{0.4999}*8\pi$. Thus, one obtains and integration period of $t = 16\pi/\sqrt{2} = 35.5431$, which is the time t_4 as recorded by observer 1. The code is then as follows,

```
In[1]:=vx=Sqrt[0.4999];
In[2]:=NIntegrate[Sqrt[1-(vx*t/(8*Pi))^2],{t,0,16*Pi/Sqrt[2]}]
Out[2]=27.9182
```

B.1.2 Figure 2.3

We now consider circular motion in both the Minkowski and Schwarzschild space-times. Observer 2 is positioned at a radius $R = 2$ from the centre of orbit. For simplicity, we choose polar coordinates for intermediary calculations. The integration limits are the elapsed time as recorded by observer 1. This is given as the orbital circumference, divided by the tangential speed. A simple code is then given as follows,

```
In[1]:="define orbital radius";
In[2]:=R=2;
In[3]:="define angular velocity (e.g., with tangential component
        equal to a quarter the speed of light)";
In[4]:=vang=0.25/R;
In[5]:=NIntegrate[Sqrt[1-(vang^2)*(R^2)],{t,0,16*Pi}]
Out[5]=48.6693
```

The R^2 term inside the integration arises due to theta-theta metric component. We perform exactly the same calculation for $R = 3$ (note the change of integration limits).

```
In[1]:=R=3;
In[2]:=vang=0.25/R;
In[3]:=NIntegrate[Sqrt[1-(vang^2)*(R^2)],{t,0,24*Pi}]
Out[3]=73.0040
```

We now carry out the same calculations in Schwarzschild space-time.

```
In[1]:="define the Schwarzschild radius rs";
In[2]:=rs=1;
In[3]:="define the time-time metric component f(R)";
In[4]:=f[R_]=1-rs/R;
In[5]:=R=2;
In[6]:=vang=0.25/R;
In[7]:=NIntegrate[Sqrt[f[R]-(vang^2)*(R^2)],{t,0,16*Pi}]
Out[7]=33.2475
```

We then perform the same calculation for $R = 3$,

```
In[1]:=rs=1;
In[2]:=f[R_]=1-rs/R;
In[3]:=R=3;
In[4]:=vang=0.25/R;
In[5]:=NIntegrate[Sqrt[f[R]-(vang^2)*(R^2)],{t,0,24*Pi}]
Out[5]=58.6057
```

The final calculation for an observer passing by a large gravitational object, is particularly difficult. For convenience, we transfer to the pseudo-Cartesian coordinate system. We shall integrate between the limits $-3 \leq \mathrm{y} \leq 3$, and thus $-3/\ \mathrm{vy} \leq t \leq 3/\ \mathrm{vy}$. For $\mathrm{vy} = 0.25$, an observer positioned at infinity would thus measure an elapsed time of $t = 6/\ \mathrm{vy} = 24.0000$.

```
In[1]:=rs=1;
In[2]:=x=3;
In[3]:=z=0;
In[4]:=vy=0.25;
In[5]:=y=vy*t;
In[6]:=R=Sqrt[(x^2)+(y^2)+(z^2)];
In[7]:=f[R_]=1-rs/R;
In[8]:=NIntegrate[Sqrt[f[R]-((vy^2)/(R^2))*((x^2)+((y^2)/f[R])
       +(z^2))],{t,-3/vy,3/vy}]
Out[8]=19.1762
```

B.2 Section 6.3

In this section, all intermediary calculations concerning holographic methods are provided. We first begin by considering the full gravitational model in $D+1$ dimensions. Since I cannot use Greek symbols inside the verbatim

environment, I shall make the following adjustments: holographic dimension $\chi = z$, scalar potential $\phi(\chi) = At(z)$, and scalar field $\psi(\chi) = P(z)$.

```
In[1]:=Clear[All]
In[2]:="specify the number of dimensions";
In[3]:=n=4;
In[4]:="specify the coordinate system";
In[5]:=coord={t,z,x,y};
In[6]:="specify the components of the vector potential";
In[7]:=A={f(z)*((L^2)/(z^2))*At(z),0,0,0};
In[8]:="specify the ansatz for the metric (i.e., asymptotically AdS)";
In[9]:=metric={{f(z)*(L^2)/(z^2),0,0,0},{0,-(1/f(z))*((L^2)/(z^2)),0,0},
      {0,0,-(L^2)/(z^2),0},{0,0,0,-(L^2)/(z^2)}};
In[10]:=inversemetric=Simplify[Inverse[metric]];
In[11]:="our first key result is finding the determinant of the metric";
In[12]:=Det[metric]
Out[12]=-(L^8)/(z^8)
In[13]:="now calculate the Christoffel symbols";
In[14]:=affine:=affine=Simplify[Table[(1/2)*Sum[(inversemetric[[i,s]])
       *(D[metric[[s,j]],coord[[k]]]+D[metric[[s,k]],coord[[j]]]
       -D[metric[[j,k]],coord[[s]]]),{s,1,n}],{i,1,n},{j,1,n},{k,1,n}]]
In[15]:=listaffine:=Table[If[UnsameQ[affine[[i,j,k]],0],{ToString[
       Gamma[i,j,k]],affine[[i,j,k]]}],{i,1,n},{j,1,n},{k,1,n}]
In[16]:=TableForm[Partition[DeleteCases[Flatten[listaffine],Null],2],
       TableSpacing->{2,2}]
In[17]:="now calculate the Riemann tensor";
In[18]:=riemann:=riemann=Simplify[Table[D[affine[[i,j,k]],coord[[l]]]
       -D[affine[[i,j,l]],coord[[k]]]+Sum[affine[[s,j,k]]
```

```
        *affine[[i,s,l]]-affine[[s,j,l]]*affine[[i,s,k]],{s,1,n}],
        {i,1,n},{j,1,n},{k,1,n},{l,1,n}]]
In[19]:=listriemann:=Table[If[UnsameQ[riemann[[i,j,k,l]],0],{ToString[
        R[i,j,k,l]],riemann[[i,j,k,l]]}],{i,1,n},{j,1,n},{k,1,n},
        {l,1,n}]
In[20]:=TableForm[Partition[DeleteCases[Flatten[listriemann],Null],2],
        TableSpacing->{2,2}]
In[21]:="now calculate the Ricci tensor and scalar";
In[22]:=ricci:=ricci=Simplify[Table[Sum[riemann[[i,j,i,l]],{i,1,n}],
        {j,1,n},{l,1,n}]]
In[23]:=listricci:=Table[If[UnsameQ[ricci[[j,l]],0],{ToString[R[j,l]],
        ricci[[j,l]]}],{j,1,n},{l,1,n}]
In[24]:=TableForm[Partition[DeleteCases[Flatten[listricci],Null],2],
        TableSpacing->{2,2}]
In[25]:=scalar=Simplify[Sum[inversemetric[[i,j]]*ricci[[i,j]],{i,1,n}
        ,{j,1,n}]]
In[26]:="in order to have empty space, we require scalar=-12/(L^2)";
In[27]:=DSolve[scalar==-12/(L^2),f(z),z]
Out[27]={{f(z)->1+(z^3)C[1]+(z^4)C[2]}}
In[28]:="for the case of the AdS Schwarzschild black hole, we consider
         C[1]=-1/(z0^3) and C[2]=0";
```

This function $f(z)$ is reflected in Eq.(6.3). The beauty of using a conformal field theory is that we can discard of the L^2/z^2 prefactor in the metric components of `In[9]`, by either absorbing this into either our coordinate system or choice of function f. We consider a new function $g(z)$, and re-run the program with this function in-situ (cf. Section 6.3).

```
In[1]:=Clear[All]
```

```
In[2]:="specify the number of dimensions";
In[3]:=n=4;
In[4]:="specify the coordinate system";
In[5]:=coord={t,z,x,y};
In[6]:=g(z_)=1-((z^3)/(z0^3));
In[7]:="specify the components of the vector potential";
In[8]:=A={g(z)*At(z),0,0,0};
In[9]:="specify the ansatz for the metric (i.e., asymptotically AdS)";
In[10]:=metric={{g(z),0,0,0},{0,-(1/g(z)),0,0},
       {0,0,-1,0},{0,0,0,-1}};
In[11]:=inversemetric=Simplify[Inverse[metric]];
In[12]:="our first key result is finding the determinant of the metric";
In[13]:=Det[metric]
Out[13]=-1
In[14]:="now calculate the Christoffel symbols";
In[15]:=affine:=affine=Simplify[Table[(1/2)*Sum[(inversemetric[[i,s]])
        *(D[metric[[s,j]],coord[[k]]]+D[metric[[s,k]],coord[[j]]]
        -D[metric[[j,k]],coord[[s]]]),{s,1,n}],{i,1,n},{j,1,n},{k,1,n}]]
In[16]:=listaffine:=Table[If[UnsameQ[affine[[i,j,k]],0],{ToString[
        Gamma[i,j,k]],affine[[i,j,k]]}],{i,1,n},{j,1,n},{k,1,n}]
In[17]:=TableForm[Partition[DeleteCases[Flatten[listaffine],Null],2],
        TableSpacing->{2,2}]
In[18]:="now calculate the Riemann tensor";
In[19]:=riemann:=riemann=Simplify[Table[D[affine[[i,j,k]],coord[[l]]]
        -D[affine[[i,j,l]],coord[[k]]]+Sum[affine[[s,j,k]]
        *affine[[i,s,l]]-affine[[s,j,l]]*affine[[i,s,k]],{s,1,n}],
        {i,1,n},{j,1,n},{k,1,n},{l,1,n}]]
```

```
In[20]:=listriemann:=Table[If[UnsameQ[riemann[[i,j,k,l]],0],{ToString[
        R[i,j,k,l]],riemann[[i,j,k,l]]}],{i,1,n},{j,1,n},{k,1,n},
        {l,1,n}]
In[21]:=TableForm[Partition[DeleteCases[Flatten[listriemann],Null],2],
        TableSpacing->{2,2}]
In[22]:="now calculate the Ricci tensor and scalar";
In[23]:=ricci:=ricci=Simplify[Table[Sum[riemann[[i,j,i,l]],{i,1,n}],
        {j,1,n},{l,1,n}]]
In[24]:=listricci:=Table[If[UnsameQ[ricci[[j,l]],0],{ToString[R[j,l]],
        ricci[[j,l]]}],{j,1,n},{l,1,n}]
In[25]:=TableForm[Partition[DeleteCases[Flatten[listricci],Null],2],
        TableSpacing->{2,2}]
In[26]:=scalar=Simplify[Sum[inversemetric[[i,j]]*ricci[[i,j]],{i,1,n}
        ,{j,1,n}]]
Out[26]=-g''[z]
In[27]:="we now calculate the electromagnetic term F=dA";
In[28]:=FullSimplify[Sum[inversemetric[[i,l]]*inversemetric[[j,k]]
        *(D[A[[k]],coord[[l]]]-D[A[[l]],coord[[k]]])*(D[A[[j]],
        coord[[i]]]-D[A[[i]],coord[[j]]]),{i,1,n},{j,1,n},{k,1,n},
        {l,1,n}]
Out[28]=-2*((At[z]*g'[z]+g[z]*At'[z])^2)
In[29]:=FullSimplify[Sum[inversemetric[[i,j]]*D[P[z],coord[[j]]]
        *D[P[z],coord[[i]]]-I*q*A[[i]]*P[z]*inversemetric[[i,j]]
        *D[P[z],coord[[j]]]+I*q*A[[j]]*P[z]*inversemetric[[i,j]]
        *D[P[z],coord[[i]]]+(q^2)*A[[i]]*A[[j]]*inversemetric[[i,j]]
        *(P[z]^2),{i,1,n},{j,1,n}]]
Out[29]=g[z]*((q^2)*(At[z]^2)*(P[z]^2)-(P'[z]^2))
```

B.2.1 Figure 6.1

The next stage is to calculate the action functional $S[\psi, \phi]$. We take all the necessary parameters from the previous lines of code, and substitute them into our action (6.1), and thus giving Eq.(6.4).

```
In[1]:=g[z_]=*(z^2)/(L^2))*1-((z^3)/(z0^3)));
In[2]:="we reparametrise both m and q to be dimensionally consistent";
In[3]:=q=Q/L;
In[4]:=m=M/L;
In[5]:="we consider asymptotic solutions as outlined in the main text";
In[6]:=P[z_]=(1/(q*Sqrt[k]))*(I+P3*(z^3)/(L^3));
In[7]:=Pc[z_]=(1/(q*Sqrt[k]))*(-I+P3*(z^3)/(L^3));
In[8]:=At[z_]=At0+At3*((z^3)/(L^3));
In[9]:=m=0;
In[10]:="substitute everything into the action functional";
In[11]:=action=FullSimplify[(1/(2*k))*(-g''[z]-(1/2)*((At[z]*g'[z]
       +g[z]*At'[z])^2)+k*(g[z]*((q^2)*(At[z]^2)*(P[z]^2)-(P'[z]^2))
       -2*(m^2)*(P[z]^2)))];
In[12]:="integrate the action functional over the holographic
         dimension";
In[13]:=function=Integrate[action,{z,0,z0}];
In[14]:=eq1=D[function,P3];
In[15]:=eq2=D[function,At3];
In[16]:=Solve[{eq1==0,eq2==0},{P3,At3}];
In[17]:=L=1;
In[18]:=k=1;
In[19]:=At0=1;
In[20]:="for the next line of code, one must copy a solution for P3
```

```
        from Out[14]. This will plot P3 for differing of horizon
        radius z0";
In[21]:=Animate[Plot[{P3,At3},{z0,0,20},PlotRange->{0,0.1}],{Q,0,3}]
```

Appendix C

Publication #1

Introduction to Graphene Electronics – A New Era of Digital Transistors and Devices

K.C. Yung

Department of Industrial systems and Engineering,

The Hong Kong Polytechnic University,

Hung Hom, Kowloon, Hong Kong.

W.M. Wu, M.P. Pierpoint and F.V. Kusmartsev

Department of Physics, Loughborough University,

Loughborough, LE11 3TU, United Kingdom.

Abstract

The speed of silicon-based transistors has reached an impasse in the recent decade, primarily due to scaling techniques and the short-channel effect. Conversely, graphene (a revolutionary new material possessing an atomic thickness) has been shown to exhibit a promising value for electrical con-

ductivity. Graphene would thus appear to alleviate some of the drawbacks associated with silicon-based transistors. It is for this reason why such a material is considered one of the most prominent candidates to replace silicon within nano-scale transistors. The major crux here, is that graphene is intrinsically gapless, and yet, transistors require a band-gap pertaining to a well-defined ON/OFF logical state. Therefore, exactly as to how one would create this band-gap in graphene allotropes is an intensive area of growing research. Existing methods include nano-ribbons, bilayer and multilayer structures, carbon nanotubes, as well as the usage of the graphene substrates. Graphene transistors can generally be classified according to two working principles. The first is that a single graphene layer, nanoribbon or carbon nanotube can act as a transistor channel, with current being transported along the horizontal axis. The second mechanism is regarded as tunneling, whether this be band-to-band on a single graphene layer, or vertically between adjacent graphene layers. The high-frequency graphene amplifier is another talking point in recent research, since it does not require a clear ON/OFF state, as with logical electronics. This paper reviews both the physical properties and manufacturing methodologies of graphene, as well as graphene-based electronic devices, transistors, and high-frequency amplifiers from past to present studies. Finally, we provide possible perspectives with regards to future developments.

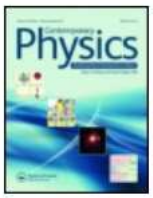

Contemporary Physics
Publication details, including instructions for authors and subscription information:
http://www.tandfonline.com/loi/tcph20

Introduction to graphene electronics - a new era of digital transistors and devices

K.C. Yung[a], W.M. Wu[ab], M.P. Pierpoint[b] & F.V. Kusmartsev[b]
[a] Department of Industrial and Systems Engineering, The Hong Kong Polytechnic University, Hung Hom, Kowloon, Hong Kong, China.
[b] Department of Physics, Loughborough University, Loughborough LE11 3TU, UK.
Published online: 01 Nov 2013.

To cite this article: K.C. Yung, W.M. Wu, M.P. Pierpoint & F.V. Kusmartsev , Contemporary Physics (2013): Introduction to graphene electronics - a new era of digital transistors and devices, Contemporary Physics, DOI: 10.1080/00107514.2013.833701

To link to this article: http://dx.doi.org/10.1080/00107514.2013.833701

Appendix D

Publication #2

Application of Graphene within Optoelectronic Devices and Transistors

F.V. Kusmartsev, W.M. Wu and M.P. Pierpoint
Department of Physics, Loughborough University,
Loughborough, LE11 3TU, United Kingdom.

K.C. Yung
Department of Industrial systems and Engineering,
The Hong Kong Polytechnic University,
Hung Hom, Kowloon, Hong Kong.

Abstract

Scientists are always yearning for new and exciting ways to unlock graphene's true potential. However, recent reports suggest this two-dimensional material may harbor some unique properties, making it a viable candidate for use in optoelectronic and semiconducting devices. Whereas on one hand,

graphene is highly transparent due to its atomic thickness, the material does exhibit a strong interaction with photons. This has clear advantages over existing materials used in photonic devices such as Indium-based compounds. Moreover, the material can be used to 'trap' light and alter the incident wavelength, forming the basis of the plasmonic devices. We also highlight upon graphene's nonlinear optical response to an applied electric field, and the phenomenon of saturable absorption. Within the context of logical devices, graphene has no discernible band-gap. Therefore, generating one will be of utmost importance. Amongst many others, some existing methods to open this band-gap include chemical doping, deformation of the honeycomb structure, or the use of carbon nanotubes (CNTs). We shall also discuss various designs of transistors, including those which incorporate CNTs, and others which exploit the idea of quantum tunneling. A key advantage of the CNT transistor is that ballistic transport occurs throughout the CNT channel, with short channel effects being minimized. We shall also discuss recent developments of the graphene tunneling transistor, with emphasis being placed upon its operational mechanism. Finally, we provide perspective for incorporating graphene within high frequency devices, which do not require a pre-defined band-gap.

D.1 Introduction

Two-dimensional materials have always been considered unstable due to their thermal fluctuations [64, 65], in what were famously referred to as the Landau-Peierls arguments. However, many scientists have not given up hope that such two-dimensional structures exist. In 2004, a research team based in Manchester successfully segregated graphene flakes from a graphite sample

via 'mechanical exfoliation' (more commonly referred to as the scotch-tape method) [64, 66, 67, 68, 69]. They witnessed a full preservation of graphene's hexagonal honeycomb structure, with astounding electrical, thermal and optical characteristics.

Graphene is an allotrope of carbon - other examples include diamond, fullerene and charcoal, all with their own unique properties. Usually graphene will be found in the form of highly ordered pyrolytic graphite (HOPG), whereby individual graphene layers stack on top of one another to form a crystalline lattice. Its stability is due to a tightly packed, periodic array of carbon atoms [70] (cf. Figure D.1), and an sp^2 orbital hybridization - a combination of orbitals p_x and p_y that constitute the σ-bond. The final p_z electron makes up the π-bond, and is key to the half-filled band which permits free-moving electrons [71]. In total, graphene has three σ-bonds and one π-bond. The right-hand portion of Figure D.1, emphasizes how small displacements of the sub-lattices A and B can be shifted in the z-direction [72].

Moreover, graphene's mode of preparation will have a strong influence upon its overall quality and characteristics. As conducted by Geim et al. [10], mechanical exfoliation consists of gradually stripping more and more layers from a graphite sheet, until what remains are a few layers of graphene. In terms of overall mobility and the absence of structural defects, this method will produce the highest quality material. Other methods such as vacuum epitaxial growth or chemical vapour deposition (CVD), each have their own merits, but will generally lead to inferior quality. For a more in-depth discussion of the available manufacturing methods, one can refer to [64, 74, 75, 76, 77, 78, 79, 80, 81, 82, 83, 84].

On the other hand, graphene is highly impermeable [70] - the mobility

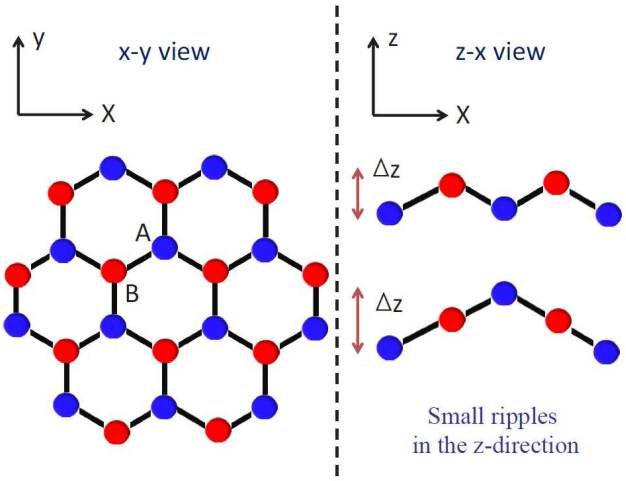

Figure D.1: The honeycomb structure of graphene is presented in the left-hand figure. The right-hand figure depicts small quantum corrugations of the sub-lattices A and B, which are shifted in the transverse direction by a small fraction of the inter-atomic spacing 'a'.

can become severely compromised upon molecular attachment. Yet, this apparent flaw has immediate applications for molecular sensors. By monitoring the deviation of electrical resistivity [85, 86], one could, for example, envision novel smoke detection systems. So too is graphene more than 100 times stronger than steel [70], possessing a Young's modulus as large as 1TPa [87]. Together with its outstanding electrical [71], thermal [88, 89, 90] and in particular, optical properties [74, 87, 91, 92], graphene has thus become a widely sought after material for use in future semiconducting and optoelectronic devices [75, 93].

Electrical Mobility - As a material, graphene harbors some remarkable qualities; highly elastic due to its monolayer structure, and more conductive than copper with mobilities reaching up to $200,000 \mathrm{cm}^{-2}\mathrm{V}^{-1}\mathrm{s}^{-1}$ for perfect

structures [87, 94, 95]. Charge carriers in graphene travel with a Fermi velocity $v_F = \sqrt{3}\gamma_0 a/2\hbar \approx 10^6 \mathrm{ms}^{-1}$. Here, $\gamma_0 \approx 3$ eV is the energy required to 'hop' from one carbon atom to the nearest neighbor, $a \approx 1.42$Å is the interatomic spacing between two neighboring carbon atoms, and $\hbar$ is Planck's constant [71, 87, 96]. This Fermi velocity is approximately 1/300 the speed of light, thus presenting a miniaturized platform upon which to test many features of quantum electrodynamics (QED) [64]. Theoretical studies with graphene show that the density of states (DoS) of electrons approaches zero at the Dirac point. However, a minimum conductivity $\sigma_0 \approx 4e^2/h$ has been displayed [64], which is approximately double that for the conductance quantum [97, 98]. Even at room temperature, electrons can undergo long range transport with minimal scattering [64, 95, 99].

Thermal Conductivity - Heat flow in suspended graphene was recently shown to be mediated by ballistic phonons, and has been verified by Pumarol et al [88] with the use of high resolution vacuum scanning thermal microscopy. However, when considering multiple layers of graphene, this transport will be reduced due to an increase of inelastic scattering. The same is observed for graphene coated upon a substrate - the mean free path of thermal phonons degrading to less than 100 nm. Nevertheless, graphene on a silicon substrate can still retain a thermal conductivity of around $600\,\mathrm{Wm}^{-1}\mathrm{K}^{-1}$ [89] - even higher than copper. Whilst the mechanism of heat transport across the graphene-substrate interface remains unknown [100], it is possible this may be linked to the in-plane thermal conductivity [88, 90].

Optical Response - Graphene's atomic thickness makes it almost perfectly transparent to visible light [72, 101], allowing such a material to become

widely accessible to a number of applications. These cover everything from photovoltaic cells, to graphene photonic transistors [93, 96, 102, 103]. Being a single layer of carbon atoms, graphene also exhibits many interesting photonic properties. As such, our focus will be directed mainly upon those which are associated with applications to optoelectronic devices. The transmittance between multiple graphene layers, how optical frequency relates to conductivity, nonlinear optical response, saturable absorption and plasmonics will all be discussed in later sections.

Most semiconducting photonic devices will be governed in some way by electron excitation and electron-hole recombination. Excitation refers to an electron absorbing photon energy of a very specific wavelength within the allowed energy bands. On the other hand, recombination is a process which leads to the emission of photons (cf. electro-luminescence) [101]. Gallium arsenide (GaAs), indium functional compounds and silicon are all common semiconductors for use in photonic devices [104, 105]. However, graphene exhibits a strong interaction with photons, with the potential for direct band-gap creation and thus being a good candidate for optoelectronic and nanophotonic devices [106]. Its strong interaction with light arises due to the Van Hove singularity [107]. Graphene also possesses different time scales in response to photon interaction, ranging from femtoseconds (ultra-fast) to picoseconds [106, 108]. Overall, graphene could easily be an ideal candidate for transparent films, touch screens and light emitting cells. It may even be used as a plasmonic device which confines light, and altering the incident wavelength. We shall elaborate upon this in later sections.

D.2 Energy Spectrum, Band-Gap and Quantum Effects

Theoretical studies of monolayer graphite (i.e., graphene) first began in 1947 by Wallace [71], who considered a simple tight-binding model with a single hopping integral. This model takes into account the hopping of an electron from one carbon atom to its first and second nearest neighbors only. Wallace's conclusions were stark; an electrical conductivity should theoretically exist for two-dimensional graphene. To elaborate; at six positions of the Brillouin zone, Dirac points (K and K') exist. These are points in momentum space for which the energy $E(\mathrm{p}_0) = 0$, where $\mathrm{p}_0 = \hbar\mathbf{K}$ (or $\hbar\mathbf{K}$'). Here, we have denoted the momentum as a vector $\mathbf{p} = (\mathrm{p_x}, \mathrm{p_y}) = \hbar\mathbf{k}$, where $\mathbf{k} = (\mathrm{k_x}, \mathrm{k_y})$ is the wave vector [64]. The energy eigenvalues were found to take a gapless form [71],

$$E^{\pm}(\mathrm{k_x}, \mathrm{k_y}) = \pm\gamma_0\sqrt{1 + 4\cos\frac{\sqrt{3}\mathrm{k_x a}}{2}\cos\frac{\mathrm{k_y a}}{2} + 4\cos^2\frac{\mathrm{k_y a}}{2}} \tag{D.1}$$

where the plus and minus signs refer to the upper and lower half-filled bands respectively [87, 97]. By expanding the above equation in the vicinity of the K or K' points, one can thus obtain a linear dispersion relation that is given by $E^{\pm} = \pm v_F\hbar|\delta\mathbf{k}|$, where $\mathbf{k} = \mathbf{K}+\delta\mathbf{k}$. These constitute what are known as Dirac cones, and are clearly emphasized by Figure D.2. Here, a direct contact of the conduction and valence bands is found [68, 71, 73, 74], thus pertaining to a zero energy band-gap E_g [64, 71, 75]. Therefore, generating a band-gap in graphene will be essential for its application within semiconducting devices (e.g., transistors). On the other hand, graphene may secure its place

in high-frequency devices, which do not require a logical OFF state [101].

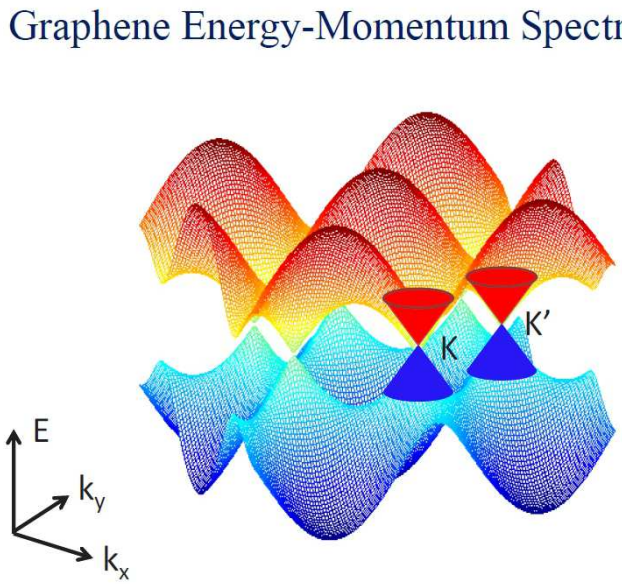

Figure D.2: The energy-dispersion spectrum as given by Eq.(D.1). Here, the z-axis represents the energy $E(\mathbf{k})$, with the $x-y$ plane corresponding to the momentum $\mathbf{k}$=$(\mathrm{k_x}, \mathrm{k_y})$. Dirac cones are located at both the K and K' points of the Brillouin zone.

A. Dirac Energy-Momentum Dispersion

Supposing we consider the Hamiltonian $\hat{H}$ as given by Wallace [71] - in the low energy limit, spinless carriers in graphene possess a zero effective mass, and are well approximated by the relativistic Dirac Hamiltonian $\hat{H}$ [97],

$$\hat{H} = v_F \hbar \hat{\sigma} \dot{\delta} \mathbf{k} \tag{D.2}$$

where $\hat{\sigma}\dot{\delta}\mathbf{k} = \sigma_x \delta \mathrm{k_x} + \sigma_\mathrm{y} \delta \mathrm{k_y}$. Here, $\hat{\sigma} = (\sigma_x, \sigma_y)$ is the vector of 2×2 Pauli

matrices:

$$\sigma_x = \begin{pmatrix} 0 & 1 \\ 1 & 0 \end{pmatrix} \qquad \sigma_y = \begin{pmatrix} 0 & -i \\ i & 0 \end{pmatrix} \tag{D.3}$$

The spinor wave function ψ of graphene can be obtained from,

$$\hat{H}\psi = E\psi \tag{D.4}$$

where E denotes the energy eigenvalues of $\hat{H}$ [87]. Here, $\psi = (\psi_A, \psi_B)^{\mathrm{T}}$ is a vector containing the two component wave function. These components represent the sub-lattices A and B accordingly [97].

B. Band-Gap Creation

Generally speaking, the electrical conductivity of a material can fall into one of three groups: conductors, insulators, semiconductors [109, 110, 111]. For a conductor, electrons are able to move freely in the conduction band since electron states are not fully occupied. However, the conduction and valence band may sometimes be separated by an energy band-gap E_g (e.g., for insulators and semiconductors), thus preventing the free movement of electrons in the conduction band. For an insulator, an electron requires a huge energy in order to excite from the valence to conduction band. A small band-gap is present for semiconductors, with an electronic band structure that is parabolic in shape [75, 94]. Doped semiconductors will make the band-gap even smaller, and hence more easy to control (cf. Figure D.3).

Graphene's high mobility makes it a particularly enticing material for use in electronic devices. However, we have already mentioned that in the vicin-

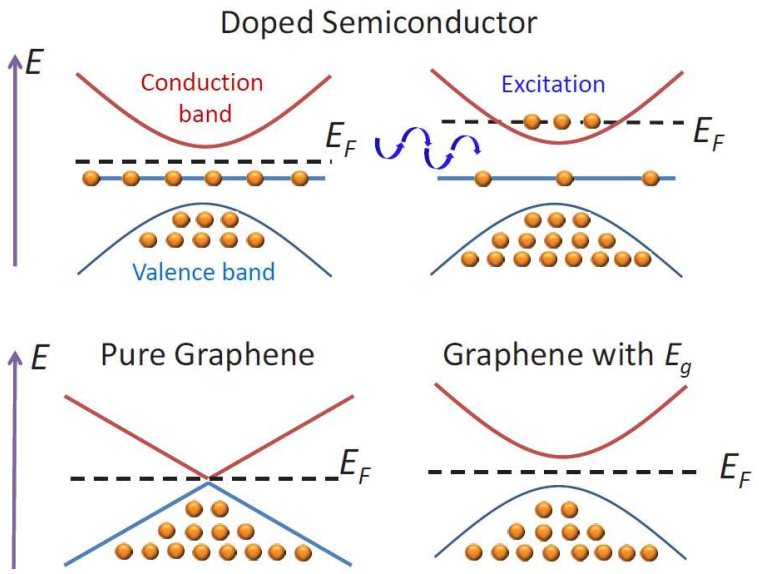

Figure D.3: The upper half of this figure depicts the electronic band structure of a doped semiconductor. Typically, the band-gap for a doped semiconductor is very small, with only a small energy being required to excite an electron from the valence to conduction band. The lower figure shows the electronic band structure for graphene. For pure samples, no energy band-gap E_g exists. In principle, an energy band-gap can be created via many methods.

ity of the Dirac point, graphene possesses a conical band structure which is gapless (i.e., $E_g = 0$) [64, 73]. Thus our main concern with regards to logical devices, is the absence of this well-defined OFF state pertaining to zero current flow. To rectify this, we must open up an energy band-gap such that $E_g \neq 0$. With regards to optoelectronic devices, a tunable band-gap can specify the range of wavelengths which can be absorbed. The energy bands for pure graphene, and graphene with a small band-gap E_g are displayed in Figure D.3. The Fermi energy level E_F is situated at the Dirac point for

pure graphene [66]. For graphene that has been modified to include a band-gap, an energy is required to excite electrons from the valence to conduction band, and hence an ON/OFF state regime is established [73]. Amongst many others, existing methods include the use of carbon nanotubes (CNTs), graphene nanoribbons (GNRs) or even bilayer graphene [64, 94, 101, 112]. However, it is important to note that although bilayer graphene does possess a zero energy band-gap, an applied electric field can be used to create one [72, 75, 94]. Other methods include deformed structures, graphene oxide (GO) [75, 85, 86], and also the use of chemical doping via compounds such as Boron Nitride (BN) [113, 114]. The idea here, is that the doped atoms alter graphene's honeycomb structure, similar to deformation or localized defects [115, 116]. All in all, one has to note that the aforementioned methods are not well-developed enough to maintain a high mobility. Much more exotic concepts are required, which we shall now discuss.

C. Quantum Phenomena

Of its more surprising attributes, graphene has also displayed signs of anomalous quantum behaviors, even at room temperature [68, 117]. We shall briefly discuss two key phenomena in particular.

Quantum Hall Effect: QHE has been observed for both single and bilayer graphene [74, 118, 119], in the presence of a magnetic field B. The Landau levels for graphene are given by,

$$E_{Landau} = \sqrt{|2e\hbar v_F^2 \mathrm{Bj}|} \tag{D.5}$$

where e is the electric charge, and $j \in \mathbb{Z}$ is the Landau index [68, 117]. In conventional 2-D semiconductors, the Landau levels are $E = \hbar\omega_c(j + 1/2)$, where ω_c is the cyclotron frequency [68, 117]. The anomalous energy spectrum for graphene subject to a B field leads to a one half shift of the minimum conductivity at the zero energy Landau level, whereas traditional QHE semiconductors give an integer one [68, 117]. The Hall conductivity σ_H is therefore given by [87, 97],

$$\sigma_H = g\left(j + \frac{1}{2}\right)\frac{e^2}{h} \tag{D.6}$$

where g is the degeneracy. For graphene, a fourfold degeneracy exists - two spins, and the valley degeneracy of the K and K' Dirac points [68]. Additionally, the fractional QHE has been observed for both monolayer and bilayer graphene (cf. for details [68, 118, 119]).

Klein Tunneling: Intuition states that if a particle's kinetic energy KE is less than some value U, then it will be physically incapable of surpassing a potential barrier of the same energy U. However, quantum mechanics states that a particle is able to tunnel the potential barrier U with a certain decay probability [68]. Furthermore, relativistic quantum mechanics permits a remarkable phenomenon called Klein tunneling. Much like a freight train instead taking a tunnel from one side of a mountain to the other, an electron can perform a similar process [117, 120]. This occurs when an electron experiences a strong repulsive force from the barrier U, and hence induces a hole inside the barrier [68, 118, 119]. This leads to a matching of the energy spectrum inside and outside the barrier, with the transmission probability becoming very close to one [117]. A perfect transmission is demonstrated for

square potentials only, and is dependent upon the energy KE, and the angle of incidence θ relative to the barrier [121]. Confined bound states will arise for energies close to the Dirac point [121]. Further details regarding how this confinement effect may relate to the special waveguide geometry has been discussed in references [122, 123, 124, 125, 126].

D.3 Photonic Properties

Optical communication networks are ubiquitous nowadays, affecting our everyday lives. A fiber-optic cable provides a much wider bandwidth, and less energy loss than some traditional copper wiring [104, 105]. According to the Shannon-Hartley theorem [127], the maximum capacity of a channel is given by

$$max(C) = Blog_2(1 + \frac{P_s}{P_n}), \tag{D.7}$$

where B is the channel bandwidth, and P_s and P_n are the average signal and noise powers respectively. It is therefore obvious that optical cable provides a much larger channel capacity, where $P_s/P_n \gg 1$.

When optical and electronic devices work together (e.g., a modulator), light signals are converted into an electrical equivalent. Generally speaking, the term 'optoelectronic' refers to an optical (photonic) electronic device, which transmits signals via light waves, or electron-photon interaction [104, 105]. A photonic device can be made of semiconductors, either being integrated into electronic circuits or transistors. Optoelectronics also play an important role as the mediator of optical communication. Devices will typically operate with an optical frequency ranging from ultraviolet to infrared

(400–700 nm) [104, 105], although graphene photonic devices can possess an even wider spectrum than this [128].

A. Transmittance Properties

As emphasized by Figure D.4, a single layer of graphene absorbs a mere 2.3% of incident light, allowing around 97.7% to pass through. Wavelengths typically range from the infrared to ultraviolet regions [96]. The transmittance T of single-layer graphene (SLG) can be approximated by the following Talyor expansion [96, 102, 103, 129, 130]

$$T = \frac{1}{(1+\alpha\pi/2)^2} \approx 1 - \alpha\pi \approx 97.7\% \ , \tag{D.8}$$

where $\alpha = e^2/c\hbar \approx 1/137$ is the fine structure constant. For multiple layers of graphene, this can be roughly estimated by

$$T \approx (1 - N\alpha\pi) \ , \tag{D.9}$$

where N is number of layers (cf. Bao *et al.* [102]). For example, the transmittance of bilayer graphene ($N = 2$) is around 95.4% (cf. Figure D.4). Indium Tin Oxide (ITO) is a semiconductor which is typically used in photonic devices, with a transmittance of around 80% [96]. It is therefore obvious that graphene film has a clear advantage over ITO. Bonaccorso *et al.* [96] also point out that the resistance per unit area for ITO is much smaller than for graphene. However, this value can be minimized by increasing the concentration of charge carriers via methods such as doping.

The degree of reflection from SLG is almost negligible, just less than 0.1%

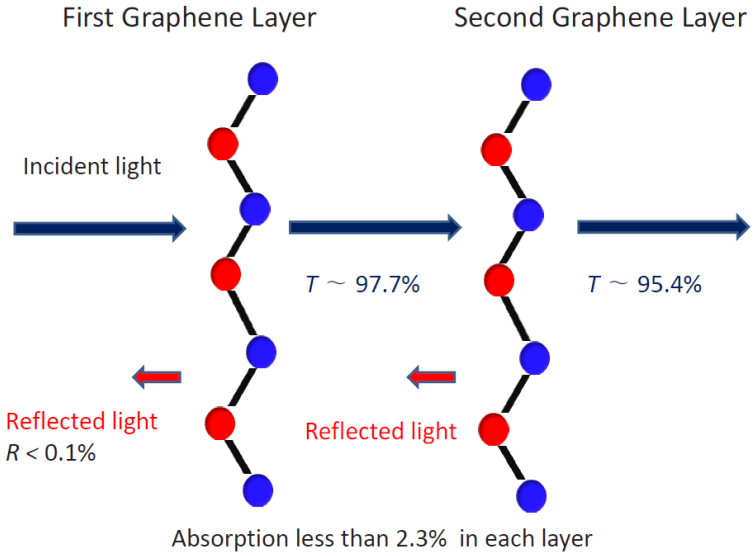

Figure D.4: Incident light passes through the to layers of graphene. The transmission, absorption and reflection coefficients are all shown. Each layer of graphene only absorbs 2.3% of incident light, transmitting around 97.7%, and reflecting less than 0.1%.

[96]. Avouris *et al.* [103, 129, 130] also mention that graphene shows a strong interaction of photons, much stronger than some traditional photonic materials per unit depth. It is also surprising that absorption can rise from 2.3% to around 40% with high concentration doping [103, 129, 130]. Unquestionably, these properties present graphene as an excellent candidate for use in photonic applications.

B. Optical Conductivity

As mentioned by Avouris *et al.* [103, 129, 130], graphene possesses a universal optical conductance $G_{op} = e^2/4\hbar$. In general, the optical conductivity

σ_{op} depends upon the frequency ω, Fermi energy E_F (via chemical doping or an applied gate voltage), and the transition rate Γ. Moreover, the optical conductivity can be divided into real and imaginary components, $\Re(\sigma_{op})$ and $\Im(\sigma_{op})$ [96, 102, 103, 129, 130],

$$\sigma_{op}(\omega, E_F, \Gamma) = \Re(\sigma_{op}) + i\Im(\sigma_{op}) \tag{D.10}$$

with energy loss originating from the imaginary part [103, 129, 130].

Bao *et al.* [102] further explain that the interband and intraband carriers' transitions are the major factors governing the optical conductivity σ_{op} (cf. Figure D.5). Interband transitions refer to an exchange of charge carriers between the conduction and valence bands, whereas intraband transitions refer to a 'jump' between quantized energy levels. For carriers performing an interband transition (at high frequency), the energy of a photon $\hbar\omega$ should be satisfying the relationship $\hbar\omega \geq 2E_F$ [102]. For the low frequency THz range ($\hbar\omega < 2E_F$), the intraband transition would be a significant contribution to the optical conductivity, while interband transitions are prohibited in this range due to the Pauli exclusion principle (Pauli block) [130]. It is important to note that a change in doping concentration would alter the Fermi energy E_F , and hence the optical conductivity. Bao *et al.* [102] state that one can tune the optical conductivity by controlling the chemical doping (shift of E_F) and the frequency response. However, one must remain aware that a high doping concentration may deteriorate the transmittance T of graphene itself.

C. Linear and Nonlinear Optical Response

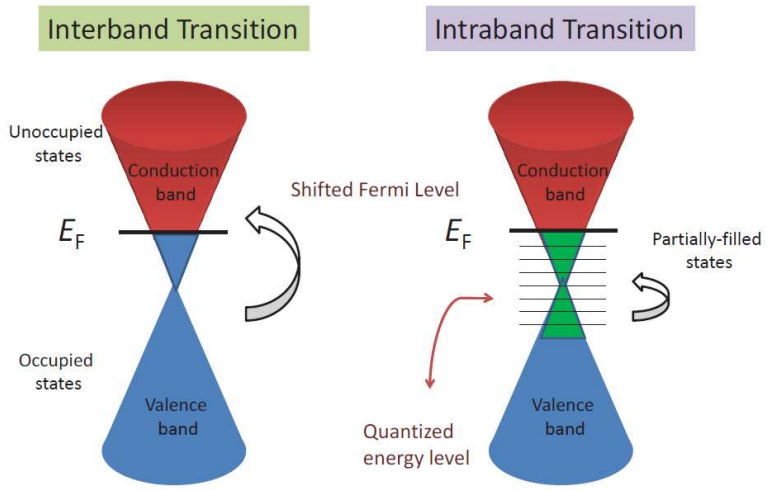

Figure D.5: The Fermi energy level E_F can be shifted upward due to either chemical doping or an applied electric field. Interband transitions refer to an electron 'jumping' from the valence to conduction bands, satisfying the relationship $\hbar\omega \geq 2E_F$. Intraband transitions refer to an electron moving through quantized energy levels, and requires less energy ($\hbar\omega < 2E_F$), provided the states are not already occupied.

Graphene also exhibits a strong nonlinear optical response to an electric field, and is an important factor in modifying the shape of the wavefront for incident light [103, 129, 130]. The displacement field D_z is given by the dielectric response of an applied electric field E_z along the 'z' direction, with polarization $\mathrm{P}(\mathrm{E}_z)$ (cf. Figure D.6);

$$\mathrm{D_z} = \epsilon_0\epsilon_\mathrm{r}\mathrm{E_z} = \epsilon_0\mathrm{E_z} + \mathrm{P(E_z)} \ . \tag{D.11}$$

Here, ϵ_0 is the electric permittivity of free space, and ϵ_r is the relative per-

mittivity. The polarization response can be written in terms of a power series (cf. for details [102, 131])

$$\mathrm{P}(\mathrm{E_z}) = \mathrm{C}_0 + \epsilon_0 \sum_{\mathrm{j}=1}^{\infty} \chi_{\mathrm{j}} (\mathrm{E_z})^{\mathrm{j}} \ , \tag{D.12}$$

where C_0 is a constant associated with the hysteresis (typically $C_0 = 0$), χ_j refers to the dielectric susceptibility of the j-th order correction, and $(\mathrm{Ez})^{\mathrm{j}}$ is the j-th power of $\mathrm{E_z}$. The linear dielectric susceptibility χ_1 can again be divided into a real part χ_{R1} and an imaginary part χ_{I1} [102]. The relative dielectric constant can then be expressed in terms of $\epsilon_r = \chi_{R1} + 1$, with an optical refractive index n_{op} given by,

$$n_{op} \approx \sqrt{\epsilon_r} = \sqrt{\chi_{R1} + 1} \ . \tag{D.13}$$

Thus, the refractive index is determined by the real part of the linear susceptibility χ_{R1}, as mentioned by Bao et al. [102]. Meanwhile, the imaginary part of the linear susceptibility χ_{I1} corresponds to the tangent loss arising at optical frequencies. Bao et al. [102] also come to the conclusion that the second order susceptibility χ_2 is generally small, provided that the symmetry of the graphene honeycomb structure is not broken (i.e., flat). The major contribution to the nonlinear response of graphene originates via the third order term $\epsilon_0 \chi_3 \mathrm{E}_z^3$, which modifies the current density in graphene (cf. for details [102]).

D. Surface Plasmons

Surface plasmons describe a set of quantized charge oscillations of electrons

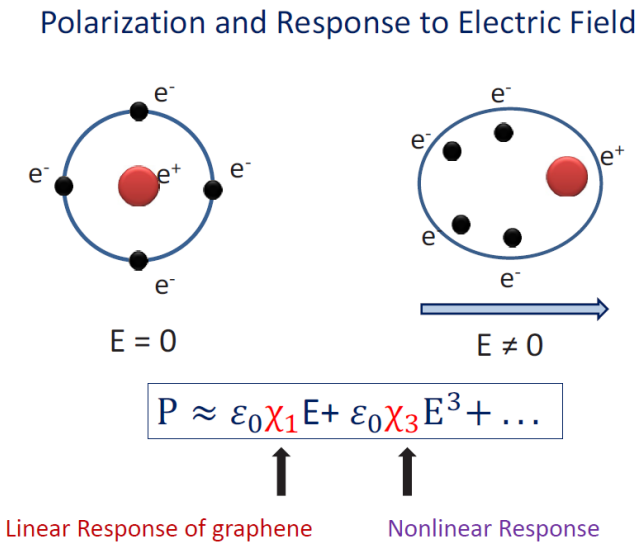

Figure D.6: This figure shows the linear and nonlinear responses to an electric field E. The lefthand figure schematically represents an atom without electric field, whilst the right-hand figure has a non-zero electric field. The equation is related to the polarization response P. The linear susceptibility χ_1 is usually associated with the refractive index, whereas the nonlinear susceptibility χ_3 provides a unique contribution to the optical properties of graphene. Due to the symmetry of graphenes honeycomb structure, the χ_2 component is very small, and is therefore neglected here.

and holes, acting upon the graphene-substrate interface [102] (cf. Figure D.7). Plasmons, in general, interact with photons or phonons to form the surface plasmon polariton (SPP). At present, aluminium, silver and gold are all ideal materials for plasmonic platforms [102, 93, 129, 130]. The basic idea is as follows - a dielectric material can be coated upon a graphene layer. Electrons then oscillate on the graphene-substrate interface, excited by the phonon or photon interactions of electromagnetic (EM) fields [102].

The SPP wavelength λ_{SPP} is normally suppressed, and much smaller than the incident wavelength λ_{in} - the ratio of these wavelengths typically being around $\lambda_{in}/\lambda_{SPP} \approx 10 - 100$ [102, 103, 129, 130]. The plasmonic frequency ω_{SPP} on the graphene surface is proportional to the square root of the Fermi energy, as given by [96, 102, 103]

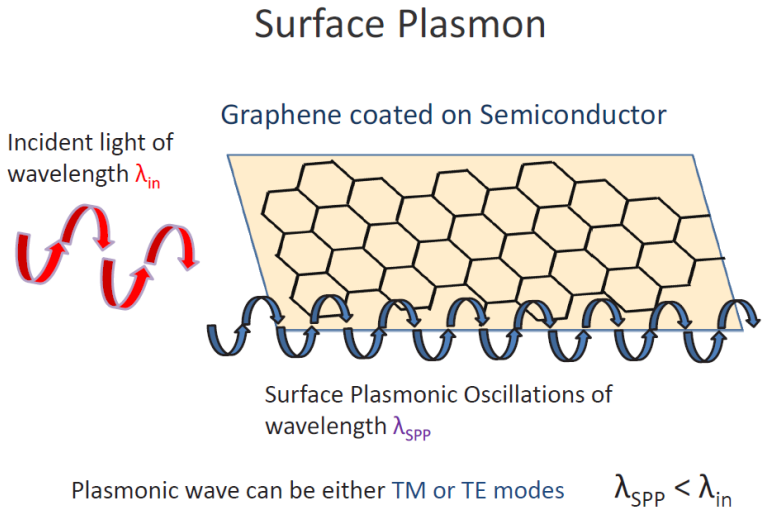

Figure D.7: This figure shows the surface plasmonic wave for graphene coated on a semiconductor. Plasmonic waves are trapped, and oscillate along the graphene and semiconductor interface. Typically, the surface plasmonic wavelength λ_{SPP} will be suppressed, and is much smaller than the incident wave λ_{in}. Either TM or TE wave modes can propagate along the plasmonic surface, depending upon the imaginary component of the optical conductivity.

$$\omega_{SPP} \propto \sqrt{E_F} \propto n^{\frac{1}{4}} \ , \tag{D.14}$$

where n is a carrier density. In practice, graphene can trap incident light, and an EM wave can propagate along the graphene surface in the THz to infrared range [103, 129, 130]. As mentioned by Avouris et al. [103, 129, 130], the distance traveled for a plasmonic wave in graphene is around $d_{SPP} \approx 10 - 100\lambda_{SPP}$. Graphene is thus a suitable material for a waveguide. Bao et al. [102] further remark that graphene is suitable for guiding transverse magnetic (TM) waves when the imaginary part of the optical conductivity $\Im(\sigma_{op}) > 0$, and suitable for guiding transverse electric (TE) waves when $\Im(\sigma_{op}) < 0$.

E. Saturable Absorption and Optical Excitation

There is an interesting property which prevents graphene from absorbing photons at high intensity, and can be used to adjust the wavefront of the light [103, 129, 130]. This is referred to as 'saturable absorption', and is dependent upon the wavelength and incident light intensity. This will be elaborated upon in later sections when we discuss the saturable absorber and photonic (optical) limiter.

The timescale of graphene's response to the interaction of photons, phonons and electron-hole recombination can be divided into three regimes [96, 102, 103, 129, 130] (cf. Figure D.8). Graphene has a very quick response to incident photons, around 10-100 fs, whereby 'hot' electrons are excited from the valence to conduction band [96, 102]. This also links to an excitation of the non-equilibrium state. Electrons may then cool down via the intraband phonon emission, with timescales of 0.1 ps [103, 129, 130]. Finally, an electron-hole pair may recombine, thus emitting photons, and an equilibrium state being reached. This process takes a mere 1-10 ps. It is important to note

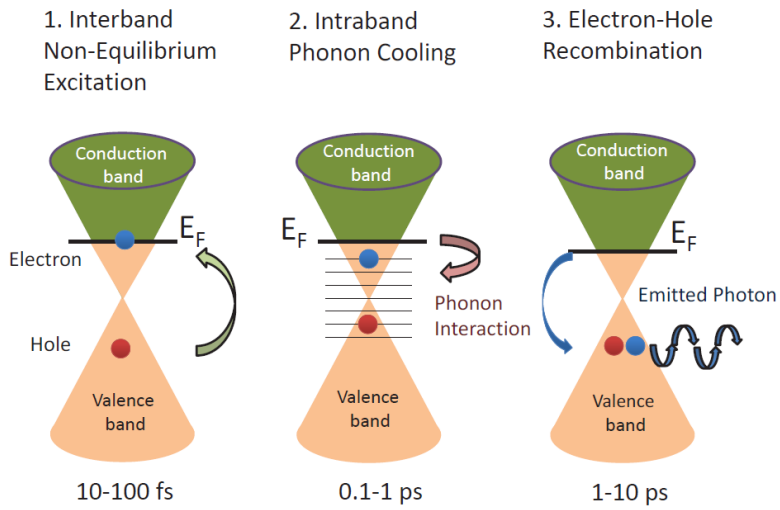

Figure D.8: There are three time scales associated with optical response. The left-hand figure represents the interband non-equilibrium excitation, and lasts around 10-100 fs. The middle figure relates to phonon cooling via the intraband interaction (0.1-1 ps). Finally, the right-hand figure is the process of electron-hole recombination (1-10 ps).

that these excitations and scattering processes are influenced by both topological defects of the lattices (e.g., dislocation and disclination) and boundary characteristics [103, 129, 130].

F. Graphene Photonic Crystal

The photonic crystal is a kind of optical device, whereby a lattice can be periodically allocated upon or within a semiconductor [132, 133] (cf. Figure D.9). A band-gap can be obtained in these periodic structures, and only a certain range of photon energies (i.e., frequencies) are allowed to propagate

within. The basic idea is that the periodic dielectric behaves as a superlattice, with restriction being placed upon the wave properties of the electrons [133]. Moktadir et al. [134] find that the graphene photonic crystal provides a wide transmission range, which can be tuned via an applied gate voltage. It has also been reported by Majumdar et al. [134] that the resonance reflectivity can be increased fourfold via a slight 2 nm shifting of the graphene crystalline structure (i.e. dislocations). Graphene's flexible nature therefore offers numerous applications.

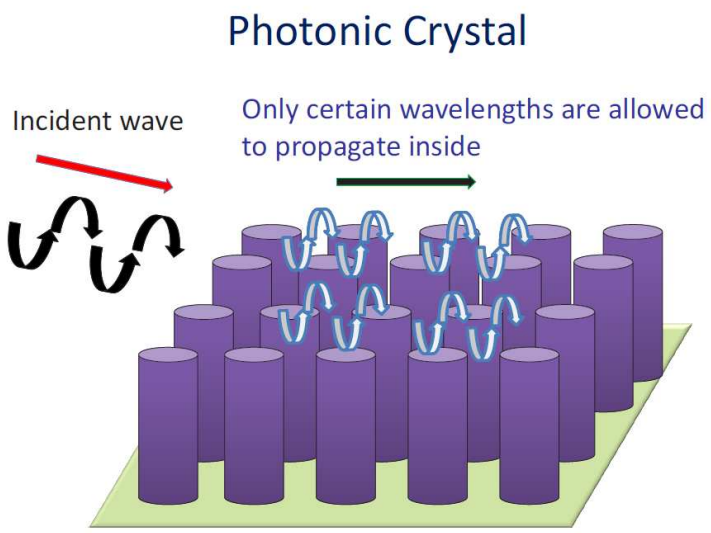

Figure D.9: Here, we present a periodic photonic crystal lattice on the substrate. The lattice forms a band-gap, allowing only certain wavelengths to propagate inside. The photonic properties can therefore be controlled.

D.4 Graphene Optoelectronic Devices

In this section, we will present ideas for optical devices which incorporate graphene, with emphasis being placed upon their photonic properties. The

various photodetectors, optical modulator, and the photonic limiter (mode-locked laser) will all be discussed.

A. Photodiode and Graphene Photodetector

The n-p or p-n junctions are comprised of two different semiconductors (n-type and p-type). Electrons from the n-type semiconductor will flow across the p-type, whereas holes in the p-type will move to the n-type [136]. In any case, a depletion layer is formed at the junction interface. In principle, n-p or p-n junctions can be forward or reverse biased [136]. Since a band-gap can be created in graphene (cf. Section D.2.B), it is therefore feasible to conceive of a graphene-semiconductor junction.

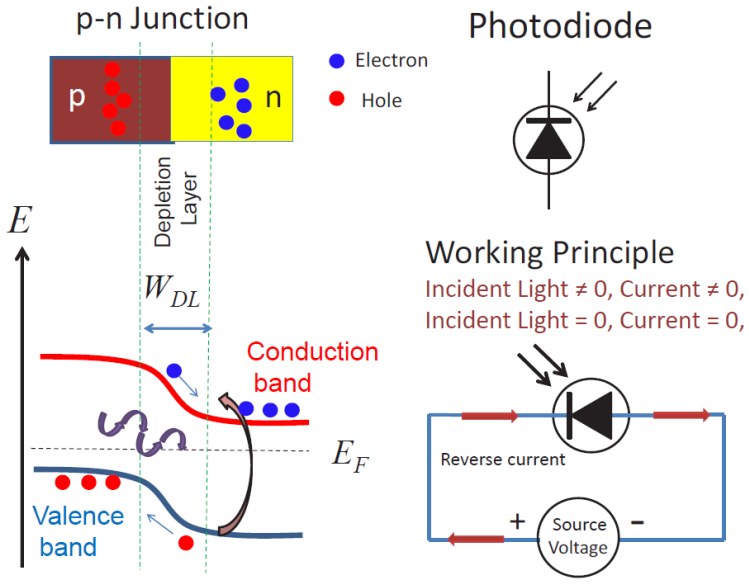

Figure D.10: A schematic of the photodiode is shown. The basic idea is that a reverse current flows upon illumination of the photodiode. The figure also emphasizes that a depletion layer is formed at the interface of the p-n junction.

Photodiodes are a key component for use in logical devices. It is a current generating device that is sensitive to incoming light (cf. Figure D.10 for the p-n junction configuration). In the absence of light, the device carries a high resistance. However, incoming photons can break down some of the bonding within the compounds at the depletion layer (cf. Figure D.10). Electrons and holes will then be created, and hence a drift current I_d flows across the diode [136]

$$I_d \approx c_1(1 - \exp(-c_2 W_{DL})) \ . \tag{D.15}$$

Here, c_1 is a constant associated with electric charge and photonic flux, W_{DL} is the width of the depletion layer, and c_2 is a constant associated with the photon energy and band-gap [108].

The working principle of the photodetector is similar to that of the photodiode, transforming photons into an observable current [96, 137] (cf. Figure D.11). More specifically, photons transfer energy to electrons, causing them to 'jump' from the valence band to conduction band (cf. interband transition). This has a typical timescale of $\sim$1 ps [102].

$$\gamma(\text{photon}) + e^-_{val} \rightarrow e^-_{con} \tag{D.16}$$

Here, e^-_{val} and e^-_{con} refer to electrons in the valence and conduction bands respectively. Bonaccorso et al. [96] point out that the absorption bandwidth of light spectra depends upon the choice of semiconductor. As we mentioned before, graphene interacts with an EM range covering the majority of the visible spectrum [96, 102]. Xia et al. [138] have also reported that the frequency response of graphene can be upwards of 40 GHz, with a theoretical

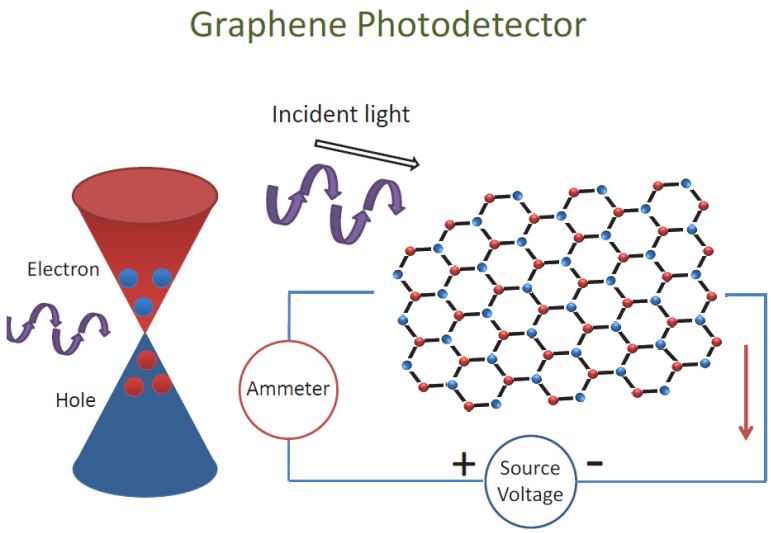

Figure D.11: This figure shows how electrons in the valence band can be excited to conduction band by incident photons. The conductivity of graphene increases, and a measurable current can flow around the circuit. In practice, the idea can be used to measure incident light intensity, for example.

limit reaching even 500 GHz. This response generally depends upon the electrical mobility, resistance and capacitance of the materials [102]. An appropriate bandwidth for graphene can therefore be adjusted via doping or an applied electric field. Mueller et al. [139] further reveal that their results for graphene display a strong photonic response at a wavelength of 1.55 μm, when applying the graphene photodetector on fast data communication links.

Bao et al. [102] have summarized that current from a photodetector can also be generated just by the contact of graphene and a semiconductor, due to the differing work functions and thermal gradient. Current leakage is one of the major drawbacks of the graphene photodetector, although this can be optimized by reducing the band-gap, or coating some dielectric material on

the graphene surface [96, 102]. Echtermeyer et al. [140] show that a number of metallic nanoparticles can be allocated on the graphene substrate, vastly improving the efficiency of the devices. The basic idea is that a metallic nanoparticle touches the graphene film, and forms a 'junction like' contact. Metallic nanoparticles on the graphene layer would thus act as small photodetectors at the same time, and thus enhance the sensitivity [140, 141].

Some other applications such as the measurement of refractive index [142], and the analysis of metamaterials via the graphene sensor [143], are all being studied on the graphene photonic detector platform.

B. Optical Modulator

The optical modulator is a photonic device which transforms electrical signals into an optical equivalent [137, 144, 145] (cf. Figure D.12 for a schematic overview). It is an essential communication link within many electronic devices, and can also alter the properties of light via doping or an applied electric field [102]. For example, assume a plane wave propagates as

$$A = |A| \exp(i\theta) \ , \tag{D.17}$$

where A can be either electric or magnetic in origin, and θ is the phase of the wave. A modulator changes the amplitude $|A|$ and phase θ of the input wave [102]. Graphene is a suitable material for a modulator since it has a strong response to a wide range of light spectra (i.e., bandwidth) [130, 144, 145]. Typically, graphene will be coated upon the silicon substrate to enhance the absorption rate [130].

Optical modulators can generally be divided into two types [102]. The

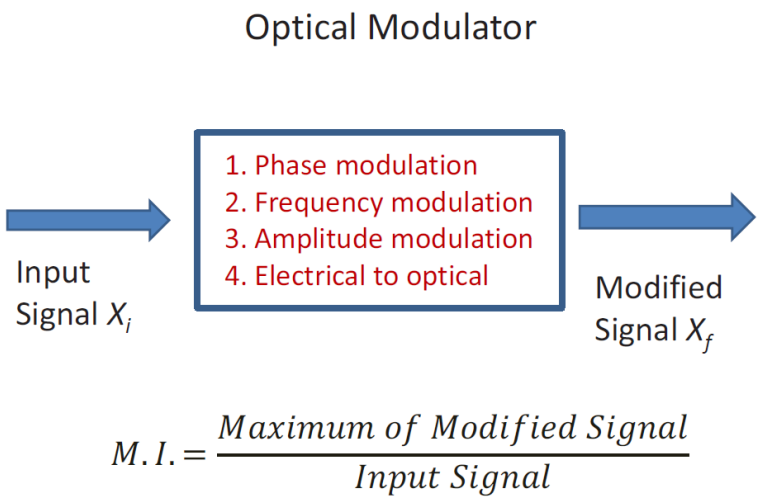

Figure D.12: The optical modulator is an important device for converting electrical signals into an optical equivalent, and therefore an ideal bridge between electronic and optical devices. This device can also change the properties of the incident wave, such as the phase, frequency, and amplitude. The Modulation Index ($M.I.$) is defined as the maximum of the modified signal X_f, divided by the input signal X_i.

first is an absorptive modulator, converting photons into some other form of energy. Normally, an absorption modulator can tune the transmitted light intensity via adjustment of the Fermi energy level E_F[102, 130]. The second type is a refractive modulator which can change the dielectric constant according to variation of the electric field. Graphene is a promising material for an absorption modulator due to its wide bandwidth and tunable Fermi energy level [96, 102]. Bao et al. [102] further reveal that the interband transition can be tuned to a logical ON/OFF state, dependent upon E_F . Regardless, graphene provides a high optical Modulation Index ($M.I.$),

making it an ideal material for any modulator [102]. This index is given by

$$M.I. = \frac{\max(X_f)}{X_i} \ , \tag{D.18}$$

where X_i and X_f refer to the variable before and after modulation respectively. The graphene modulator can also be applied to the optical resonator, allowing the wavelength to be altered (cf. for details [102]).

Recently, the dielectric sandwich - two layers of graphene with dielectric filling - has been used as an optical signaling modulator [144, 145]. Gosciniak et al. [144] estimate that this graphene optical modulator can reach speeds of up to 850 GHz, with 3 dB modulation and small losses. Liu et al. [145] have also reported a wide absorption range of 1.35-1.60 μm in wavelength.

C. Graphene Waveguide

A waveguide is a physical channel which traps light, guiding it through a designated path [124, 146]. For example, fiber-optic cable is a common waveguide for the communication of light signals - its high refractive index n_{op} trapping light inside the fiber [124]. As we have already seen, the refractive index depends upon the linear dielectric susceptibility χ_{R1} [102]. Zhang et al. [146] have studied the wave-modes of the graphene quantum well, identifying energy dispersion relations associated with Klein tunneling and classical wave-modes [146]. Zhang et al. [146] further note an absence of the third order classical, and first order tunneling wave-modes.

Graphene plasmonic waveguides have become an essential component for integration with logical devices [147, 148]. Kim et al. [147] have studed the plasmonic waveguide for a dielectric substrate coated on graphene, discover-

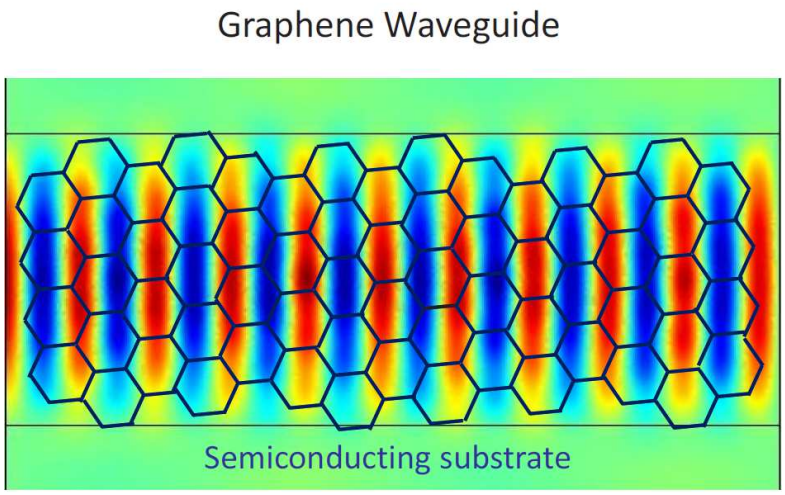

Figure D.13: Graphene is coated upon the semiconducting substrate, and either the TE or TM wavemodes can be transmitted along the graphene thin film.

ing little optical loss and very fast operating speeds. They show that at the peak wavelength $\lambda = 1.31\,\mu$m, the transmission ratio is around 19 dB for the TM mode [147].

D. Saturable Absorber

As we have already highlighted upon, saturable absorption refers to an absorption of photons decreasing as the light intensity increases [129, 149] (cf. Figure D.14). It is usually applied via the mode-locked laser [102, 150]. Many semiconductors exhibit saturable absorption, but are not as sensitive as graphene [102, 129]. The basic idea is as follows - a number of excited electrons occupy the conduction band during high intensity exposure, and

electrons in the valence band are no longer able to absorb photons due to the Pauli exclusion principle [102, 150]. This property originates from the nonlinear susceptibility of graphene for a short response time [96]. In application, a saturable absorber can be used to transform a continuous wave to a very short wave pulse [96]. Generally speaking, monolayer graphene provides a high saturable absorption coeffcient, and recently, some research has uncovered that CNTs may also be suitable candidate for a saturable absorber [149, 151]. Bao et al. [150] also report that a single layer graphene (SLG) saturable absorber can provide around 66% modulation depth, and produce picosecond wave pulses.

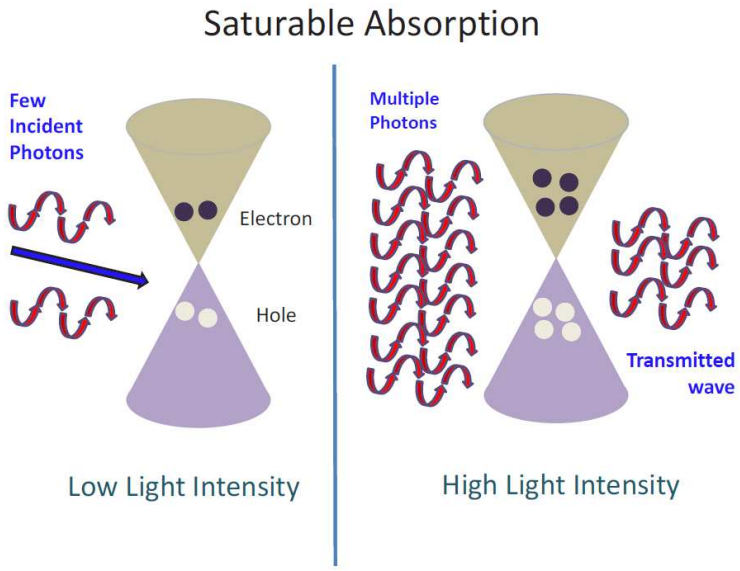

Figure D.14: The idea of saturable absorption for graphene is shown. Graphene can absorb photons, and create electron-hole pairs at low incident light intensity. However, electrons are incapable of occupying the conduction band at high light intensity, since most of the states have already been occupied (cf. Pauli exclusion principle).

E. Photonic Limiter

A photonic limiter is used to reduce the intensity of light that is emitted from the source [96, 102, 152, 153]. The mechanism is to permit the passage of low intensity light, and to filter out light of higher intensity [152, 153]. Dispersed graphene-oxide solutions are generally used for studying the optical limiter [149, 150]. In particular, graphene, has a strong response to a change of light intensity [102], with a transmittance $T(\mathrm{I})$ that is inversely dependent upon the light intensity I. Such a device can therefore, for example, be implemented to protect the human eye when working with laser apparatus [96]. Wang et al. [152] also note how graphene's nonlinear response is the working principle behind the reduction of light transmitted at high intensity, and also show that graphene can limit a wide range of the visible spectrum [152, 153].

According to Bao et al. [102], the reverse saturable absorption (opposite to saturable absorption) is the key nonlinear response that filters high intensity light, and subject to certain conditions. This relates to an optical limiter absorbing more high-energy photons than low-energy photons [102]. Lim et al. [149] have reported that, in practice, the property will change from saturable absorption to reverse saturable absorption, only when microplasmas or microbubbles appear. These lead to a nonlinear thermal scattering, which is also an important factor in limiting high intensity light [102]. Nevertheless, the graphene photonic limiter is still in the early stages of development, with more drastic efforts being required in the near future.

D.5 Transistors

Nowadays, field effect transistors (FETs) are a key component of most integrated circuitry, commonly acting as a simple logic gate. These devices can be of either n-p-n or p-n-p type, depending upon the desired operation. In this day and age, when the speed and size of devices are becoming all important, scientists are having to seek revolutionary new materials to replace the likes of Silicon (Si), Germanium (Ge) and Gallium Arsenide (GaAs). With outstanding electrical mobility, graphene-based materials are becoming evermore prominent as candidates within future transistors (cf. Figure D.15).

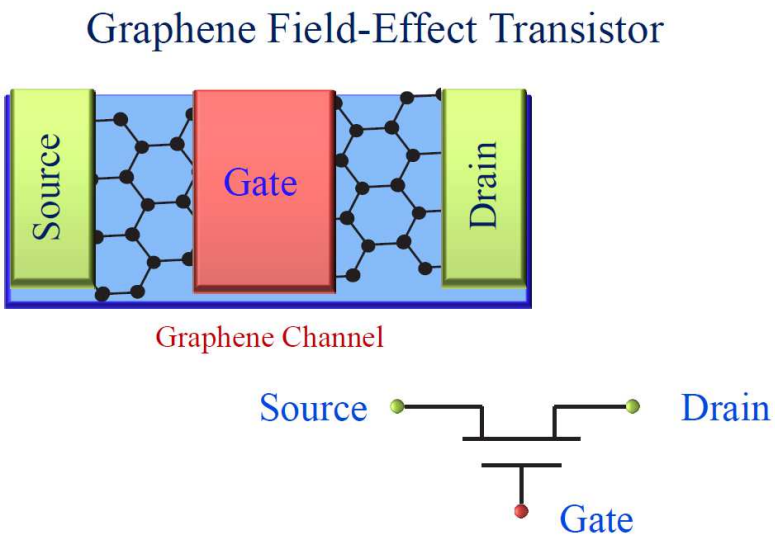

Figure D.15: The idea of the graphene FET is shown. The channel of the transistor is made of graphene, and a gate voltage V_G controls the current flow I_{DS} from drain to source.

A. Carbon Nanotube Transistor

Before we commence any in-depth discussion of this particular design [85, 86, 154], we must first discuss the physical properties of graphene nanoribbons (GNRs) [155] and carbon nanotubes (CNTs) [101, 156, 157, 158, 159]. A GNR is considered to be a piece of graphene of exceptionally narrow width [155]. The electrical attributes of GNRs are determined by their boundary conditions (BCs) (cf. Figure D.16). The 'armchair' BC can cause either metallic or semi-metallic behavior to be exhibited, whereas the zig-zag BC yields only metallic characteristics [101, 156, 157]. Therefore, GNRs are another means of generating an energy band-gap. In this case, the gap size is inversely proportional to the nanoribbon width.

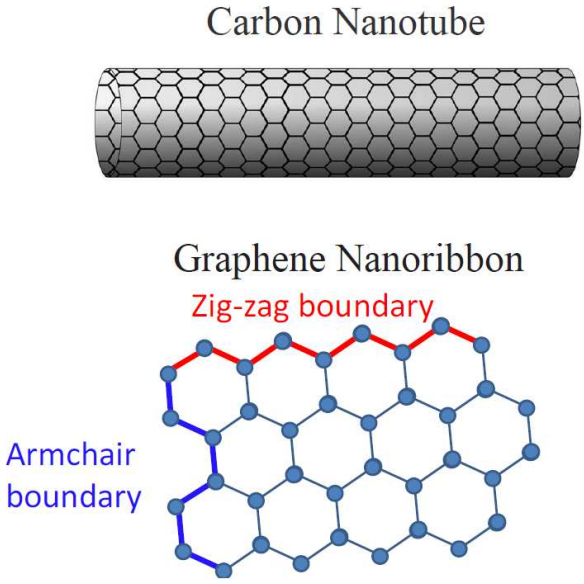

Figure D.16: The lower portion of this figure highlights the two possible boundary conditions (BCs) that a graphene nanoribbon (GNR) can satisfy. The zig-zag BC yields only a conducting state, whereas the armchair BC can either imply a conducting or semiconducting state (dependent upon the width of the nanoribbon). The GNR can also be curled to form a carbon nanotube (CNT), with a band-gap that is inversely proportional to its radius.

Carbon nanotubes are often considered to be one-dimensional structures, and can be formed by curling a GNR (typically 10-100 nm in width [101, 155]) into a cylindrical configuration (for further details concerning their fabrication, one can refer to [101, 158]). The nanotubes can either be single-walled or multi-walled, although this must be taken into account when considering the CNT radius r_{CNT} . Since this process leads to structural deformation of graphene's honeycomb lattice, there is an overall modification of the electronic band structure [101, 156, 157]. Quantum equivalents of the capacitance, inductance and resistance have all been exhibited within the electrical properties of CNTs, and an energy band-gap E_g is found to be inversely proportional to this CNT radius r_{CNT} [101],

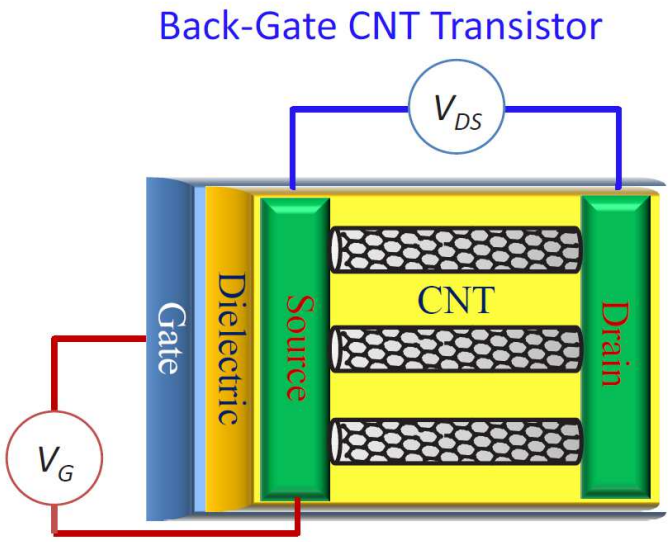

Figure D.17: The figure shows the back-gated CNT transistor. It contains multiple CNTs as the intermediary channels, providing stable performance and current flow. Since the device is back-gated, it can easily be applied within integrated circuitry.

$$E_g \sim 1/r_{CNT} \ . \tag{D.19}$$

Thus, together with graphene's capability for long-range ballistic transport (even at room temperature), this presents many useful applications. For example, CNTs would be an apt source-drain channel within semiconducting devices such as transistors [156].

For decades now, the CNT transistor has been subject to intense study [94, 101, 156, 160, 161, 162], with a recently reported high switching ratio [162]. They consume much less power, and can possess shorter channel lengths than their silicon-based counterparts. They can also exist in many forms, the most popular being the top-gate, back-gate and wrap-around gate designs [156, 163, 164, 165]. Recently, Shulaker et al. [163] have developed a simple computer from the CNT-based transistors, which can perform more than 20 different instructions. Figure D.17 provides a diagrammatic representation of how a back-gated multi-CNT transistor may look - the CNTs themselves acting as the intermediary channels. Currently, one can produce a purified CNT having less than 0.0001% impurity - which can minimize any inelastic scattering in the channel [164]. The ON/OFF drain-source current I_{DS} can be tuned by using an applied electric field (i.e., the gate voltage V_G) to act upon the CNT channel [164]. Moreover, the ballistic transport of electrons is a result of the one-dimensional CNT structure [101], which again restricts the degree of inelastic scattering. CNT transistors would also appear to alleviate the issue of the short-channel effect in silicon-based devices. In theory, the shorter the channel, the faster the transistor [94, 101]. However, usually when the channel has a length scale in tens of nanometers, the drain-source current I_{DS} tends to become most unstable [101]. A recent

study [161, 164] has revealed that the CNT channel can be as short as 9 nm, whilst maintaining a stable current. There are even some predictions that the CNT channel can reach even down to 7 nm in the near future [161, 164].

Schottky barriers at the channel-electrode contacts, are the major obstacle with regards to the CNT's application within transistors [165]. Specifically, they provide a large resistance at the CNT-electrode interface, due to the differing work-functions [101]. The Schottky barrier would generally downgrade the ON/OFF switching ratio [101, 165]. Even worse, this barrier is much larger than for silicon-based devices. A recent study by Javey et al. [165] reveals that the Schottky barrier would be greatly reduced when using the noble metal, Palladium (Pd) as the electrode. They also show that the CNT channel can even then maintain ballistic transport [165]. It is important to emphasize how both classical and quantum equivalents of inductance, resistance and capacitance are exhibited for CNT transistors [101]. In particular, quantum effects become most apparent at the nanoscale. Both quantum inductance and capacitance are determined by the size, BCs and the density of states (DoS) of the CNT [94, 101], whereas the quantum resistance is equal to $h/4e^2$.

B. Tunneling Transistor

1. Mechanisms of Tunneling

As we have already highlighted upon many times now, the absence of a well-defined OFF state in the graphene transistor is a major setback [166, 167]. Assuming a band-gap were to be created, the next hurdle to overcome is the back-current leakage during this OFF state, since this downgrades the

power efficiency [166, 167]. Furthermore, opening this band-gap would then reduce the mobility of graphene, with the Dirac fermions being subject to some inelastic scattering [167].

The tunneling graphene transistor is a revolutionary new concept, and may be capable of alleviating some of the aforementioned drawbacks. It consumes very little power (up to 109 times less than silicon-based devices [168]) and possesses a very fast response time (steep sub-threshold slope) [94]. Michetti et al. also report that an ON/OFF switching ratio can reach as high as 10^4, even with a small electric field [169, 170, 171]. It is also found that tunneling occurs at exceptional speed [171]. The underlying concept is visualized in Figure D.18. The interband tunneling is tuned via an applied drain-source voltage V_{DS} and gate voltage V_G [167, 172]. Both V_{DS} and V_G are used to accumulate the electrons and holes in upper and lower graphene layers respectively, and thus altering the shape of the potential barrier [173]. The tunneling is also associated with the channel length, and thickness of the gate oxide layer t_{ox} [169].

2. Vertical Design

A relatively new concept which relies upon vertical tunneling has been developed by the Manchester research group [166, 167]. The graphene-based device consists of a few (insulating) layers of hexagonal Boron Nitride (hBN) or molybdenum disulphide (MoS_2) [174, 175, 176]. These are positioned between two graphene sheets which then constitute the electrodes (cf. Figure D.19). The key point here, is that the insulating layers act as a barrier, and thus preventing the flow of current. As such, there is no need for a well-defined band-gap in graphene [174, 175, 176]. This has the added benefit of

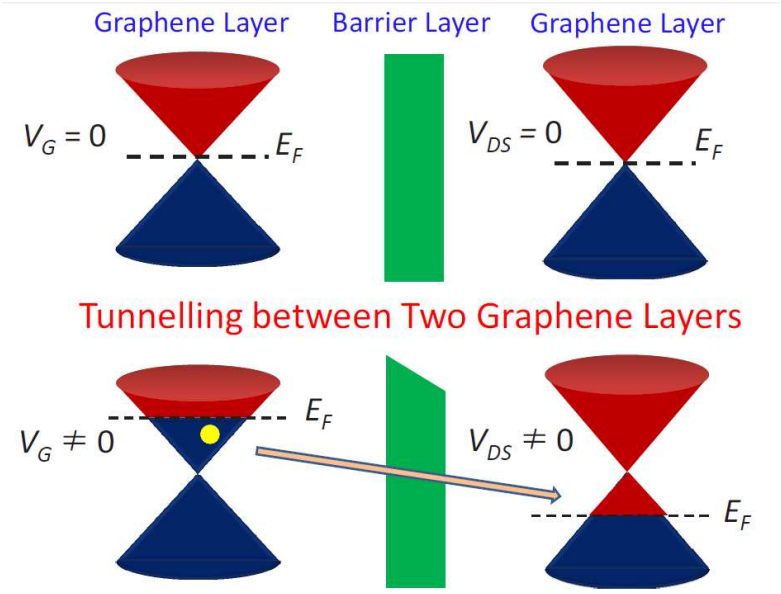

Figure D.18: The upper figure shows an intermediate barrier separating the two layers of graphene. In the absence of external electric fields, the Fermi energies are situated at the Dirac points. When the gate voltage V_G and drain-source voltages V_{DS} are applied, electrons begin to accumulate in the conduction band of one graphene layer, and holes in the other. Tunneling can readily occur in this situation, via a fine tuning of both voltages.

greatly reducing any current leakage whilst in the OFF state [174, 175, 176]. The whole process of current tunneling then acts perpendicular to the layers [174, 175, 176]. Electrons in the bottom graphene layer will begin to accumulate once a gate voltage V_G is applied across the lower insulating layer [177, 178]. The drain-source voltage V_{DS} is then added to create holes in the upper graphene layer [166, 174, 175, 176]. This has the desired effect of increasing the Fermi energy E_F in bottom graphene layer, and decreasing E_F in the upper layer. Electrons in the bottom graphene layer are then capable of tunneling to the top graphene layer [167]. A recent study by Georgiou

et al. [174] reveals that the current modulation can reach a high value of 10^6 (even at room temperature). It is also interesting to note that a resonant tunneling within the vertical transistor occurs in some energy states, and a negative differential conductance exists (i.e., current decreases upon an increase in voltage) [175, 176].

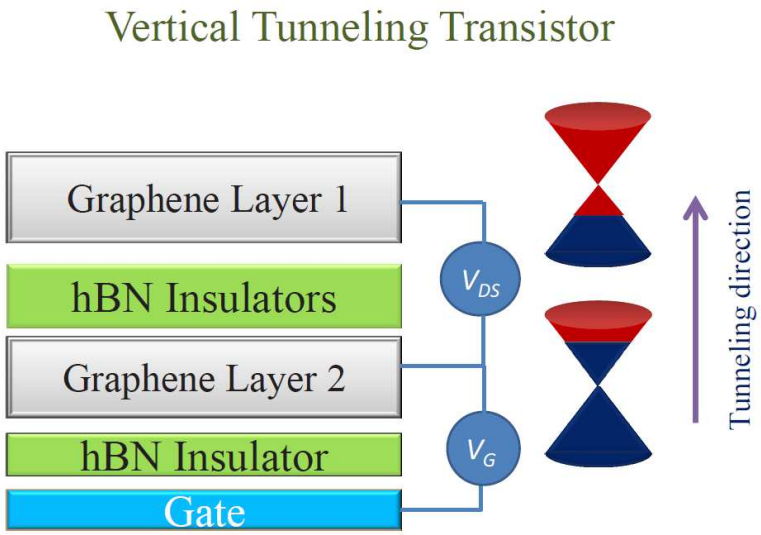

Figure D.19: The vertical tunneling graphene transistor is shown. The hexagonal Boron Nitride (hBN) insulating layers act as an intermediary barrier. The accumulation of holes in the upper graphene layer is controlled by the drain-source voltage V_{DS}, whereas the build-up electrons in the lower graphene layer can be tuned via the gate voltage V_G . Electrons are then capable of tunneling from the bottom to top layer of graphene.

C. High Frequency Devices

High frequency transistors do not require an OFF state, and can operate solely through variations of the current or voltage signaling [94, 179].

Graphene may thus be applicable within the realms of high-frequency transistors, inverters, or operational amplifiers [94, 147, 180]. Graphene's response to these signals is incredibly fast, with operating speeds of around a few hundred GHz [147, 179, 181, 182, 183].

The performance of high frequency devices is characterized by two important parameters - the cut-off frequency f_{cut} and maximum oscillation frequency f_{max}. The cut-off frequency f_{cut} is given by a current gain G_I equal to unity [179]

$$G_I = 20\, log_{10}\left(\frac{I_{out}}{I_{in}}\right) \ , \tag{D.20}$$

where I_{out} and I_{in} are the output and input currents respectively. Typically, f_{cut} is proportional to the trans-conductance g_{rf} and the thickness of the gate oxide layer t_{ox}, whereas inversely proportional to the transistor gate length L_G and gate width W_G [94, 179]. The whole expression is given by

$$f_{cut} = c_1 \frac{t_{ox}\, g_{rf}}{L_G\, W_G} \ , \tag{D.21}$$

where c_1 is a constant associated with dielectric gate. In experiments, one would only shorten the gate length L_G for simplicity, thereby increasing the cut-off frequency. Wu et al [179] report that with CVD-prepared graphene, f_{cut} can reach upwards of 155 GHz for a relatively short gate length of 40 nm. Theoretical simulations have indicated that a cut-off frequency of 1 THz can be attained for just a few nanometers gate length [181].

Similar to f_{cut}, the maximum oscillation frequency f_{max} is obtained for a power gain G_P equal to one. Here, we have $G_P = 10\, log_{10}(P_{out}/P_{in})$, where P_{out} and P_{in} are the output and input powers respectively [179]. The value of

f_{max} in graphene-based devices is slightly more complicated, and is dependent upon the cut-off frequency, gate resistances, and the trans-conductance g_{rf} [179, 181]. A recent report [179] has mentioned that f_{max} can reach up to 20 GHz. However, it is important to note that a short gate length would not necessarily imply a high value for f_{max} [179, 181]. At present, not much is understood of the $I - V$ characteristic curve - this has three regions, firstly linear, then saturating, and finally a second linear region [94, 179, 181]. In addition, a change of gate voltage V_G would alter the shape of the $I-V$ curve, and making the saturation region ambiguous. Without a stable saturation region, the value of f_{max} is limited. This problem will require urgent attention in the near future, if the high-frequency transistor is to make any headway [147, 184].

D.6 Summary

Graphene's outstanding capabilities have drawn the attention of scientists from several interdisciplinary backgrounds - all looking to take advantage. This stand-alone two-dimensional structure is a playground for Dirac fermions which possess a zero effective mass [67, 185, 186]. Quantum phenomena have been observed even at room temperature; a series of anomalous quantum effects including QHE and Klein tunneling [64, 117]. Graphene's versatility is nigh on endless - in this paper, we have merely focused upon optoelectronic devices and transistors. Optical communications provide a much wider bandwidth, with higher efficiencies than most typical conducting wire. We are thus dawning upon a new golden photonic age of higher internet speeds, and entertainment-based devices. Graphene's high transmittance, strong interaction of light with ultra-fast response time, wide absorption spectrum,

and tunable optical conductivity [96, 102, 130], present an ideal material for optical devices! Amongst many others, these include the photodetector, optical modulator, plasmonic waveguide and also the saturable absorber. The absence of any discernible band-gap for graphene is an unavoidable issue for logical devices, although one may be created via various methods (e.g., structural deformation or chemical doping) [94]. The CNT transistor is now a well-established technology - developed over more than 30 years. Only now has the dream of a CNT-based computer become a working reality [163]. Carriers in CNT channels can perform ballistic transport, even for very short lengths. However, the graphene vertical tunneling transistor is something rather novel. This device itself does not require band-gap at all, and yet, both operates at exceptional speeds, whilst consuming very little power. Our final talking point was the high frequency transistor, which acts as amplifier in the circuit rather than a typical logical device. The cut-off frequency can reach theoretical estimates of up to 1 THz, for just a few nanometers of gate length [101]. Although we have plainly made the case for graphene's implementation within numerous optical and electronic devices, there are a few obstacles which we must overcome. These are the nonlinear $I-V$ characteristic curve, and the emergence of Schottky barriers (although we mention a suitable fix). Fifty years ago, no one would have ever envisaged that optical or silicon-based devices would have their place in everyday life. Graphene may change the world!

Bibliography

[1] **Einstein A.** Zur Elektrodynamik bewegter Körper. *Ann. Phys.* 322 (10): 891–921, 1905.

[2] **Eötvös RV** *Mathematische und Naturwissenschaftliche Berichte aus Ungarn* 8: 65, 1890.

[3] **Vessot et al.** Test of Relativistic Gravitation with a Space-Borne Hydrogen Maser. *Phys. Rev. Lett.* 45: 2081–2084 (1980).

[4] **Jarosik et al.** Seven-year Wilkinson microwave anisotropy probe (WMAP) observations: sky maps, systematic errors, and basic results. *Astrophys. J. Suppl. Ser.* 192: 14, 2011.

[5] **Smoot et al.** Structure in the COBE differential microwave radiometer first-year maps. *Astrophys. J.* 396: L1–L5, 1992.

[6] **Riess et al.** Observational evidence from supernovae for an accelerating universe and a cosmological constant. *Astron. J.* 116: 1009–1038, 1998.

[7] **Perlmutter et al.** Measurements of Ω and Λ from 42 high-redshift supernovae. *Astrophys. J.* 517: 565–586, 1999.

[8] **Bergstrom L.** Dark matter constituents. *Nucl. Phys.* 138: 123–129, 2005.

[9] **Boyle LA, Caldwell RR, Kamionkowski M.** Spintessence! New models for dark matter and dark energy. *Phys. Lett.* 545: 17–22, 2002.

[10] **Planck Collaboration et al.** Planck 2013 results. XVI. Cosmological parameters. *arXiv:1303.5076v3 [astro-ph.CO].*

[11] **Benoit-Levy A.** Early Universe @ UCL: How Planck maps all the matter in the Universe, May 2013.
`http://www.earlyuniverse.org/the-planck-lensing-map-a-k-a-how-a-cmb-experiment-gives-a-map-of-all-the-matter-in-the-universe/`.

[12] **Steinhardt PJ, Turok N.** Why the cosmological constant is small and positive. *Science* 312: 5777, 1180–1183, 2006.

[13] **Tegmark et al.** Cosmological parameters from SDSS and WMAP. *Phys. Rev. D* 69: 103501, 2004.

[14] **Riess et al.** Type Ia supernova discoveries at $z > 1$ from the Hubble space telescope: Evidence for past deceleration and constraints on dark energy evolution. *Astrophys. J.* 607: 665, 2004.

[15] **David W, De-Santiago J, Wang Y.** Inhomogeneous vacuum energy. *Class. Quantum Grav.* 29: 145017, 2012.

[16] **Copeland EJ, Sami M, Tsujikawa S.** Dynamics of dark energy. *Int. J. Mod. Phys. D* 15: 1753, 2006.

[17] **Weinberg S.** The cosmological constant problem. *Rev. Mod. Phys.* 61: 1–23, 1989.

[18] **Valle DC, Mielke EW.** Solitonic axion condensates modelling dark matter halos. *Ann. Phys. NY* 336: 245–260, 2013.

[19] **Gegenberg J, Kelly PF, Mann RB, Vincent D.** Theories of gravitation in two dimensions. *Phys. Rev. D* 37: 3463–3471, 1988.

[20] **Katanaev MO, Volovich IV.** Two-dimensional gravity with dynamical torsion and strings. *Ann. Phy. NY* 197: 1–32, 1990.

[21] **Teitelboim C.** *Quantum theory of gravity,* edited by Christensen SM. Bristol: Hilger, 1984, p. 327.

[22] **Teitelboim C.** Gravitation and Hamiltonian structure in two space-time dimensions. *Phys. Lett.* 126: 41–45, 1983.

[23] **Brown JD, Henneaux M, Teitelboim C.** Black holes in two space-time dimensions. *Phys. Rev. D* 33: 319–323, 1986.

[24] **Brown JD.** *Lower dimensional gravity.* Singapore: World Scientific, 1988.

[25] **Mann RB, Shiekh A, Tarasov L.** Classical and quantum properties of two-dimensional black holes. *Nucl. Phys.* 341: 134–154, 1990.

[26] **Sikkema AE, Mann RB.** Gravitation and cosmology in (1+1) dimensions. *Class. Quantum Grav.* 8: 219, 1991.

[27] **Chan KCK, Mann RB.** Cosmological models in two space-time dimensions. *Class. Quantum Grav.* 10: 913, 1993.

[28] **Zioutas K, Hoffmann DHH, Dennerl K, Papaevangelou T.** What is dark matter made of? *Science,* 306: 5701, 1485–1488, 2004.

[29] **Ostriker JP, Steinhardt P.** New light on dark matter. *Science,* 300: 5627, 1909–1913, 2003.

[30] **Gaillard MK, Kain B.** Is the universal string axion the QCD axion? *Nucl. Phys.* 734: 116–137, 2006.

[31] **Schunck FE, Kusmartsev FV, Mielke EW.** Dark matter problem and effective curvature Lagrangians. *Gen. Relativ. Gravit.* 37: 1427–1433 , 2005.

[32] **Mielke EW, Kusmartsev FV, Schunck FE.** Inflation, bifurcations of non-linear curvature Lagrangians and dark energy, in *Proceedings of the 11th Marcel Grossmann Meeting (MG11) in Berlin, Germany, July 23-29, 2006* edited by Kleinert H, Jantzen RT and Ruffini R. Singapore: World Scientific, 2008, p. 824–843.

[33] **Mielke EW, Schunck FE.** Reconstructing the inflaton potential for an almost flat COBE spectrum. *Phys. Rev. D* 52: 672–678, 1995.

[34] **Mielke EW, Peralta HH.** Flattened halos in a non-topological soliton model of dark matter. *Phys. Rev. D* 70: 123509, 2004.

[35] **Mielke EW, Schunck FE.** Non-topological scalar soliton as dark matter halo. *Phys. Rev. D* 66: 023503, 2002.

[36] **Mielke EW, Peralta HH.** Eigenvalues of the third order slow-roll approximation of inflation. *Phys. Rev. D* 66: 123505, 2002.

[37] **Mielke EW, Schunck FE.** Boson stars: alternatives to primordial black holes? *Nucl. Phys.* 564: 185–203, 2000.

[38] **Schunck FE, Mielke EW.** General relativistic boson stars *Class. Quantum Grav.* 20: 20, 2003.

[39] **Liddle AR, Urena-Lopez LA.** Inflation, dark matter and dark energy in the string landscape. *Phys. Rev. Lett.* 97: 161301, 2006.

[40] **Mielke EW, Velez Perez JA.** Axion condensate as a model for dark matter halos. *Phys. Lett.* 671: 174–178, 2006.

[41] **Fuchs B, Mielke EW.** Scaling behaviour of a scalar field model of dark matter halos. *Mon. Not. Roy. Astron. Soc.* 350: 707, 2004.

[42] **Sanders R.** Hubble spots mysterious dark matter 'core'. *Universe Today,* March 2, 2012.

[43] **Benitez J, Macias A, Mielke EW, Obregon O, Villanueva VM.** From inflationary COBE potentials to higher-order curvature scalar Lagrangians. *Int. J. Mod. Phys.* 12: 16, 2835–2854, 1997.

[44] **Magnano G, Sokolowski LM.** Physical equivalence between nonlinear gravity theories and a general-relativistic self-gravitating scalar field. *Phys. Rev. D.* 50: 5039–5059, 1994.

[45] **Carroll SM, Duvvuri V, Trodden M, Turner MS.** Is cosmic speed-up due to new gravitational physics? *Phys. Rev. D.* 70: 043528, 2004.

[46] **Carosi G.** Finding the axion: The search for the dark matter of the universe. *AIP Conf. Proc.* 899: 30, 2007.

[47] **Duff MJ.** Strong/weak coupling duality from the dual string. *Nucl. Phys.* 442: 47–63, 1995.

[48] **Misner CW, Thorne KS, Wheeler JA.** *Gravitation,* W. H. Freeman, 1973.

[49] **Klein O.** Quantum theory and five-dimensional relativity. *Zeit. f. Physik* 37: 895, 1926.

[50] **Straub WO.** Kaluza-Klein Theory, December 2008. `http://www.weylmann.com/kaluza.pdf`.

[51] **Wilczek F.** Two Applications of Axion Electrodynamics. *Phys. Rev. Lett.* 58: 1799–1802, 1987.

[52] **'t Hooft G.** Symmetry Breaking through Bell-Jackiw Anomalies. *Phys. Rev. Lett.* 37: 8, 1976.

[53] **Callan C, Dashen R, Gross D.** The structure of the gauge theory vacuum. *Phys. Lett.* 63: 334–340, 1976.

[54] **Jackiw R, Rebbi C.** Vacuum Periodicity in a Yang-Mills Quantum Theory. *Phys. Rev. Lett.* 37: 172, 1976.

[55] **Hartnoll SA.** Lectures on holographic methods for condensed matter physics. *arXiv:0903.3246 [hep-th]*, 2010.

[56] **Maldacena JM.** The large N limit of superconformal field theories and supergravity. *Int. J. Theor. Phys.* 38: 1113–1133, 1999.

[57] **Parks RD.** *Superconductivity.* Marcel Dekker Inc., 1969.

[58] **Hartnoll SA, Herzog CP, Horowitz GT.** Building a Holographic Superconductor. *Phys. Rev. Lett.* 101: 031601, 2008.

[59] **Lewis CL.** Explicit gauge covariant Euler-Lagrange equation. *Am. J. Phys.* 77: 839, 2009.

[60] **Linde A.** A New Inflationary Universe Scenario: A Possible Solution of the Horizon, Flatness, Homogeneity, Isotropy and Primordial Monopole Problems. *Phys. Lett. B* 108: 389–392, 1982.

[61] **Kusmartsev FV, Mielke EW, Obukhov YN, Schunck FE.** Classification of inflationary Einstein-scalar-field models via catastrophe theory. *Phys. Rev. D* 51: 924, 1995.

[62] **Kusmartsev FV.** Application of catastrophe theory to molecules and solitons. *Phys. Rep.* 183: 1–35, 1989.

[63] **Guth AH.** Inflationary universe: A possible solution to the horizon and flatness problems. *Phys. Rev. D* 23: 347, 1981.

[64] **Geim AK, Novoselov KS.** The rise of graphene. *Nature Mater.* 6: 183–191, 2007.

[65] **Meyer JC.** The structure of suspended graphene sheets. *Nature* 446: 60–63, 2007.

[66] **Geim AK.** Graphene: status and prospects. *Science* 324: 1530–1534, 2009.

[67] **Geim AK.** Graphene prehistory. *Phys. Scr. T146* 014003: 2012, 2012.

[68] **Katsnelson MI.** Graphene: carbon in two dimensions. *Materials Today* 10: 20–27, 2007.

[69] **Novoselov KS et al.** Two-dimensional atomic crystals. *PNAS* 102: 10451–10453, 2005.

[70] **Savage N.** Materials science: Super carbon. *Nature* 483: S30–S31, 2012.

[71] **Wallace PR.** The Band Theory of Graphite. *Phys. Rev.* 71: 622–634, 1947.

[72] **O'Hare A, Kusmartsev FV, Kugel KI.** A stable flat form of two-dimensional crystals: could graphene, silicene, germanene be minigap semiconductors. *Nano Lett.* 12: 1045–1052, 2012.

[73] **Novoselov KS et al.** Electric Field Effect in Atomically Thin Carbon Films. *Science.* 306: 666–669, 2004.

[74] **Novoselov KS.** Two-Dimensional Gas of Massless Dirac Fermions in Graphene. *Nature* 438: 197–200, 2005.

[75] **Iyechika Y.** Application of graphene to high-speed transistors: expectations and challenge Science and Technology Trends - Quarterly Review 3776–3792, 2010.

[76] **Hlawacek G et al., Beilstein J.** Imaging ultra thin layers with helium ion microscopy: Utilizing the channeling contrast mechanism. *Nanotechnol.* 3: 507–512, 2012.

[77] **Robinson JA et al.** Correlating Raman Spectral Signatures with Carrier Mobility in Epitaxial Graphene: A Guide to Achieving High Mobility on the Wafer Scale. *Nano Lett.* 9: 2873–2876, 2009.

[78] **Gouider Trabelsi AB, Ouerghi A, Kusmartseva OE, Kusmartsev FV, Oueslati M.** Raman spectroscopy of four epitaxial graphene layers: Macro-island grown on 4H-SiC0001 substrate and an associated strain distribution. *Thin Solid Films* 539: 377–383, 2013.

[79] **Das A, Pisana S, Chakraborty B, Piscanec S, Saha SK, Waghmare UV, Novoselov KS, Krishnamurthy HR, Geim AK, Fer-**

rari AC, Sood AK. Monitoring dopants by Raman scattering in an electrochemically top-gated graphene transistor. *Nature Nanotechnol.* 3: 210–215, 2008.

[80] **Bae S et al.** Roll-to-roll production of 30-inch graphene films for transparent electrodes. *Nature Nanotechnol.* 5: 574–578, 2010.

[81] **Chen JH, Jang C, Xiao S, Ishigami M, Fuhrer MS.** Intrinsic and Extrinsic Performance Limits of Graphene Devices on SiO2. *Nature Nanotechnol.* 3: 206–209, 2008.

[82] **Bolotin KI et al.** Ultrahigh electron mobility in suspended graphene. *Solid State Commun.* 146: 351–355, 2008.

[83] **Morozov SV et al.** Giant Intrinsic Carrier Mobilities in Graphene and Its Bilayer. *Phys. Rev. Lett.* 100: 016602, 2008.

[84] **Lin YM et al.** Enhanced Performance in Epitaxial Graphene FETs with Optimized Channel Morphology. *IEEE* 32: 1343, 2011.

[85] **He QY, Wu SX, Yin ZY, Zhang H.** Graphene-based electronic sensors. *Chem. Sci.* 3: 1764–1772, 2012.

[86] **He QY et al.** Transparent, flexible, all-reduced graphene oxide thin film transistors. ACS Nano 5: 082117, 2011.

[87] **Neto AHC, Novoselov KS.** New directions in science and technology: two-dimensional crystals. *Rep. Prog. Phys.* 74: 082501, 2011.

[88] **Pumarol ME et al.** Direct nanoscale imaging of ballistic and diffusive thermal transport in graphene nano-structures. *Nano Lett.* 12: 2906–2911, 2012.

[89] **Prasher R.** Graphene spreads the heat. Science 328: 185–186, 2010.

[90] **Seol JH et al.** *Science* 328, 213–216 (2010).

[91] **Chen S.** Thermal conductivity of isotopically modified graphene. *Nature Mater.* 11: 203–207, 2012.

[92] **Raffee J.** Wetting transparency of graphene. *Nature Mater.* 11: 217–222, 2012.

[93] **Engel M et al.** Light matter interaction in a micro-cavity controlled graphene transistor room temperature transistor based on a single carbon nanotube. *Nature Commun.* 3: 906–911, 2012.

[94] **Schwierz F.** Graphene transistors. *Nature Technology* 5: 487–496, 2010.

[95] **Kusmartsev FV, Tsvelik AM.** Semi-metallic properties of a heterojunction. *JETP Lett.* 42: 257–260, 1985.

[96] **Bonaccorso F, Sun Z, Hasan T, Ferrari AC.** Graphene photonics and optoelectronics. *Nature Photonics* 4: 611–622, 2010.

[97] **Sarma SD, Adam S, Hwang EH, Rossi E.** Electronic transport in two-dimensional graphene. *Rev. Mod. Phys.* 83: 407–470, 2011.

[98] **Zhou YB, Wu HC, Yu DP, Liao ZM** Magneto-resistance in graphene under quantum limit regime. *Appl. Phys. Lett.* 102: 093116, 2013.

[99] **Du X, Skachko I, Barker A, Andrei EY.** Approaching ballistic transport in suspended graphene. *Nature Nanotechnol.* 3: 491–495, 2008.

[100] **Koh YK, Bae MH, Cahill DG, Pop E.** Heat conduction across monolayer and few-layer graphenes. *Nano Lett.* 10: 4363–4368, 2010.

[101] **Avouris P, Chen Z, Perebeinos V.** Carbon-based electronics. *Nature Nanotech.* 2: 605–615, 2007.

[102] **Bao Q, Loh KP.** Graphene photonics, plasmonics, and broadband optoelectronic devices. *ACS Nano*, 6: 3677–3694, 2012.

[103] **Avouris P.** Graphene photonics and optoelectronics. *Nano Lett.* 10: 4285–4294, 2010.

[104] **Saleh EA, Teich MC.** *Fundamentals of Photonics*, Wiley Series in Pure and Applied Optics, 2007.

[105] **Kasap SO.** *Optoelectronics Photonics: Principles Practices*, Prentice Hall, 2001.

[106] **Koppens FHL, Chang DE, Garca de Aba jo FJ.** Graphene plasmonics: A platform for strong light-matter interactions. *Nano Lett.* 11: 3370–3377, 2011.

[107] **Britnell L et al.** Strong Light-Matter Interactions in Heterostructures of Atomically Thin Films. *Science Comm.* 340: 1311, 2013.

[108] **Rosencher E.** *Optoelectronics*, Cambridge University Press, 2002.

[109] **Rudden MN, Wilson J.** *Element of Solid State Physics.* New York Wiley Ch. 4-6, 1993.

[110] **Irwin JD, Kerns DV.** *Introduction to Electrical Engineering.* New Jersey: Prentice Hall, Ch. 8-9, 1995.

[111] **Turton R.** *The Physics of Solids.* New York: Oxford University Press, Ch. 4-6, 2000.

[112] **Kim KS et al.** Large-scale pattern growth of graphene films for stretchable transparent electrodes. *Nature* 457: 706–710, 2009.

[113] **Fan X, Shen Z, Liu AQ, Kuo JL.** Band gap opening of graphene by doping small boron nitride domains. *Nanoscale* 4: 2157–2165, 2012.

[114] **Shinde PP, Kumar Y.** Direct band gap opening in graphene by BN doping: Ab initio calculations. *Phys. Rev. B* 84: 125401, 2011.

[115] **Coletti C, Riedl C, Lee DS, Krauss B, Patthey L, von Klitzing K, Smet JH, Starke U.** Charge neutrality and band-gap tuning of epitaxial graphene on SiC by molecular doping. *Phys. Rev. B* 81: 235401, 2010.

[116] **Terrones H, Lv R, Terrones M, Dresselhaus MS.** The role of defects and doping in 2D graphene sheets and 1D nanoribbons. *Rep. Prog. Phys.* 75: 062501, 2012.

[117] **Katsnelson MI, Novoselov KS, Geim AK.** Chiral tunneling and the klein paradox in graphene. *Nature Phys.* 2: 620–625, 2006.

[118] **Dean CR et al.** Multicomponent fractional quantum Hall effect in graphene. *Nature Phys.* 7: 693–696, 2011.

[119] **Novoselov KS et al.** Room-temperature quantum hall effect in graphene. *Science* 315: 1379, 2007.

[120] **Calogeracos A.** Paradox in a pencil. *Nature Phys.* 2: 579–580, 2006.

[121] **Zalipaev VV, Maksimov DN, Linton CM, Kusmartsev FV.** Spectrum of localized states in graphene quantum dots and wires. *Phys. Lett. A* 377: 216–221, 2013.

[122] **Hartmann RR, Robinson NJ, Portnoi ME.** Smooth electron waveguides in graphene. *Phys. Rev. B* 81: 245431, 2010.

[123] **Williams JR, Low T, Lundstrom MS, Marcus CM.** Gate-controlled guiding of electrons in graphene. *Nat. Nanotech.* 6: 222–225, 2011.

[124] **Wu Q, Turpin JP, Werner DH.** Integrated photonic systems based on transformation optics enabled gradient index devices. *Light: Science and Applications* 38, 2012.

[125] **Downing CA, Stone DA, Portnoi ME.** Zero-energy states in graphene quantum dots and rings. *Phys. Rev. B* 84: 155437, 2011.

[126] **Stone DA, Downing CA, Portnoi ME.** Searching for confined modes in graphene channels: The variable phase method. *Phys. Rev. B* 86: 075464, 2012.

[127] **Shannon CE.** Communication in the presence of noise. *Proc. Inst. of Radio Engs* 37: 10–21, 1949.

[128] **Gan X et al.** High-Contrast Electro-optic Modulation of a Photonic Crystal Nanocavity by Electrical Gating of Graphene. *Nano Lett.* 13: 691–696, 2013.

[129] **Avouris P, Xia FN.** Graphene applications in electronics and photonics. *Material Research Soc.* 37: 1225–1234, 2012.

[130] **Avouris P, Freitag M.** Graphene Photonics, Plasmonics, and Optoelectronics. *IEEE* 20: 600012, 2013.

[131] **Butcher PN, Cotter D.** *The Elements of Nonlinear Optics.* Cambridge University Press, 1991.

[132] **Lu L, Cheong LL, Smith HI, Johnson SG, Joannopoulos JD, Soljacic M.** Three-dimensional photonic crystals by large-area membrane stacking. *Optics Lett.* 37: 47264728, 2012.

[133] **Joannopoulos JD, Johnson SG, Winn JN, Meade RD.** *Photonic Crystals: Molding the Flow of Light*. Princeton Univ. Press, 2008.

[134] **Moktadir Z, Charlton M, Pollard M, Mizuta H, Rutt H.** *Tunable transmission in a graphene photonic crystal in mid-infrared*. Graphene 2011 Conference, Bilbao, Spain, 11-14 Apr 2011.

[135] **Majumdar A, Kim J, Vuckovic J, Wang F.** Graphene for Tunable Nanophotonic Resonators *IEEE* 20:4600204, 2014.

[136] **Mohan Kumar D.** Optoelectronic devices and their applications. *Electr. For You*, Oct 2003.

[137] **Furchi M et al.** Microcavity-integrated graphene photodetector. *Nano. Lett.*, 12: 2773-2777, 2012.

[138] **Xia F, Mueller T, Lin YM, Garcia AV, Avouris P.** Ultrafast graphene photodetector. *Nature Nanotech.* 4: 839–843, 2009.

[139] **Mueller T, Xia F, Avouris P.** Graphene photodetectors for high-speed optical communications. *Nature Photonics* 4: 297–301, 2010.

[140] **Echtermeyer TJ el al.** Strong plasmonic enhancement of photovoltage in graphene. *Nature Communications*, 2: 458, 2011.

[141] **Nicoletti O et al.** Three-dimensional imaging of localized surface plasmon resonances of metal nanoparticles. *Nature*, 502: 80–84, 2013.

[142] **Xing F el al.** Sensitive Real-Time Monitoring of Refractive Indexes Using a Novel Graphene-Based Optical Sensor. *Scientific Reports* 2: 908, 2012.

[143] **Amin M, Farhat M, Bagci H.** A dynamically reconfigurable Fano metamaterial through graphene tuning for switching and sensing applications. *Scientific Reports* 3: 2105, 2013.

[144] **Gosciniak J, Tan DTH.** Theoretical investigation of graphene-based photonic modulators. *Scientific Reports* 3: 1897, 2013.

[145] **Liu M et al.** A graphene-based broadband optical modulator. *Nature* 474: 64–67, 2011.

[146] **Zhang FM, He Y, Chen X.** Guided modes in graphene waveguides. **Appl. Phys. Lett.**, 94: 212105, 2009.

[147] **Kim JT, Choi SY.** Graphene-based plasmonic waveguides for photonic integrated circuits. *Optic Express* 19: 24557–24562, 2011.

[148] **Wang X, Cheng Z, Xu K, Tsang HK, Xu JB.** High-responsivity graphene/silicon-heterostructure waveguide photodetectors. *Nature Photonics* 7: 888–891, 2013.

[149] **Lim GK et al.** Giant broadband nonlinear optical absorption response in dispersed graphene single sheets. *Nature Photonics* 5: 554–560, 2011.

[150] **Bao Q et al.** Monolayer graphene as a saturable absorber in a mode-locked laser. *Nano Res.* 4(3):297–307, 2011.

[151] **Hendry E, Hale P, Moger J, Savchenko A, Mikhailov S.** Coherent nonlinear optical response of graphene. *Phys. Rev. Lett.* 105: 97401, 2010.

[152] **Wang J, Hernandez Y, Lotya M, Coleman JN, Blau WJ.** Broadband Nonlinear Optical Response of Graphene Dispersions. *Adv. Mater.* 21: 2430–2435, 2009.

[153] **Tutt LW, Kost A.** Optical limiting performance of C60 and C70 solutions. *Nature* 356: 225–226, 1992.

[154] **Park J, Nam S, Lee M, Lieber CM.** Synthesis of monolithic graphene-graphite integrated electronics. *Nature materials* 98: 082117, 2011.

[155] **Li X, Wang X, Zhang L, Lee S, Dai H.** Chemically derived, ultrasmooth graphene nanoribbon semiconductors. *Science* 319: 1229–1232, 2008.

[156] **Tans SJ, Verschueren ARM, Dekker C.** Room-temperature transistor based on a single carbon nanotube. *Nature* 393: 49–52, 1998.

[157] **Martel R, Schmidt T, Shea HR, Hertel T, Avouris P.** Single and multi-wall carbon nanotube field-effect transistors. *Appl. Phys. Lett.* 73: 2447–2449, 1998.

[158] **Zhu HW, Xu CL, Wu DH, Wei BQ, Va jtai R, Ajayan PM.** Direct Synthesis of Long Single-Walled Carbon Nanotube Strands. *Science* 296: 884–886, 2002.

[159] **McCann E, Fal'ko VI.** Symmetry of boundary conditions of the Dirac equation for electrons in carbon nanotubes. *J. of Phys. Cond. Matter* 16: 2371–2379, 2004.

[160] **Kreupl F.** Carbon nanotubes finally deliver. *Nature* 484: 321–322, 2012.

[161] **Franklin AD et al.** Sub-10 nm carbon nanotube transistor. *Nano Lett.* 12:7 58–762, 2012.

[162] **Jang S et al.** Flexible, transparent single-walled carbon nanotube transistors with graphene electrodes. *Nanotech.* 21: 425201, 2010.

[163] **Shulaker MM, Hills G, Patil N, Wei H, Chen HY, Wong HSP, Mitra S.** Carbon nanotube computer. *Nature* 501: 526, 2013.

[164] **Franklin AD.** Electronics: The road to carbon nanotube transistors. *Nature* 498:443, 2013.

[165] **Javey A, Guo J, Wang Q, Lundstorm M, Dai H.** Ballistic Carbon Nanotube Transistors. *Nature* 424: 654, 2003.

[166] **Britnell L et al.** Field-Effect Tunneling Transistor Based on Vertical Graphene Heterostructures. *Science* 335: 947–950, 2012.

[167] **Ponomarenko LA et al.** Tunable metal-insulator transition in double-layer graphene heterostructures. *Nature Phys.* 7: 958–961, 2011.

[168] **Yang X et al.** Graphene tunnelling FET and its applications in low power circuit design. *GLSVLSI10 Proceedings of the 20th symposium on Great lakes symposium on VLSI.* 263–268, 2010.

[169] **Michetti P, Cheli M, Iannaccone G.** Model of tunneling transistors based on graphene on SiC. *Appl. Phys. Lett.* 96: 133508, 2010.

[170] **Zhao P, Chauhan J, Guo J.** Computational study of tunneling transistor based on graphene nanoribbon. *Nano Lett.* 9: 684–688, 2009.

[171] **Zhang Q, Fang T, Xing H, Seabaugh A, Jena D.** Graphene nanoribbon tunnel transistors. *IEEE Electron Dev. Lett.* 29: 1344–1346, 2008.

[172] **Ionescu MA, Reil H.** Tunnel field-effect transistors as energy-efficient electronic switches. *Nature* 479: 329–337, 2011.

[173] **Nandkishore R, Levitov L.** Common-path interference and oscillatory Zener tunneling in bilayer graphene pn junctions. *PNAS* 108: 14021–14025, 2011.

[174] **Georgiou T et al.** Vertical Field Effect Transistor based on Graphene-WS2 Heterostructures for flexible and transparent electronics. *Nature Nanotech.* 8: 100–103, 2013.

[175] **Britnell L et al.** Resonant tunnelling and negative differential conductance in graphene transistors. *Nature Comm.* 4: 1794, 2013.

[176] **Nguyen VH et al.** Bandgap nanoengineering of graphene tunnel diodes and tunnel transistors to control the negative differential resistance. *J. Comput. Electron* 12: 85–93, 2012.

[177] **Malec CM, Davidovic D.** Transport in graphene tunnel junctions. *J. Appl. Phys.* 109: 064507, 2011.

[178] **Cobas E, Friedman AL, Erve OMJ, Robinson JT, Jonker BT.** Graphene As a Tunnel Barrier: Graphene-Based Magnetic Tunnel Junctions. *Nano Lett.* 12: 3000–3004, 2012..

[179] **Wu Y et al.** High-frequency, scaled graphene transistors on diamond-like carbon. *Nature* 472: 74–78, 2011.

[180] **Schall D, Otto M, Neumaier D, Kurz H.** Integrated Ring Oscillators based on high-performance Graphene Inverters. *Scientific Rep.* 3: 2592, 2013.

[181] **Zheng J et al.** Sub-10 nm Gate Length Graphene Transistors: Operating at Terahertz Frequencies with Current Saturation. *Scientific Rep.* 3: 1314, 2013.

[182] **Lin YM et al.** 100-GHz Transistors from Wafer-Scale Epitaxial Graphene. *Science* 327: 662, 2010.

[183] **Cheng R et al.** High frequency self-aligned graphene transistors with transferred gate stack. *PNAS* 109: 11588–11592, 2012.

[184] **Yung KC, Wu WM, Pierpoint MP, Kusmartsev FV.** Introduction to Graphene Electronics - A New Era of Digital Transistors and Devices. *Contemp. Phys.* DOI:10.1080/00107514.2013.833701, 2013.

[185] **Pototsky A, Marchesoni F, Kusmartsev FV, Hanggi P, Savel'ev SE.** Relativistic Brownian motion on a graphene chip. *Europ. J. Phys.* B85: 356, 2012.

[186] **Yang Y et al.** Coherent nonlocal transport in quantum wires with strongly coupled electrodes. *Phys. Rev. B* 87: 045403, 2013.